Physics Reports 999 (2023) 1–60

Contents lists available at ScienceDirect

Physics Reports

journal homepage: www.elsevier.com/locate/physrep

SYNAPSE: An international roadmap to large brain imaging

Anton P.J. Stampfl [1], Zhongdong Liu [2], Jun Hu [3], Kei Sawada [4], H. Takano [4], Yoshiki Kohmura [4], Tetsuya Ishikawa [4], Jae-Hong Lim [5], Jung-Ho Je [6], Chian-Ming Low [7], Alvin Teo [8], Eng Soon Tok [9], Tin Wee Tan [10], Kenneth Ban [10], Camilo Libedinsky [11,12], Francis Chee Kuan Tan [13], Kuan-Peng Chen [14], An-Cheng Yang [14], Chao-Chun Chuang [14], Nan-Yow Chen [14], Chi-Tin Shih [15], Ting-Kuo Lee [16], De-Nian Yang [17], Hsu-Chao Lai [18], Hong-Han Shuai [19], Chang-Chieh Cheng [20], Yu-Tai Ching [21], Chia-Wei Li [22], Ching-Che Charng [23], Chung-Chuan Lo [23], Ann-Shyn Chiang [23], Benoit Recur [24], Cyril Petibois [24], Chia-Liang Cheng [25], Hsiang-Hsin Chen [24,26], Shun-Min Yang [24,26], Yeukuang Hwu [24,26], Catleya Rojviriya [27], Supagorn Rugmai [27], Saroj Rujirawat [27], Giorgio Margaritondo [28,*]

[1] *Australian Nuclear Science and Technology Organization, Lucas Heights, NSW 2234, Australia*
[2] *Henan university of Technology, Zhengzhou, China*
[3] *Shanghai Institute of Applied Physics, Chinese Academy of Science, Shanghai, China*
[4] *RIKEN SPring-8 Center, Hyogo 679-5148, Japan*
[5] *Pohang Accelerator Laboratory, Pohang University of Science and Technology, Pohang, Gyeongbuk 37673, South Korea*
[6] *Department of Materials Science and Engineering, Pohang University of Science and Technology, Pohang, Gyeongbuk 37673, South Korea*
[7] *Department of Pharmacology, Department of Anaesthesia, and Healthy Longevity Research Programme, Yong Loo Lin School of Medicine, National University of Singapore, Singapore*
[8] *School of Chemical and Life Sciences, Nanyang Polytechnic, Singapore*
[9] *eMaGIC-Lab, Department of Physics, National University of Singapore, Singapore*
[10] *National Supercomputing Center, Singapore*
[11] *Department of Psychology, The N1 Institute for Health, National University of Singapore, Singapore*
[12] *Institute of Molecular and Cell Biology, A*STAR, Singapore*
[13] *Department of Anaesthesia, National University Hospital, National University Health System, Singapore*
[14] *National Center for High-Performance Computing, Hsinchu, Taiwan, ROC*
[15] *Department of Physics, Tunghai University, Taichung, Taiwan, ROC*
[16] *Department of Physics, National Tsing Hua University, Hsinchu, Taiwan, ROC*
[17] *Institute of Information Science, Academia Sinica, Taipei, Taiwan, ROC*
[18] *Department of Computer Science, National Yang Ming Chiao Tung University, Hsinchu, Taiwan, ROC*
[19] *Department of Electronics and Electrical Engineering, National Yang Ming Chiao Tung University, Hsinchu, Taiwan, ROC*
[20] *Information Technology Service Center, National Yang Ming Chiao Tung University, Hsinchu, Taiwan, ROC*
[21] *National Yang Ming Chiao Tung University, Hsinchu, Taiwan, ROC*
[22] *Department of Life Science, National Tsing Hua University, Hsinchu, Taiwan, ROC*
[23] *Institute of Systems Neuroscience, and Brain Research Center, National Tsing Hua University, Hsinchu, Taiwan, ROC*
[24] *Institute of Physics, Academia Sinica, Taipei, Taiwan, ROC*
[25] *Department of Physics, National Dong Hwa University, Hualian, Taiwan, ROC*
[26] *Department of Engineering Science, National Cheng Kung University, Taiwan, ROC*
[27] *Synchrotron Light Research Institute, Thailand*
[28] *Faculté des Sciences de Base, Ecole Polytechnique Fédérale de Lausanne, Lausanne 1015, Switzerland*

* Corresponding author.
E-mail address: giorgio.margaritondo@epfl.ch (G. Margaritondo).

https://doi.org/10.1016/j.physrep.2022.11.003
0370-1573/

ARTICLE INFO

Article history:
Received 31 August 2022
Received in revised form 23 November 2022
Accepted 24 November 2022
Available online xxxx
Editor: Fulvio Parmigiani

Keywords:
Brain mapping
Radiology
X-rays
Synchrotron
Phase contrast
Supercomputing

ABSTRACT

Since 2020, synchrotron radiation facilities in several Asia-Pacific countries have been collaborating in a major project called "SYNAPSE" (Synchrotrons for Neuroscience: an Asia-Pacific Scientific Enterprise). They use x-ray imaging to attack in a coordinated fashion one of the major issues in modern science: the structure of animal and human brains, including neurons and connections. The objective is to develop Google-like maps also including detailed structural and functional information for selected regions of interest. The sheer mass of data needed for the objective poses huge problems for the acquisition, processing, storage and use of images. In order to complete the task within a reasonable time, the key element of the SYNAPSE strategy is the parallel and coordinated work of several facilities on the same specimens. This article reviews different aspects of the enterprise, including the foundations of synchrotron radiation, coherence and of its role in advanced imaging, electron accelerators, x-ray optics and detectors. This will provide the foundation for an extensive presentation of the different components of SYNAPSE, with an overview of results already obtained within the consortium.

Contents

1. Foreword: SYNAPSE and its philosophy

Brain research is one of the many fields of science and technology that exploit the three-dimensional (3D) observation of objects with high spatial resolution. X-ray computed tomography (CT) is one of the few suitable ways to meet this challenge. Today, we can achieve sub-micrometer resolution in this technique by using state-of-the-art synchrotron X-ray sources and detection systems. This opens the way, in particular, to a novel approach for mapping the brains of large animals or humans.

X-ray tomography follows a scaling law between the sample size and the highest resolution. It is difficult to attain micrometer resolution for meter size samples. Therefore, 3D mapping of a large sample such as the human brain with sub-micrometer resolution requires stitching together a vast amount of structural data. The data acquisition and processing speeds must be incredibly high to achieve full reconstruction in a reasonable time scale.

A direct way to increase the data acquisition speed is to enhance the X-ray flux (within the radiation damage limit) with an advanced X-ray source and high-performance optics. Other critical factors are the dynamic range and the dead time of the detectors. Therefore, one must also consider robots that automatically exchange samples to speed up the process.

High X-ray flux and robotization facilitate the task of large-brain mapping. The SYNAPSE enterprise adds to these factors a fundamental strategic element: it uses synchrotron radiation techniques simultaneously at several facilities. This makes it possible to acquire the huge amount of data needed for large-brain mapping in a reasonable time. And it constitutes a radically different way to use synchrotron radiation with respect to the current practices.

After preliminary negotiations and planning, the idea of SYNAPSE became concrete with an inauguration ceremony in Singapore early in 2020. The event included the formal signature of documents manifesting the partners' intent to implement a common strategic plan.

As mentioned, SYNAPSE is not only a major enterprise, but also a very important change in strategy in synchrotron radiation research — half a century after its birth. For many decades, the use of synchrotron sources was influenced by the ongoing use of the accelerators for elementary particle research: a parasitic philosophy transferred to synchrotron radiation activities themselves [1].

Consequently, synchrotron radiation experiments have been typically performed by medium-size teams at specific facilities, and in competition between them. This strategy was reasonable for the experiments in materials science that initially dominated synchrotron radiation research.

But it is no longer effective now for fundamental scientific objectives that require a massive volume of experimental data. Large-brain research on a microscopic scale is a very significant case: we shall indeed see that the data size defies imagination.

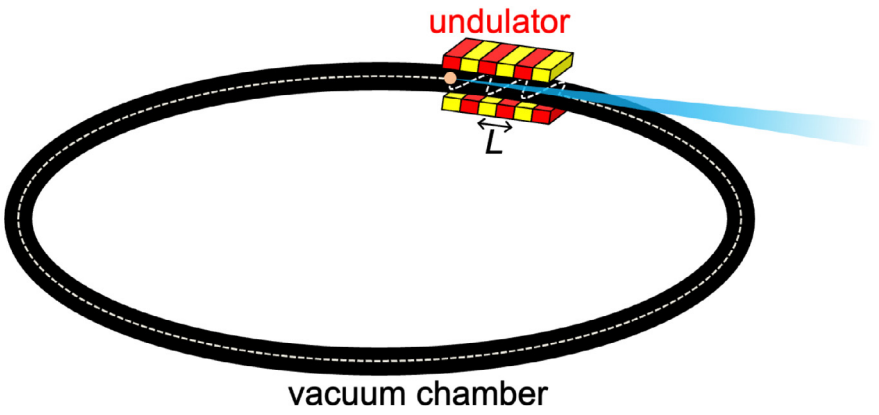

Fig. 1. Emission of synchrotron radiation by an electron in a closed-loop accelerator, subject to the action of an undulator [1].

Such a mass of information cannot be obtained at present without a coordinated use of several different facilities. The standard way to manage synchrotron radiation research does not deal with this need. SYNAPSE is a new approach tackling the problem with an innovative strategy.

This enterprise can thus impact synchrotron radiation research beyond its specific scientific objectives. It brings indeed a novel solution of scientific problems that cannot be managed with the present synchrotron radiation practices. This opens up new research horizons beyond the present spectrum of X-ray science and technology.

1.1. Synchrotron radiation basics

The basic ingredient of SYNAPSE is synchrotron radiation. Therefore, we will begin our presentation with an overview of its foundations.

For seven decades after Roentgen's discovery [2], the X-rays sources did not progress much and remained largely unsatisfactory [1,3]. The cause of this slow evolution was rather fundamental. Sources of electromagnetic radiation typically have a size comparable to the emitted wavelengths. For X-rays, the size is similar to that of atoms. In fact, the emitters in a conventional (anode) X-ray source are its individual atoms.

However, such sources have limited performance since the atoms are bound to a solid that when exposed to a high emitted power can be damaged. Furthermore, the emission is not concentrated in a narrow angular range as in a laser, so in practical applications much of it is wasted.

Alternate X-ray-emitting devices are very desirable. But their size should be again comparable to individual atoms, making their fabrication an impossible technological task.

Starting in the 1960s, a solution to this problem emerged [1,3] as a byproduct of the technology of electron accelerators. The electrons in such machines travel at a speed close to that of light, c. Therefore, their properties, including the emission of electromagnetic radiation, are subject to the rules of Einstein's relativity [4,5].

Consider for example (Fig. 1) an electron in an accelerator (e.g., a synchrotron) that oscillates in the transverse direction because of the action of a periodic series of magnets (an "undulator") [1]. The transverse acceleration of an electric charge causes the emission of electromagnetic radiation. For a non-relativistic electron, the emitted wavelength approximately equals the period L of the undulator,

Relativity, however, affects in two ways the wavelength detected in the laboratory frame [1,6]. First, the undulator period "seen" by the electron is decreased to L/γ by the "Lorentz contraction" — where $\gamma = (1 - v^2/c^2)^{-1/2}$ is the relativistic factor that measures the electron energy. Second, the wavelength is affected by the Doppler shift, which for electromagnetic waves is a relativistic effect. This phenomenon approximately divides the detected wavelength by a factor $2\ \gamma$.

Overall, the wavelength is divided by a factor $\approx \gamma\ (2\ \gamma) = 2\ \gamma^2$, shifting to the short values typical of X-rays. In fact, for modern accelerators γ is typically several thousand.

The emission of X-rays by electron accelerators was first detected [7,8] for machines called "synchrotrons". It was thus baptized "synchrotron radiation", even though the present sources are no longer synchrotrons but "storage rings".

Simple relativistic arguments also explain [1,6] other characteristics of synchrotron radiation sources that make them very superior to conventional X-ray emitters. In particular, the fast forward motion of the electrons "projects" their emission ahead in the longitudinal direction. Relativity boosts this effect, producing strong angular collimation: the radiation is confined to a cone of width $\approx 1/\ \gamma$ and its geometry is laser-like.

The angular collimation means that each electron acts as an extreme flashlight, producing for example a fast emission pulse each time it passes through an undulator. According to the Fourier theorem, a fast pulse corresponds to a

band of frequencies or wavelengths, $\Delta\lambda$. From this band, specific values can be selected using filtering devices called "monochromators".

The emitted power is proportional to the square of the acceleration. The relativistic transformation of coordinates multiplies the acceleration by γ^2 and the emission by γ^4, producing a very high flux. The flux is not limited by the possible damage to the host material as in conventional X-ray sources, since the emitting electrons are not bound to a solid but circulate instead in the vacuum chamber of the accelerator.

The emission is linearly polarized in the plane of the transverse electron acceleration. Special periodic magnetic devices can also produce elliptical polarization.

The synchrotron source size is determined by the transverse cross section Σ of the electron bunches circulating in the accelerator. Modern accelerator technology produces small Σ, making synchrotron radiation sources point-like and even more laser-like.

The combination of high flux, small source size and strong angular combination produces a high "brightness" or "brilliance" B [1,3,6]. This is a quality parameter proportional to the flux F and inversely proportional to Σ and to the solid angular spread Ω of the emission: $B = \text{constant } x\ F/(\Sigma\ \Omega)$.

Later, we shall discover that a high B also implies a large degree of "lateral coherence" [9]. This has a strong impact on X-ray imaging.

An electron accelerator, like a storage ring, hosts several synchrotron radiation sources — whose emissions can be processed by monochromators and other optical components along beamlines to experimental chambers where they are utilized for a variety of applications. Each source is a magnetic device that produces transverse acceleration.

There exist two kinds of such devices besides undulators. First, "wigglers", which are periodic magnet arrays like the undulators but with stronger magnetic fields. The wavelength band emitted by a wiggler is broader than that of an undulator, where some spectral filtering occurs producing a narrower band.

The third class of synchrotron radiation sources is that of the "bending magnets", whose primary role is to keep the electrons in the accelerator within a closed orbit. The emission of synchrotron radiation is an important secondary role: sources of this kind typically supply X-rays to the majority of the beamlines around an accelerator.

The properties of synchrotron radiation sources — high brightness, high flux, collimation, polarization and coherence are reminiscent of those of lasers. Are such sources, indeed, lasers? Not really, since the emission mechanism is not stimulated emission but random spontaneous emission, and there is no optical amplification as in a laser.

There exist, however, another class of X-ray sources, the "free electron lasers" (FELs), whose operating mechanism – although not equivalent to that of lasers – does involve optical amplification [6]. This mechanism was originally proposed and implemented for infrared emission [10], but in recent years became a reality also for X-rays [6,11,12]. And opened up exciting new research opportunities — in particular for imaging.

As schematically illustrated in Fig. 2, the optical amplification occurs when the electrons in a bunch traveling along an undulator become arranged in periodic "slices" with period equal to the wavelength — so that their emissions are correlated [6]. This rearrangement is produced by the interaction of the electrons with the radiation stochastically emitted after the bunch enters the undulator.

Indeed, one can demonstrate that the wave fields indirectly "push" the electrons within a bunch along the undulator axis. The wave is zero at its nodes and so is its interaction with the electrons. Therefore, we could expect the electrons to accumulate at the nodes. However, within one wavelength the wave fields have two opposite directions (see the bottom part of Fig. 2). As a consequence, if the electrons are pushed towards a given node, they are pushed away from the two adjacent nodes. Thus, the accumulation occurs at every other node and the microbunching period is one wavelength.

The very short wavelengths of X-rays make this mechanism vulnerable to perturbations. This delayed the practical implementation of X-ray FELs for several decades. Furthermore, the effects of optical amplification for X-rays cannot be boosted by an optical cavity as for visible and infrared lasers. Indeed, reflection is very weak at short wavelengths except at glancing incidence. Therefore, optical amplification in an FEL for X-rays must be strong enough to produce one-pass lasing. This requires a very long undulator and very concentrated, high-density electron beams that are technically difficult to realize and contributed to the aforementioned delay. Such beams can be obtained with linear accelerators.

As these difficulties have been surmounted, X-ray FELs are now a reality [6]. They are based on linear accelerators (LINACs) and produce very short pulses with extreme peak brightness and excellent lateral coherence, as we shall discuss later.

1.1.1. Coherence

The interactions of X-rays with matter that are exploited for imaging are of different kinds. Most important is absorption, which is not directly linked to the wave nature of the radiation. However, in several imaging techniques the wave aspects are relevant, requiring X-rays with a sufficient level of "coherence" [9].

Roughly speaking, coherence is "the property that allows radiation to produce observable wave phenomena" [9]. To discover its key aspects, one can consider anyone of such phenomena. Here, we shall use diffraction by two very narrow slits at a distance Δ from each other (Fig. 3).

Suppose that the slits are illuminated by a plane-wave X-ray beam: will it produce a visible diffraction pattern in the fluorescent panel? The answer is positive if the X-ray source is very small (point-like) and emits only one wavelength, λ. The angular distance between the central fringe in the pattern and the two adjacent ones is $\approx \lambda/\Delta$.

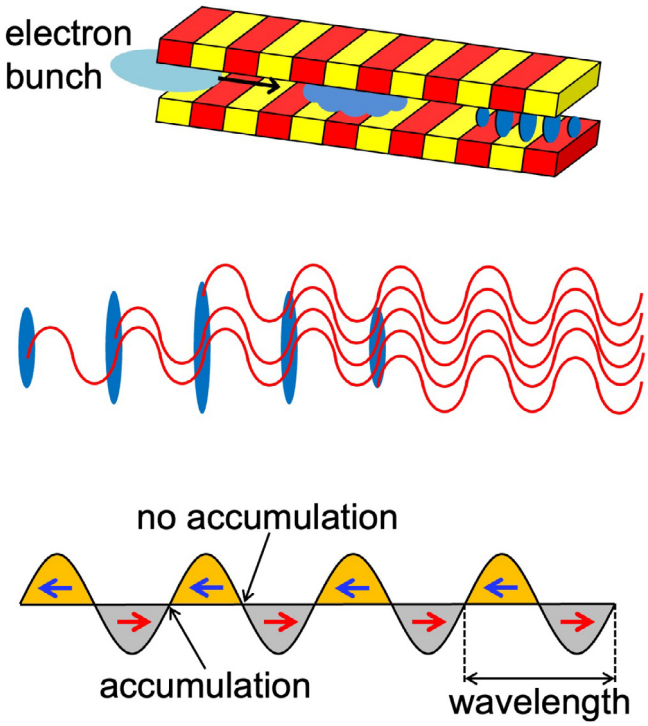

Fig. 2. Schematic illustration of the optical amplification mechanism of a free electron laser [6]. Top: traveling along an undulator, an electron bunch interacts with its emitted waves and is re-shaped in periodic "slices". Middle: the subsequent emission from the electrons in the "slices" is correlated and amplifies the initial wave. Bottom: the wave changes sign within a wavelength, and the corresponding interactions with the electrons lead to accumulation at every other node, so the microbunching period equals the wavelength.

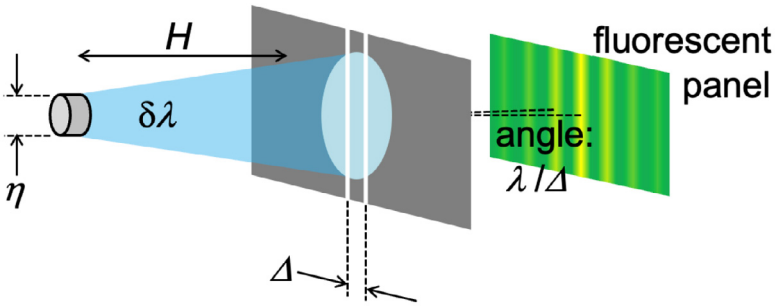

Fig. 3. The diffraction by two very narrow slits can be used to analyze the notion of coherence.

But the situation is more complex for a realistic source, for example a circular one with diameter η that emits a band of wavelengths centered at λ, of finite width $\delta\lambda$. The collective effect of all wavelengths in this band "blurs" the fringe distance from λ/Δ to $\delta\lambda/\Delta$. When this blurring exceeds the distance itself, the pattern is no longer visible.

Therefore, the condition for observing a diffraction pattern is $\delta\lambda/\Delta < \lambda/\Delta$, or

$$\delta\lambda/\lambda < 1.$$

This is one of the requirements for coherence, specifically the condition for "time coherence" or "longitudinal coherence". Another way to express it is by using the "coherence length", defined as

$$L_c = \lambda^2/\delta\lambda;$$

longitudinal coherence is present if $L_c > \lambda$.

To better understand the coherence length, we must consider that the wave effects are caused by the "phase", which in a wave function propagating along the z-direction, e.g.,

$$E = E_o exp\{i[(z - ut)/\lambda + \phi]\},$$

corresponds to the angular argument $(z-ut)\lambda+\phi$ of the (oscillating) imaginary exponential function. Here, u is the phase velocity.

Consider the two extreme wavelengths in the emitted band, $\lambda + \delta\lambda/2$ and $\lambda - \delta\lambda/2$. Assume that at a certain distance from the source the phases of the corresponding waves coincide. But, as the waves propagate, their phases will subsequently become different. After a distance L, the phase difference between them is $2\pi[L/(\lambda-\delta\lambda/2)-L/(\lambda+\delta\lambda/2)]$, which for $\delta\lambda/2<<\lambda$ becomes:

$$\approx(2\pi L/\lambda)[1+\delta\lambda/(2\lambda)-1+\delta\lambda/(2\lambda)] = 2\pi L\delta\lambda/\lambda^2.$$

The two waves are still reasonably "in phase" with each other if their phase difference is $<< 2\pi$, and this is true if $L<<\lambda^2/\delta\lambda = L_c$. Therefore, L_c is the maximum distance over which the radiation in the bandwidth $\delta\lambda$ keeps a reasonably homogeneous phase.

We shall now consider another kind of coherence: the "lateral" or "spatial" one. Referring to Fig. 3, each point in an extended source produces a diffraction pattern. The superposition of patterns, however, may blur the fringes making them impossible to observe.

The maximum distance between two source points is η. The corresponding maximum angular distance between the corresponding patterns is $\approx\eta/H$, where H is the source-slit separation. A pattern is still visible if this distance is smaller than the already mentioned angular distance between fringes: $\eta/H < \lambda/\Delta$, or

$$\Delta < \lambda H/\eta.$$

This is the condition for lateral (spatial) coherence.

There is another, interesting way to express this notion. Basically, only the portion of the radiation that illuminates the slit system contributes to diffraction, i.e., reveals lateral coherence. This corresponds to an angular range $\approx\Delta/H$ in the direction perpendicular to the slits.

Extending the same analysis to both transverse directions, we can conclude that only the emission within a solid angle $\approx(\Delta/H)^2$ can contribute to wave effects requiring lateral coherence. If the source emits over a total solid angle Ω, the corresponding portion of the total emitted power is given by the ratio of the solid angles, $\approx(\Delta/H)^2/\Omega$. Using the above-derived condition for lateral coherence, $\Delta < \lambda H/\eta$, this ratio is

$$< [(\lambda H/\eta)/H]^2/\Omega = \lambda^2/(\eta^2\Omega).$$

The factor $\lambda^2/(\eta^2\Omega)$ defines the "coherent power" and is a measure of the lateral coherence of the radiation. A source is laterally coherent if its coherent power is large. Note that the geometric parameters η^2 and Ω are related to those that define the brightness (since η^2 is proportional to the source size Σ). Historically, the efforts to enhance the brightness by improving the synchrotron source geometry produced lateral coherence as an important byproduct [1].

These efforts, however, are now coming to an end. There exists indeed [9] a fundamental "diffraction limit" that prevents the coherent power factor $\lambda^2/(\eta^2\Omega)$ to become larger than unity. This limit is now reached by many synchrotron sources and by all the X-ray FELs.

The conditions for lateral coherence lead to a notion complementary to the coherence length, the "coherent area". We have seen that the effects related to lateral coherence are present over a distance $\Delta < \lambda H/\eta$ in the transverse direction perpendicular to the slits. Considering both transverse directions, one realizes that such effects are present over a transverse "coherent area" $(\lambda H/\eta)^2$.

Together, the coherence length and the coherent area define the "coherence volume":

$$V_c = (\lambda^2/\delta\lambda)(\lambda H/\eta)^2 = \lambda^4 H^2/(\delta\lambda\eta^2).$$

Basically, high overall coherence requires the source to pack a lot of emitted energy (or, equivalently, a lot of photons) within this volume.

Note the implication of the λ^2 term in the coherent power factor $\lambda^2/(\eta^2\Omega)$. Reaching high lateral coherence is much more difficult for short-wavelength X-rays than for visible or infrared radiation. The same conclusion applies to longitudinal coherence, since the coherence length too is proportional to λ^2. And the coherent volume is proportional to λ^4. This is why coherence-related effects, which have been exploited for centuries in visible and infrared optics, emerged only in recent years for short-wavelength X-rays.

The situation changed when, as we have seen, the improvements targeting high brightness also produced high lateral coherence. Concerning longitudinal coherence, the required narrow wavelength bandwidth can be achieved with monochromators. A monochromator sharply decreases the X-ray flux available for experiments. However, this loss is manageable thanks to the high initial brightness of synchrotron sources.

Coherence has thus become an essential ingredient of advanced X-ray imaging. The results are rather spectacular, as we shall see, and impact many different domains including brain research.

As to X-ray FELs, their small source size (corresponding to the highly concentrated electron bunch required for one-pass lasing) and strong angular collimation produce a high level of lateral coherence, reaching the diffraction limit. The situation for longitudinal coherence, however, is more complicated.

In the FEL mechanism the optical amplification applies to waves that are randomly emitted when the electron bunch enters the undulator. Due to this random character, each X-ray pulse has a different time shape. This, according to the Fourier theorem, produces a broad bandwidth of frequencies (and wavelengths), limiting the longitudinal coherence.

Fig. 4. X-ray image obtained with phase contrast (left) compared (right) to the corresponding (simulated) absorption radiograph.

However, many applications require high longitudinal coherence and a non-changing pulse shape. The solution to this problem was implemented in recent years [9,12] and is called "seeding". In it, the FEL is not used to optically amplify randomly emitted waves but externally generated pulses of well-defined and unchanging shape. This technique produces FEL sources with high coherence both laterally and longitudinally [12].

1.1.2. Coherent imaging

SYNAPSE is based on X-ray imaging techniques, which in turn are based on interactions between the radiation and the object. As mentioned, the most widely used interaction is absorption, which decreases the intensity of X-ray waves traveling through materials. There, exist, however, other kinds of interactions that can contribute to the formation of images, often yielding better results than those of mere absorption [13].

One example is provided by Fig. 4, which compares an image of bubbles obtained with wave-like effects to a standard (adsorption) radiograph. The absorption only modifies the intensity of the X-ray wave, i.e., the amplitude of its electric and magnetic fields. But it does not touch the phase, i.e., the angular argument $(z - ut)/\lambda + \phi$.

This means that absorption radiology only exploits part of the information produced by wave–matter interactions. Such interactions include wave-like phenomena such as diffraction, refraction or interference. They are used in alternate techniques collectively called "phase contrast" imaging [13]. As exemplified by Fig. 4, such techniques enhance the information content of the images.

Being based on wave-like phenomena, phase contrast imaging requires a high level of coherence. But we have seen that coherence is difficult to achieve for X-rays. Indeed, phase-contrast X-ray imaging became a reality only after the advent of high-brightness synchrotron sources.

Phase contrast X-ray imaging is, in reality, a collection of different approaches delivering different kinds of information. In principle, a description of the underlying mechanisms would require a complete theory of X-ray scattering by electrons in the imaged objects. This includes energy-conserving phenomena like interference, diffraction and refraction as well as inelastic phenomena like absorption.

Some basic features, however, can be understood without sophisticated theories [13]. One can see in Figs. 4 and 5 that coherent X-rays enhance the visibility of edges between different parts of the object. What produces this edge enhancement?

Actually, as shown by Fig. 5, two phenomena contribute to it: edge refraction and edge diffraction. Such phenomena are schematically illustrated in Fig. 6. In the top part of the figure, we see a beam of X-rays passing through a slanted edge between two parts of the specimen. The beam deviation produces a pair of bright–dark fringes as in the top portion of Fig. 5. This phenomenon is observed in the majority of the phase-contrast X-ray images.

The visibility of the fringe pairs changes with the specimen-detector distance, which for a fixed deviation changes their geometry at the detector. For small distances, the fringes may be too narrow with respect to the detector resolution, and therefore not visible. As the distance increases, they become visible. But their widths eventually become too broad, and they disappear.

The specific distances for which each aspect of the above behavior occurs depend on the edge geometry — which changes from edge to edge and is in general more complex than the simple case of the top part of Fig. 6. So, the above conclusions do not lead to general rules for all specimens and all edges and must be used empirically.

The second edge-enhancement mechanism is illustrated in the bottom part of Fig. 6. Basically, it is a case of the classic phenomenon of "Fresnel edge diffraction", which for visible light produces diffraction fringes at the edges of opaque objects. This mechanism yields not just a pair but a series of fringes, as seen in the bottom part of Fig. 5.

Contrary to edge enhancement by refraction, the visibility of the Fresnel-diffraction fringes monotonically increases with the specimen-detector distance. Such distance can thus be adjusted to enhance one of the two mechanisms of Fig. 6 with respect to the other, and in general to optimize the edge visibility. In most cases, refraction fringe pairs are the most effective in creating good phase-contrast radiographs.

Fig. 5. Two X-ray images of the edge of an optic fiber, obtained with different geometries and emphasizing the two different phase-contrast mechanisms producing edge enhancement.

Both mechanisms can produce visible fringes only if the initial X-ray beam has a well-defined geometry. This requires a high level of spatial coherence.

Interestingly, simple models demonstrated that only a limited level of longitudinal coherence is required [14,15]. Thus, it is not necessary to decrease the wavelength bandwidth with a monochromator. Without a monochromator, one avoids the corresponding loss of flux and increases the signal level. This approach has boosted the possible application of phase contrast radiology and its impact in different disciplines.

1.2. Technical breakthroughs along the path to SYNAPSE: accelerators

Electron accelerators used as synchrotron sources are of course a key factor in advanced X-ray imaging, which in turn is the backbone of SYNAPSE. We briefly review here the corresponding developments.

The early use of synchrotron radiation was parasitic to high-energy physics experiments. However, researchers gradually felt the need for dedicated light sources. The full-time use of an accelerator as a synchrotron source was successfully tested with Tantalus at the Wisconsin Synchrotron Radiation Center in the late 1960's. Projects for the construction of storage ring accelerators dedicated to synchrotron radiation began in the mid-1970s. These dedicated facilities are known as "second-generation sources".

Being free from the restriction of high-energy experiments, researchers were seeking novel ways to generate brighter radiation. A preferred solution was provided by wigglers or undulators installed on the straight sections of the accelerator. We have seen how undulators generate high-brightness radiation. In addition, their emission is quasi-monochromatic owing to the already mentioned interference effect.

Optimization of the accelerators for the use of undulators promoted the concept of third-generation synchrotron radiation sources. The performance of undulators strongly depends on the "emittance" of the electron beam, which is the combination of the transverse cross section and the angular spread from the reference trajectory. Lower horizontal emittance is preferable for better performing undulators, and became a target for third-generation facilities.

Early planning for third-generation facilities began in the 1980s for soft-X-rays and the vacuum UV spectral region in Trieste (ELETTRA), Berkeley (ALS — Advanced Light Source), and elsewhere. The first hard-X-ray third-generation source was the European Synchrotron Radiation Facility (ESRF) in Grenoble. At that time, the undulator technology was still evolving, so a high-energy electron beam (several GeV) was considered necessary to generate hard X-rays with undulators.

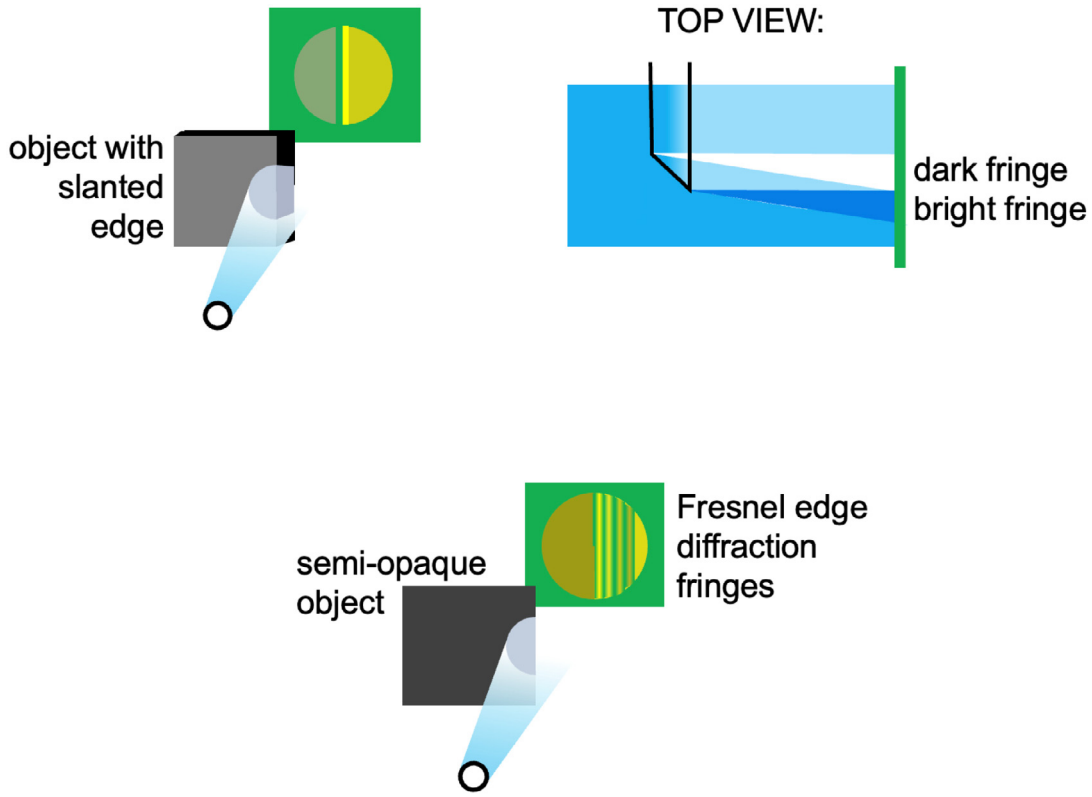

Fig. 6. Schematic illustration of the two edge-enhancement mechanisms active in Fig. 5. Top: production of a bright–dark fringe pair by refraction at a slanted edge. Bottom: Fresnel edge diffraction causes a series of fringes.

The electron energy stepped up from 6 GeV to 7 GeV (Advanced Photon Source-APS, Argonne, USA), and to 8 GeV (SPring-8, Japan). These facilities started user operations in the 1990s.

The operation of third-generation sources led to substantial progress in undulator technology. A remarkable development was the in-vacuum undulators, designed by the SPring-8 team, which had a key role in the subsequent advances in synchrotron and x-FEL sources. The arrays of permanent magnets were placed in a vacuum chamber [16] strongly reducing their gap with respect to conventional out-of-vacuum undulators.

A narrow gap enhances the magnetic field and the emission of X-rays. Indeed, the 27 m long undulator at SPring-8 delivers 10^{14} photons s^{-1} at a photon energy of 15 keV, even after spectral filtering by a Si double-crystal monochromator.

The impact of these achievements was widespread, and SPring-8 has become a worldwide standard [17,18]. The improved uniformity of an undulator magnetic field also enhanced the brightness of the higher harmonics emitted at submultiples of the fundamental wavelength. This made it possible to produce hard-X-rays with medium energy electron accelerators.

As new third-generation sources continued to be built and improved, many users recognized their usefulness for science and technology, including industrial applications. Many countries constructed third-generation SR facilities based on medium-energy (a few 3 GeV) storage rings. In the Asia-Oceania region, there are four such facilities: the Australian Synchrotron (AS) in Melbourne, the Pohang Light Source-II (PLS-II) in Korea, the Shanghai Synchrotron Radiation Facility (SSRF) in China, and the Taiwan Photon Source (TPS) in Hsinchu.

Undulators reach their ultimate performance when the electron beam emittance becomes smaller than the photon beam emittance. This situation corresponds to the already mentioned "diffraction-limit" in coherence. Various efforts have been made towards diffraction-limited light sources. The most effective is the adoption of a multi-bend-achromat (MBA) magnet lattice [19], replacing the typical double-bend-achromat (DBA) [20] lattice of third-generation rings. The MBA strongly decreases the electron beam emittance by increasing the number of bending magnets within a unit cell of the storage ring lattice. Synchrotron radiation facilities based on MBA storage rings are often called "fourth-generation" sources.

MAX-IV in Lund, Sweden, was the first fourth-generation facility [21]. Many synchrotron facilities around the world are now being upgraded using the MBA strategy. Notably, ESRF was recently reshaped obtaining a machine called "Extremely Brilliant Source" (EBS) [22]. And there are several more plans, for example SIRIUS in Brazil [23], for constructing fourth-generation facilities and/or upgrading existing sources.

In the Asia-Pacific region, Japan is constructing a new ultrabright 3 GeV facility in Sendai [24], China, a 6 GeV ring near Beijing [25], Korea a 4 GeV machine in Cheongju [26] and Thailand a 3 GeV source [27]. Japan is also preparing the upgrade of SPring-8 to a 6 GeV fourth-generation facility [28].

Although MBA sources achieve ultrahigh brightness, various issues remain to be addressed from the user perspective. For example, maintaining the stability of the source and that of the beamline optics. Indeed, even tiny vibrations at either the source or the optics degrade the effective geometry and the brightness. Even with these difficulties, MBA machines are excellent continuous sources. In parallel, the advent of X-ray FELs provide outstanding pulsed sources with extreme peak brightness.

1.2.1. X-ray FELs today

We have seen that, due to the previously mentioned technical difficulties, the FEL strategy was limited for decades to long (infrared) wavelengths. But it now extends to X-rays.

The first operating x-FEL was the Linac Coherent Light Source [29] at Stanford, proposed in 1992 by Pellegrini and collaborators and realized in 2009. The Advanced Photon Source at Argonne developed its Low Energy Undulator Test Line (LEUTL) and constructed an FEL for the visible-to-ultraviolet photons [30]. In the same period, DESY at Hamburg was developing the TESLA project [31] for soft-X-rays, which eventually led to the hard-X-ray European X-FEL [32].

When the LCLS and TESLA x-FELs were designed, the in-vacuum undulator technology was not yet mature, so they used out-of-vacuum undulators. Adopting instead in-vacuum undulators with short periods, SPring-8 realized a revolutionary design for FELs, the "SPring-8 Compact SASE Source (SCSS)".

The implementation of new x-FELs is now spreading worldwide, notably with SACLA at SPring-8, the PAL X-FEL [33] in Korea, the Swiss x-FEL at the Paul-Scherrer Institute [34]. The Shanghai Institute of Applied Physics (SINAP) built a soft-X-ray FEL and is planning a high-repetition rate superconducting x-FEL [35]. Another notable development was the realization of the aforementioned "seeding" technique by the FERMI source in Trieste.

These exciting developments justify a question: what role, if any, will x-FEL play in the SYNAPSE strategy? The question is largely open.

For example, the peak brightness of present x-FELs is still insufficient [36] for high-resolution image reconstruction [37] of biomolecules <10 nm. Alternate strategies were proposed exploiting coherence [38–43]. However, their feasibility has not yet been fully demonstrated.

The possible contributions of x-FELs to brain imaging are still not clear. Note that the "detect-and-destroy" strategy, [44], extracting information in a time short enough to avoid significant damage, is also not yet demonstrated for biology tissues. It is, however, possible to use X-ray imaging techniques based on x-FELs, specifically coherent diffraction imaging (CDI), to obtain detailed information on the structures of proteins and the microscopic organelles of neurons.

All in all, the use of x-FELs for SYNAPSE is something to watch but not guaranteed. The possible access to three FELs within the consortium is, however, an advantage.

1.2.2. Developments in X-ray optics

Optics devices for processing X-rays play of course a critical role in imaging. However, they face significant difficulties because of the fundamental physical properties of short-wavelength radiation. Specifically, the real part of the refractive index is close to unity, therefore standard refractive lenses cannot be developed. Furthermore, reflection is very limited except at very small incidence angles. These characteristics sharply limit the applicability of optical solutions developed for the visible light.

Without optical devices, the resolution level achievable by X-ray microimaging is limited. It is specifically difficult to reach spatial resolution better than 1 μm due to penumbral blurring and the diffraction spread. However, with state-of-the-art microfabrication technology, it has become possible to manufacture high-precision X-ray optical devices and widely exceed this limit.

X-ray optical devices are developed for scanning microscopy or for full-field imaging microscopy. Both types of techniques now reach a spatial resolution at the 10 nm level for X-ray photon energies below 20 keV [45,46].

For X-ray optical devices, total reflection, diffraction, and refraction phenomena are utilized. A reference reflection X-ray focusing device is the Kirkpatrick–Baez mirror conceived in 1947 [47], in which two aspherical mirrors that focus in orthogonal directions are arranged in tandem to achieve a point focus. This solution can be used for scanning microscopy.

Reflective optics can also be used in imaging microscopy. One example is the "Wolter mirror", the combination of two aspherical reflection planes with ellipsoidal (or paraboloidal) and hyperbolic surfaces [48–51]. The advantage of this solution is primarily the absence of aberrations [52].

Another widely used X-ray focusing device is the Fresnel zone plate (FZP) [53–55]. This is a concentric circular diffraction grating with alternating absorbing and transmitting zones. The zone thickness and diameter follow a specific mathematical constraint that produces a sharp focal point.

The FZPs are widely used both for scanning and as thin lenses for imaging microscopy with limited aberrations. They work quite well for relatively low photon energies, but their efficiency is lower at high photon energies, for which reflection devices work better. The fabrication of X-ray FZPs is a difficult task since it requires realizing very thin outermost zones with a high aspect ratio to obtain sufficient absorption [56–59]. To solve the corresponding mechanical stability problems requires innovative technical designs [60].

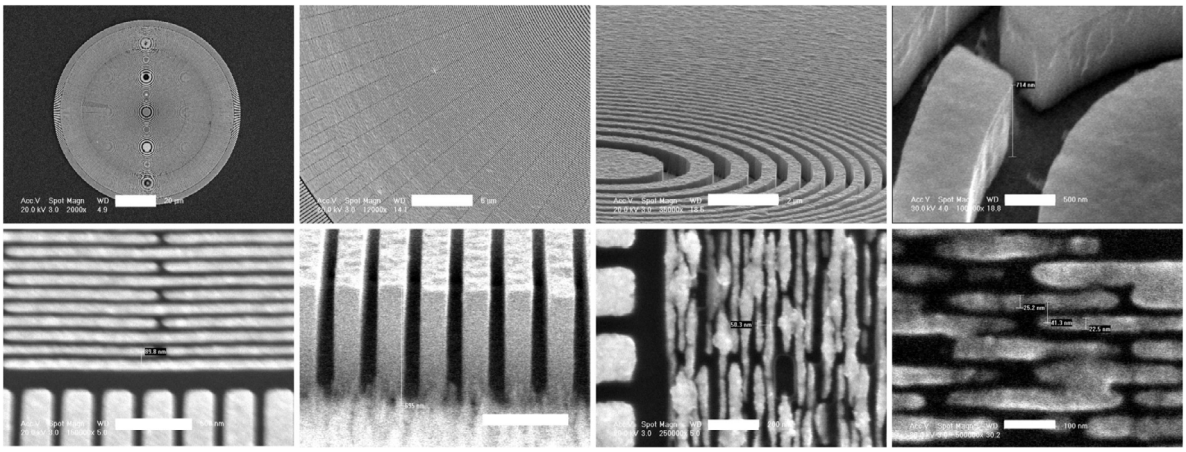

Fig. 7. A series of SEM images with increasing magnification of a Au zone plate with outermost zone width ∼20 nm. Scale bars (top row, left to right): 20 μm, 5 μm, 2 μm, 0.5 μm; (bottom row): 500 nm, 500 nm, 200 nm, 100 nm.

Fig. 7 shows an example of FZP manufactured by SYNAPSE members [61]. The device was fabricated by high-voltage (100 keV) electron beam writing, capable of producing structures of a few nm over a large area (diameter ∼500 μm). The high-resolution FZP pattern developed on a thick photoresist layer is then filled with Au by electrodeposition. The scanning electron microscopy (SEM) images of Fig. 7 show a 500 nm thick Au FZP with 20 nm outermost zone width, reaching an aspect ratio (thickness or height divided by the width) of 25 with a single layer process. This class of zone plates already produced X-ray images with <20 nm resolution [62].

There exist also X-ray refractive-optics devices somewhat reminiscent of visible light lenses. However, as mentioned the (real part of the) refractive index of X-rays in materials is only slightly less than unity. Therefore, compound refractive lenses (CRLs) are used [63], in which many concave lenses are realized in series in a solid material along the optical axis. The CRLs can be used for imaging microscopy [64], especially in the high photon energy range where the absorption by the solid material is limited.

Some of the devices mentioned above can now reach resolutions at the 10 nm level. And this is not the ultimate performance. For example, laterally-graded multilayer focusing mirror with wavefront corrected adaptive X-ray systems [65] and multilayer Laue lenses (MLLs) [66–68] can reach higher resolution, and nanometer-level focusing has been reported [69].

X-ray optics devices play, of course, a fundamental role in brain imaging. Their recent technical progress are essential ingredients for SYNAPSE. Devices with different performance levels will be utilized in the program for different tasks within the overall strategy.

For example, tomography at micron-level resolution can be used for the general brain mapping tasks. And regions of special interest can be analyzed with nanometer-level resolution. The strategy must harmonize the need to obtain the important information and the overall duration of the experiments, as nanometer resolution is of course more time consuming.

The practical implementation of the SYNAPSE strategy relies on forthcoming improvements in resolution and image-taking time. Rather important improvements are underway for both aspects.

1.2.3. Detectors for X-ray imaging

X-ray detectors are another key technical issue for the SYNAPSE project. But they face a fundamental problem. Weak interaction with matter allows high penetration, which is a key reason for the widespread use of X-rays. However, it complicates their detection. As a consequence, radiology largely used for a long time "lens-less" solutions — and still does. This enhances the importance of the spatial resolution and sensitivity of advanced X-ray sensors [70].

X-ray-to-Visible Conversion

This conversion is exploited by many detector systems and is notably implemented with scintillating materials — e.g., CsI or phosphorus particles. The visible images can be magnified with standard optics and detected with a camera, producing radiographs with high spatial resolution. Fig. 8 shows the schematic diagram of a standard imaging system using this conversion to perform submicron-resolution tomography.

This experimental system is, in essence, a visible-light microscope. Thus, innovative approaches originally implemented for visible microscopy can be transferred to radiology using commercial low-cost components.

The spatial resolution allowed by X-ray-to-visible conversion is excellent, reaching the diffraction limit set by the visible light [71,72]. Not surprisingly, this approach dominates full-field radiology with micron and submicron resolution, reaching the nanometer level with matching X-ray magnification optics [73].

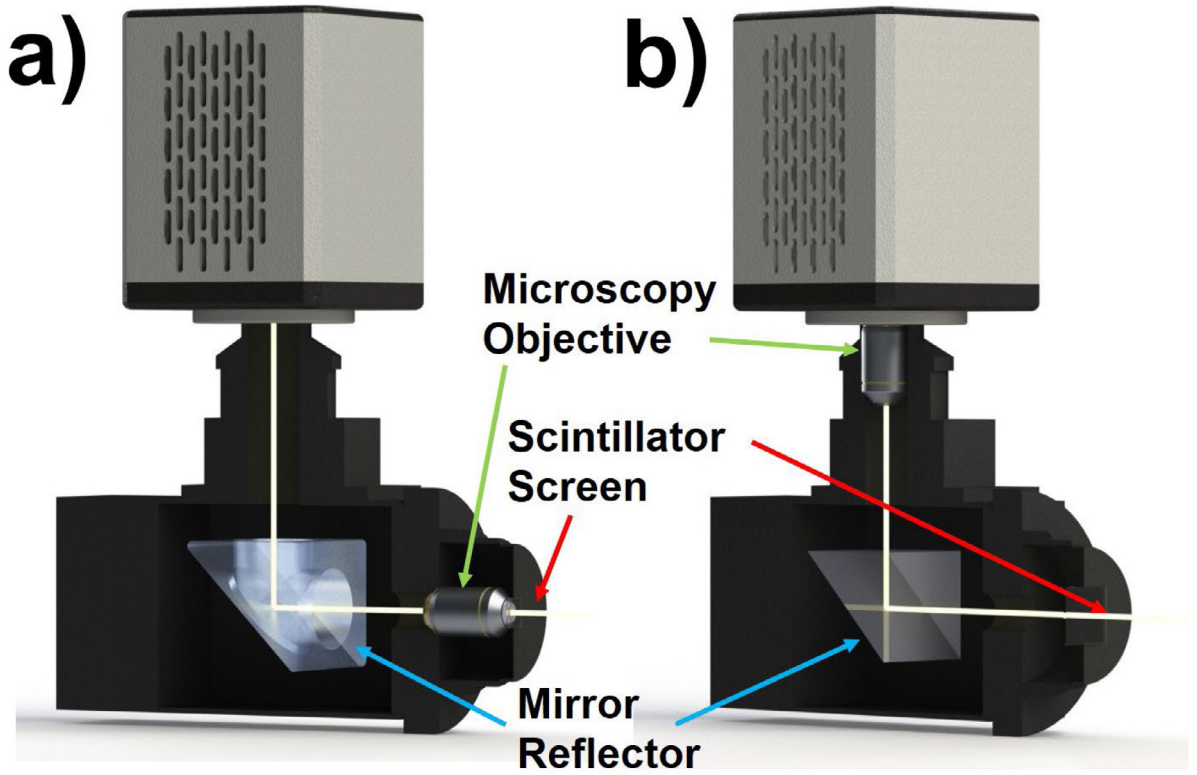

Fig. 8. Optical layout of an X-ray imaging system using X-ray-to-visible conversion. In the configuration (a) the microscopy objective is placed directly behind the scintillator screen and risking X-ray damage. The lens is placed behind the mirror reflector in configuration (b) but requires longer working distances and therefore lower NA (Numerical Aperture) and lower resolution.

The X-ray-to-visible conversion, being very effective, largely compensates the handicaps of magnifying X-ray lenses [74,75]. For example, the transmission X-ray microscopes [76–78], shown in Fig. 9, achieved with this approach ∼16 nm resolution [54,79], notably using a >200x X-ray Fresnel zone plate lens.

Fiber optics taper coupling

Without a complicated optical system, most of the X-ray cameras integrate the scintillating film directly with a CCD or cMOS sensor. This not only simplifies the detecting system but also reduces the loss of photons caused by the microscope objectives and by other optical components. The magnification or demagnification of the visible light image generated by the scintillator screen can be achieved by coupling a tapered fiber optics from the X-ray sensor layer (the scintillator screen) to the visible light imaging device (see Fig. 10).

By aligning each bundle to the pixels of a CCD or a cMOS sensor, the tapered bundles provide magnification or demagnification like a visible-light microscope objective, with very high efficiency. It is also possible to couple a thick pixelated scintillator screen matching each scintillator pixel with the fiber optics to increase the X-rays-to-visible conversion efficiency.

This type of detection currently achieves only limited resolution for X-ray imaging: this reduces its usefulness for SYNAPSE. However, the pixel size (3–30 μm at present) of the image sensors may be reduced in the future with specialized manufacturing technologies. SYNAPSE will follow these developments looking at the possibility of special applications.

One should note that the use of CCD and cMOS technologies to detect X-rays was a major breakthrough along the path to high-resolution radiology with a large field-of-view. Another important element of progress was the increasing number of pixels. The practical consequences discussed later are particularly important for SYNAPSE.

Direct X-ray detection

It is possible to detect X-ray photons directly on a semiconductor imaging device without converting them to visible photons. The efficiency is optimized by fabricating a suitable sensor layer that converts X-ray photons to electrical signals and is linked to readout electronics by metal bump bonding [80,81].

Sensor devices of this kind provide the ultimate performance in terms of sensitivity, reaching single-photon counting. They are already commercially available. However, the current pixel size is not sufficient for the needs of a project like SYNAPSE. One can expect this situation to improve in a short time. Among the important projects in this field, we note Maxipix [82,83], XPAD [84], Pilatus [85] and AGIPD (adaptive gain integrating pixel detector system) [86].

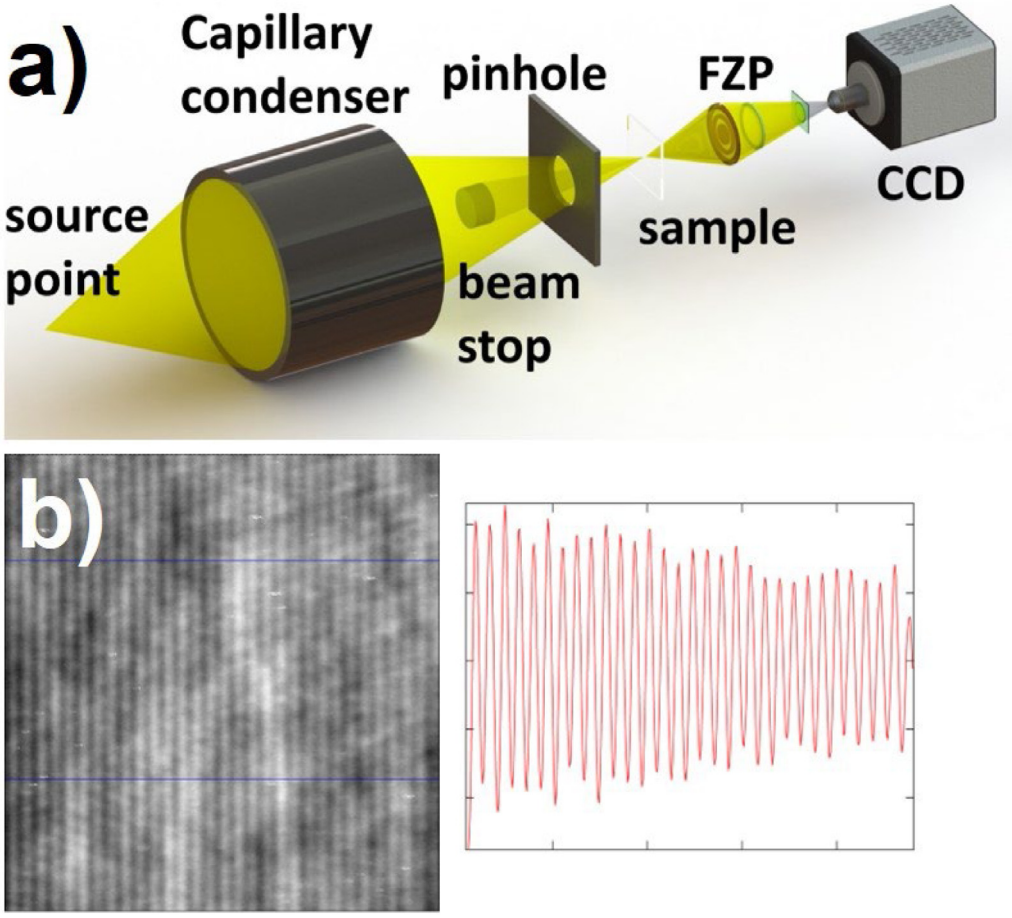

Fig. 9. (a) Schematic diagram of a hard-X-ray Fresnel zone plate (FZP) microscope with the option of Zernike phase contrast. (b) image of a 15 nm pitch test pattern.

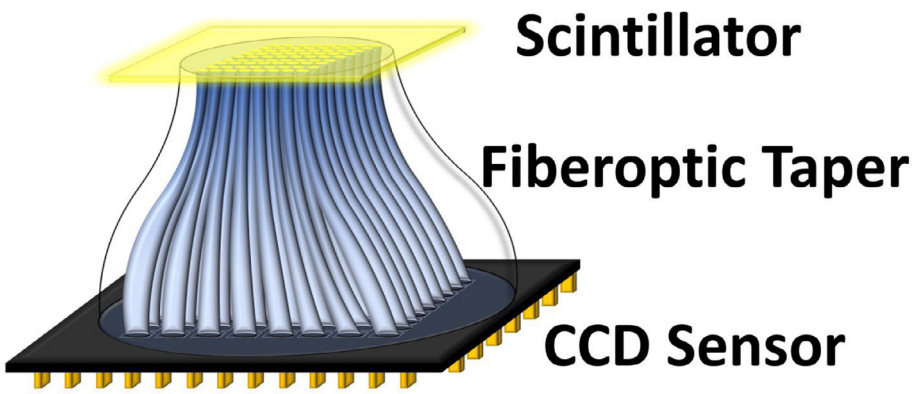

Fig. 10. Schematic of a charge-coupling device (CCD) coupled with a Fiberoptic taper for X-ray imaging.

These detectors are already the foundations of many X-ray diffraction and imaging experiments. The recent progress is based on integrating multiple functions – signal processing and amplification – in a pixel of a cMOS sensor [87]. This benefits spatial resolution and efficiency.

2. Synchrotron based imaging techniques

We already presented in Section 2.1.2 the basic aspects of the use of coherence for phase-contrast imaging. We shall now expand our description of the different X-ray imaging approaches that already have a role in SYNAPSE or may be used for it in the future.

2.1. Real-space imaging

2.1.1. Micro and nano-radiology and tomography

These two full-field imaging methods record the planar distribution of X-rays transmitted through the specimen (“shadowgraphs”) and reveal the X-ray absorption by the corresponding specimen region. They work in a way similar to medical radiology techniques [88].

Tomography uses radiographs taken at different angles between the X-ray beam and the specimen. The 3D distribution of the X-ray absorption by the specimens is extracted by computer processing (“tomography reconstruction”).

The simplicity of the imaging process and the straightforward interpretation of the data make these techniques the most used synchrotron-based real-space imaging approaches [13,89]. They are indeed implemented in all synchrotron facilities. In some cases, they were used for medical diagnosis as a high-resolution alternative to standard clinical radiology [90,91].

We have seen that synchrotron radiation revolutionized radiology thanks to its brightness and to the exploitation of phase contrast in addition to absorption contrast. This notably produced the resolution required for SYNAPSE. As mentioned in Sec. I.2.c, to achieve high resolution, radiology and tomography use X-ray-to-visible conversion. Nanoscale X-ray imaging exploits, in addition, special lenses to magnify the X-ray images, further improving the resolution [76,91].

SYNAPSE takes specifically advantage of the recent developments in this subdomain. Its overall strategy combines imaging at micron level and nanometer level into the same system. This equipment, called AXON (Accelerated X-ray Observation of Neurons), was designed to optimize the speed and resolution for the brain mapping tasks. Fig. 11 shows the schematic diagram of an AXON system and examples of resolution performance.

By capturing the X-rays transmitted through the sample with a scintillator, and then recording the visible images with a high-resolution optical microscope, AXON microtomography (micro-AXON) enable us, for example, to image the interior of a whole fly head at <0.3 μm resolution. With similar procedures, AXON nanotomography (nano-AXON) achieves $\sim$20 nm resolution by magnifying, as mentioned, the projected image with a Fresnel zone plate [76,91].

2.1.2. Micro and nano-probes

Images of the spatial distributions of the chemical components, of their chemical state, of the spin orientation or of other physical quantities are obtained by focusing an X-ray beam on the sample, detecting the relevant signal and scanning the sample with respect to the probe.

One relevant example is scanning fluorescence X-ray microscopy. In this technique, X-rays induce the photoionization of inner shell electrons to form vacancies in a shell, e.g., the K-shell, of a specific element. These vacancies are then filled by the transitions of electrons from an outer shell, e.g., the L- or M-shell. During which, X-ray photons are emitted with energy equal to the difference between the energies of the two shells.

Therefore, the emitted X-ray photon energies are specifically related to the elements in the specimen and can be used to determine their distribution. The fluorescence X-ray photons are captured by an energy-resolving detector, perpendicular to the incoming X-ray optical axis. The resulting “chemical maps” can be quantitative and reach high spatial resolution and high sensitivity. In fact, sensitivity levels of femtograms or even attograms are achievable for low-concentration elements.

Scanning fluorescent X-ray microscopy is now routinely applied in a variety of domains [92,93]. We note, for example, the study of the Alzheimer’s disease inside basal ganglia [94] and of intercellular fatty acids [95].

2.1.3. Fast and ultrafast X-ray imaging

X-ray imaging can achieve high time resolution by using specialized detection systems such as high frame-rate cameras. And by exploiting the pulsed time structure of X-ray sources: picoseconds for synchrotrons, femtoseconds to attoseconds for x-FELs and laser plasma sources. These specialized techniques are closely followed by the members of the SYNAPSE consortium, some of whom are personally involved in the corresponding experiments. They are looking forward to a possible integration of time-resolved experiments in the strategy.

The feasibility of this potential direction of SYNAPSE is not yet established. Indeed, the ultrahigh brightness of ultrashort x-FEL pulses typically damage brain specimens. An alternate approach would be to accept the damage but exploit the short duration of the pulses to obtain the information before it occurs. However, this “detecting-and-destroying” strategy is not feasible in the case of brain specimens since the damage is not localized.

We note, however, that X-ray imaging not using x-FELs is already performed with high imaging speed, >1000 Hz or microsecond exposure times [96–99]. The speed is essentially limited by the number of X-ray photons, in turn determined by the source brightness. X-ray imaging is already used to study dynamic phenomena at the microsecond to nanosecond level [100,101].

SYNAPSE is not targeting dynamic phenomena at the present stage. However, it does profit from high imaging speed — which determines the time required for a tomographic image. The current performance of <0.1 s per projection image achieved with AXON systems is already optimal considering existing mechanical constraints.

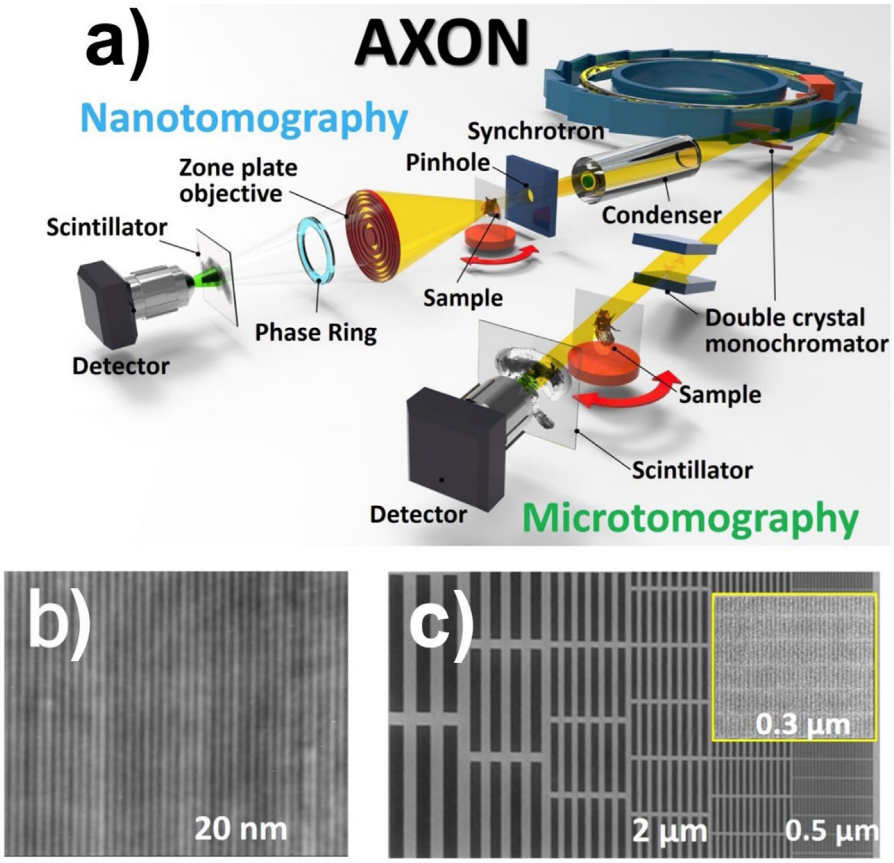

Fig. 11. AXON instrumentation and spatial resolution. (a) Schematic picture of the two types of synchrotron beamlines used for AXON: on the left, a nanoresolution transmission X-ray microscopy facility, and, on the right, a microtomography facility. Bottom: images of test patterns whose smallest features are 20 nm (b) and 0.3 μm wide (c), showing that the spatial resolution of the microtomography (nanotomography) beamlines is sufficient to detect submicron (nanometer) features.

2.1.4. Spectromicroscopy

The advanced characteristics of synchrotron sources led to a series of new experimental techniques investigating chemical and physical properties on a microscopic scale. Although developed for materials science, such techniques find increasing applications in other domains — and is quite useful for biomedical research. We are considering them for possible integration in SYNAPSE.

One important case is X-ray spectromicroscopy. By combining high lateral resolution to spectroscopic analysis, this technique can nondestructively deliver detailed chemical information on a scale down to nanometers. X-ray spectromicroscopy can be implemented in a tomographic mode, becoming quite useful, for example, in the analysis of cultural heritage specimens.

Complementary to X-ray spectromicroscopy are the spectroscopic versions of microscopy techniques in other spectral ranges. Spectroscopic imaging has been proved to achieve 3D rendering, e.g., in Raman microscopy [102], infrared (IR) microscopy [103] and mass spectrometry [104].

One challenge within spectromicroscopy techniques is to normalize the signal-to-noise ratio between 2D images stacked for 3D rendering. This is specifically relevant to the comparison and merging with X-ray imaging results, discussed later and can potentially be a potential problem for the future development of SYNAPSE, that might also include the use of different spectromicroscopy techniques.

Indeed, SYNAPSE already includes a strong collaboration with parallel projects using infrared spectromicroscopy [105,106]. This technique has a great potential for analyzing large samples (typically tissues) because of high-efficiency focal plane array detection and rapid acquisition with high signal-to-noise ratio.

2.2. Coherent diffractive imaging (CDI)

The coherence of synchrotron radiation paves the way to a powerful class of imaging techniques whose relevance to SYNAPSE is under analysis. These techniques are collectively known as CDI.

Diffraction patterns recorded at a far-field geometry with coherent visible or X-ray illumination contain the entire information about amplitudes and phases caused by the interaction of the wave with each point of the object. In 1948, Gabor proposed that the complex wave functions could be extracted by reconstruction of the diffraction patterns, with resolution not limited by the lens aberrations [107].

For X-rays, we have seen that lenses are difficult to fabricate and with technical limitations. Therefore, CDI is better implemented without lenses. The strategy is based on performing inverse Fourier transforms of the diffracted waves.

The problem is that the experiments do not detect the complex diffracted waves but only their intensity, corresponding to the wave amplitude. The information about the phase is missing, creating the so-called "phase problem". Different approaches have been invented to solve the problem, some of them taking advantage of the different wavelengths emitted by a synchrotron source. The phase problem is, in general, a very active area of research [108–114].

CDI can strongly profit from the ultrahigh peak brightness and coherence of x-FELs [115–121]. As an example, we exploited in a test experiment x-FEL radiation to image ∼100 nm liposome particles in water — even though they consist of weakly scattering biomolecules. The diffracted intensity was sufficient for CDI reconstruction, which yielded quantitative information on individual particles [122] and on drugs carried by them [123–125]. These results indicate that we could image cell vesicles in neurons relevant to brain functions, a performance that could be interesting for SYNAPSE.

Reconstruction

The possible use of CDI for SYNAPSE justifies the efforts within the consortium to improve the reconstruction methods. The first step of the strategy is to reconstruct the real space image to generate random phases and combine them with the amplitude information from the reciprocal space pattern. Then, a Fourier transform is applied back and forth to transform images between real space and reciprocal space — with the squared modulus of the diffracted wave field set equal to the measured diffraction intensities in each cycle.

By applying various constraints in real and reciprocal space, the pattern evolves into an image after enough iterations of the so-called hybrid input–output process [119]. To guarantee reproducibility, the process is repeated with new sets of random phases for each run, over hundreds to thousands of cycles [126–129]. The results on test specimens are rather encouraging.

This progress notwithstanding, it is not yet clear what role CDI (with or without x-FELs) will play in brain mapping within SYNAPSE. Indeed, the aforementioned specimen damage problem is still an unexplored issue.

Note, however, that CDI can be implemented with a synchrotron source rather than with an x-FEL, without targeting atomic resolution and using a fixed specimen that allows longer X-ray exposures. The corresponding method is called "ptychography" [130–133]. We are watching its progress and assessing its potential interest for SYNAPSE [134,135].

3. Examples of applications of advanced X-ray imaging

3.1. Microradiology and microtomography

The development of the SYNAPSE strategy takes place in a wider environment in which imaging techniques are applied to a broad variety of issues in different disciplines. Knowing this environment is important to assess the development of techniques that could be imported to SYNAPSE — and also the potential impact of the SYNAPSE developments in many disciplines. We shall present here some examples coming from the research of members of the SYNAPSE coalition.

We shall specifically illustrate the advantages of X-ray microimaging using selected applications different from brain research. This will notably confirm that the most important characteristic of X-rays for imaging applications is their high penetration in solid objects. When coupled with high spatial resolution and with coherence, this feature yields a very powerful probe with diverse and very extended applications. We have seen, indeed, that flux and brightness are not the only positive characteristics of synchrotrons and free electron lasers, since coherence is playing an increasingly important role.

Note, by the way, that high flux and brightness can sometimes be a mixed blessing. X-rays can damage the specimens. Caution must be exercised to guarantee that radiation effects are limited.

As a consequence, radiology and tomography with synchrotron radiation are still mostly confined to non-living specimens. The limited applications to live animals are further complicated by legal and ethical requirements. All the relevant handling procedures and the formal authorizations of all involved authorities are required. Dealing with such complications is justified by the potential impact of imaging experiments that may be indeed very important for the study of diseases with high impact on society.

A common characteristic of the examples presented here is the coordinated use of multiple synchrotron techniques. This illustrates the remarkable versatility of X-ray imaging. And it also highlights its role as the coordinating technique for the integration of the results from other imaging techniques not based on X-rays. The three-dimensional structures revealed by X-ray microtomography are excellent frames to incorporate other kinds of information. This fact strongly influenced the connectome mapping strategy for SYNAPSE.

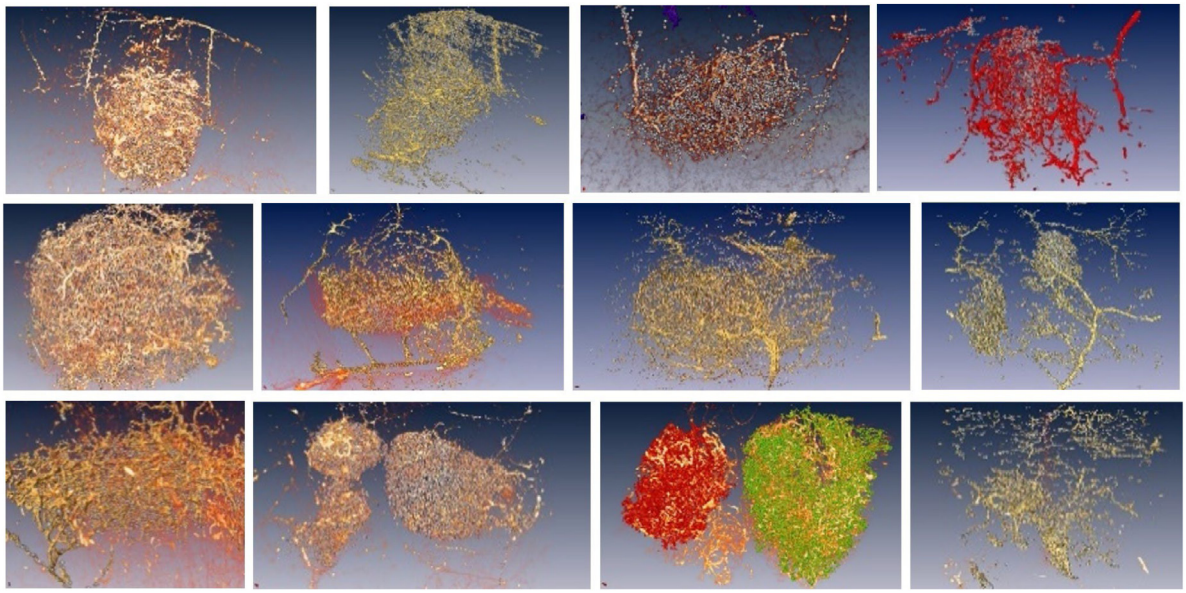

Fig. 12. Tomography reconstructed images of solid-tumor-induced angiogenic microvessels.

3.1.1. Microvasculatures

This was one of the first applications of the enhanced imaging performances made possible by synchrotron sources [136–138]. Indeed, microvasculature studies were not previously possible because of the insufficient resolution and/or the limited 3D imaging capabilities [139].

To yield useful results, microvascular analysis must be extended to blood vessels as small as 3–4 μm in diameter. Such microvessels cannot be imaged by magnetic resonance (MRI), CT scans, ultrasound imaging, or other visualization methods, whose typical resolution levels are hundreds of microns.

Electron microscopy and visible microscopy can of course reach higher resolution. However, for building three-dimensional images they must rely on sectioning the specimens and imaging many consecutive slices.

This line of research specifically analyzed tumor-induced microvasculatures. The background of the research was influenced by the 1971 work of Folkman et al. who proposed that the growth of tumors depends on angiogenesis [140]. It was shown that an imbalance exists of pro-angiogenic and anti-angiogenic factors that allows the development of an abnormal vascular network. Histological studies revealed numerous dilated vessels in angiogenic tumors [141]. This produces a heterogeneity in the tumor blood flow, and consequently an abnormal oxygenation and nutrient uptake, accompanied by increased tumor interstitial fluid pressure [142].

These discoveries inspired anti-angiogenic therapies [143,144], trying to block the development of anomalous blood vessels in growing tumors. The approach was notably developed for brain glioblastomas, a type of tumor extremely difficult to treat with other therapies. Unfortunately, glioblastoma multiforme did not respond as hoped. A shift from mostly solid towards more infiltrative tumor forms often occurs, and the survival time does not significantly improve [145]. It is now even assumed by some authors that anti-angiogenic treatments stimulate this trend [146].

To clarify these and many other issues, it was necessary to investigate in detail the differences between normal and tumor-induced microvasculatures. This required probing the vessel network morphology on the large scale of an entire tumor, also analyzing the functionalities [147]. In turn, the study requires a quantitative imaging technique able to characterize microvasculatures with micron-level resolution [138]. The images must be mathematically analyzed to determine the three-dimensional distribution of the morphological vessel features.

Note the similarities between these requirements and those of whole-brain imaging in SYNAPSE. In both cases, high resolution and excellent three-dimensional imaging are necessary. Plus, sophisticated mathematical analysis must be used to extract useful information. Of course, the challenges created by whole-brain mapping are much more severe.

For glioblastoma microvasculatures, the technical problems were solved by using high-resolution microtomography and different tumor phenotypes. Their microvasculature organization and shape at different growth stages were analyzed. Synchrotron microtomography (Fig. 12) demonstrated the capability to image minute microvasculatures in healthy and tumor-related mouse brain tissues. A powerful mathematical image analysis method was developed to extract a series of morphological vessel parameters.

This experimental strategy was made possible by the use of Au nanoparticles in solution as contrast agents [148,149]. The achieved imaging performance notably allowed the study of large volumes as required for reliable quantitative

analysis. Note that >80% of the brain microvasculature consists of vessels with a lumen dimension <5 μm [150,151]. This quantitatively defines the required spatial resolution, which can only be achieved using a synchrotron source.

The nanoparticle decoration was essential for improving the contrast. Here again, this fact is relevant to SYNAPSE: we shall see that new staining methods based on nanoparticles are a key part of its plans.

The mouse glioblastoma microvasculature studies were crowned by success. A key result was obtained by accurately measuring the microvasculature volume and comparing it to the tissue volume. This included tissues inside the tumors, at the tumor periphery and healthy tissues. It was discovered that the vasculature-to-tumor volume ratio does not detectably change with the tumor size. The ratio is different for angiogenic, cooptive, and mixed-form glioma tumors. But, for each kind of tumor, it stays constant at different stages of tumor growth.

3.1.2. Tumor imaging

Results relevant to SYNAPSE were also obtained by efforts targeting the imaging of some solid tumors that have different density than the surrounding tissues and can be detected by X-ray imaging [152–154]. For example, lung tumors could be imaged with excellent resolution, revealing a wealth of details thanks to phase contrast. Specifically, tumors with size <1 mm could be clearly imaged in live mouse lung [155], a result possibly relevant to early cancer detection.

3.2. Nanoparticle synthesis with synchrotron radiation

Synchrotron sources find an important role in radiology parallel to the direct use for imaging: they are used for irradiation to stimulate the synthesis of metal nanoparticles [156,157]. This is quite relevant to brain mapping, which uses such nanoparticles as contrast agents.

Nanoparticles can be synthesized using a vast array of different methods that employ chemical, physical, or biological processes [158–160]. In our case, the use of synchrotron X-rays opens a potential route for producing size-specific nanoparticles [161–165] that can be used as image enhancers [166,167] — and also for disease treatment [168–172].

In-particular, gold nanoparticles have properties that set them apart. First, their absorption-to-scattering cross-sections can be tailored depending on the nanoparticle size and morphology [148,173,174], facilitating high contrast imaging.

Second, Au nanoparticles are highly stable in solution and have low toxicity allowing high concentration and accumulation in tissues for high-contrast X-ray imaging [175]. Third, stable Au nanoparticles can be synthesized "bare" [176], allowing surface functionalization for biomedical applications [177,178].

The synthesis of metal nanoparticles via X-ray irradiation starts from the aqueous solutions of precursors [157,161–165]. Intense unmonochromatized synchrotron X-rays [179] are used to reduce the metal ions in the solution and synthesize large quantities (liters) of nanoparticles requiring no reducing agents and surfactants in the aqueous solution. Most of the excellent properties, i.e., long shelf-life, high nanoparticle concentration, tunable size distributions, can be attributed to the extremely fast radiolytic reduction effect of the very intense X-rays avoiding any undesired nucleation and clustering of the bare nanoparticles.

Besides acting as contrast agents, by fast passivation and functionalized surfaces, very small nanoparticles, ∼nm size, producing bright fluorescent visible light are ideal for labeling [178] for multimodal imaging important for SYNAPSE. Moreover, stable ^{197}Au, can be transformed into ^{198}Au and ^{199}Au through neutron irradiation using a research reactor [180,181] producing β and γ-rays. The γ-rays that can be captured to reveal the emission location in an animal body with high accuracy, again a unique feature facilitating multimodal imaging.

3.3. Time-resolved X-ray imaging and tomography

As mentioned, the high brightness of synchrotron X-rays is the key factor that makes SYNAPSE brain mapping possible. Fast imaging also enables imaging with high time resolution – with or without x-FEL's – an integrated part of the SYNAPSE strategy. We present here results studying the fast dynamics of the liquid drops on solid and liquid surface to illustrate the potential of time resolve study.

Phase contrast X-ray microradiology was notably used to analyze the dynamics of bubbles and liquid drops, frequently observed in everyday life [182–186]. Time-resolved microradiology could directly image the entire processes of drops impact on solid surface [187] on the scale of microns and microseconds, revealing complex dynamic features [188,189]. Upon hitting a solid surface, a liquid drop can spread, splash, break up, or bounce. X-ray images captured first the evolution of an entrapped air film into a bubble on the scale of 100 microsecond [190].

The analysis of the images shows the formation of the pinch-off of the liquid channel and daughter droplets in the bubble that is attributed to a contraction process driven by the surface tension of the water droplet. A critical value of the relevant parameter was derived, above which the pinch-off does not occur, as verified for different liquids.

While the drops hit a liquid pool, the evolution of the entrapped air, and the dynamics of the entrained air display very different phenomena [191,192]. High-speed experiments on a variety of liquid pools revealed two retraction mechanisms of the entrapped air film: inertial and viscous depending on the liquid viscosity [193–195].

These findings can be used to predict the morphological evolution of the entrained air under different conditions. The success of applying high speed imaging with X-rays also opens the door for higher image throughput and the potential to study live specimens without relying on heavy metal staining.

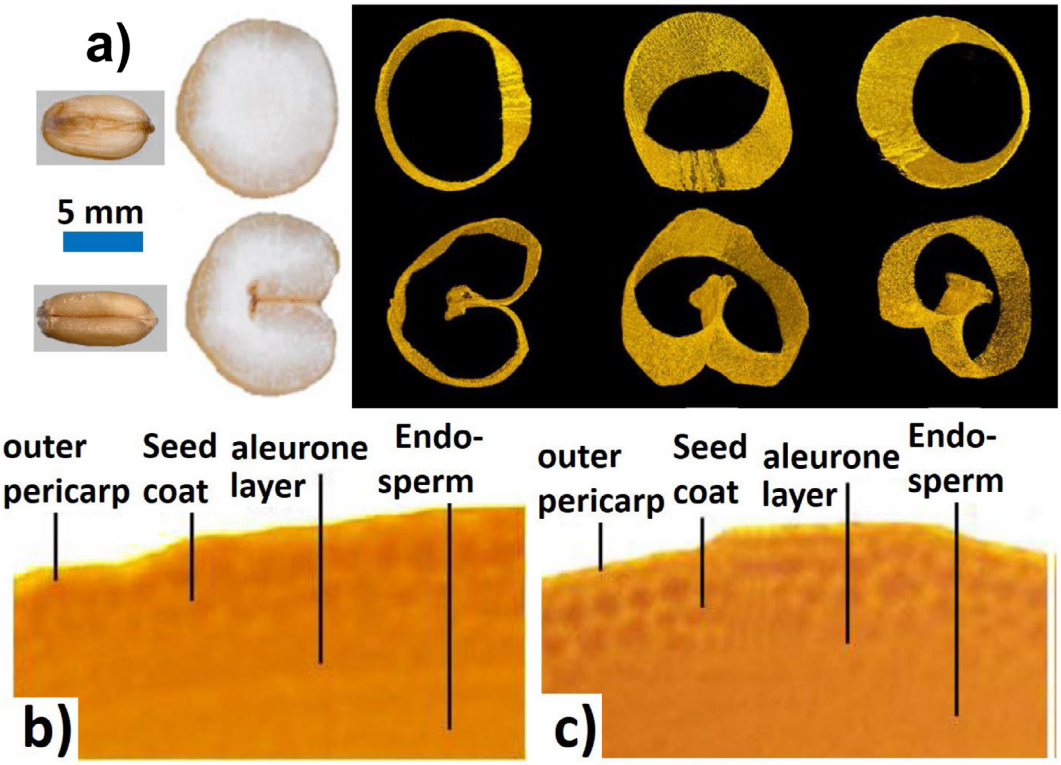

Fig. 13. (a) Microtomography images of wheat grains. The creaseless wheat grain has a rounded shape (top), and normal wheat grain (bottom) has a deep crease. (b) Cross-section views of the wheat bran region of normal wheat, and (c) creaseless wheat. The outer pericarp, seed coat, and aleurone layer, where most nutrients are found, are still present on creaseless wheat, but removed by the excessive milling of normal wheat grains. Images obtained at the BL 13W1 beamline of Shanghai Synchrotron Radiation Facility (SSRF).

3.4. Plant biology and food science

X-ray imaging is widely used for plant specimen studies — for example, the observation of water transport within a plant xylem and phloem. This requires imaging internal microstructures in live condition — which was one the first applications extending the scope of microradiology on biology specimens. High lateral resolution is critical to these experiments as well as high time resolution.

Here one can see the advantages of combining X-ray imaging with other experimental tools. For example, the elemental distribution in plants was obtained with synchrotron X-ray fluorescence microscopy [196] and microtomography [197]. For example, the distribution of contaminants was shown from the phytoremediation of polluted soils [198].

This kind of strategy is an excellent example of multimodal imaging, demonstrating the integration of different kinds of information provided by different synchrotron X-ray techniques. One particularly interesting application of X-ray imaging is the study of grains, obviously important for human wellbeing and the economy.

One example is the study of creaseless wheat, developed by combining variable frequency microwave radiation and phytohormones treatment [199,200] and aiming to increase the wheat flour yield by reducing the waste of milling the wheat grains with crease. Fig. 13 shows that the crease was completely absent leaving only slight trace on the grain surface. X-ray fluorescence images, Fig. 13b and 13 c, confirmed that more nutrients, as much as 12% with respect to regular wheat, are preserved through the milling of creaseless wheat.

Research on rice also tries to increase productivity and improve the grain quality to withstand stresses due to climate change, diseases or insects — such as the rice weevil that infests grain and rice crops. Development of pest-resistant rice and optimized harvesting times are very important to control the weevil infestation.

The analysis on wheat grains was also applied to rice. The X-ray tomographic images, Fig. 14, revealed the weevil infestation that had penetrated the rice kernel and sealed the holes with a gelatinous substance making the infestation undetectable. High speed tomography would allow fast examination of many grains to identify the pattern of infestation.

Furthermore, high resolution tomography detected microscopic structural changes of uncooked rice after ultrasonication forming microporous surfaces and fissures in milled rice. These changes allow a 28-fold increase of the iron uptake following soaking in a water iron solution and a $>80\%$ retention after washing and cooking. The microstructural

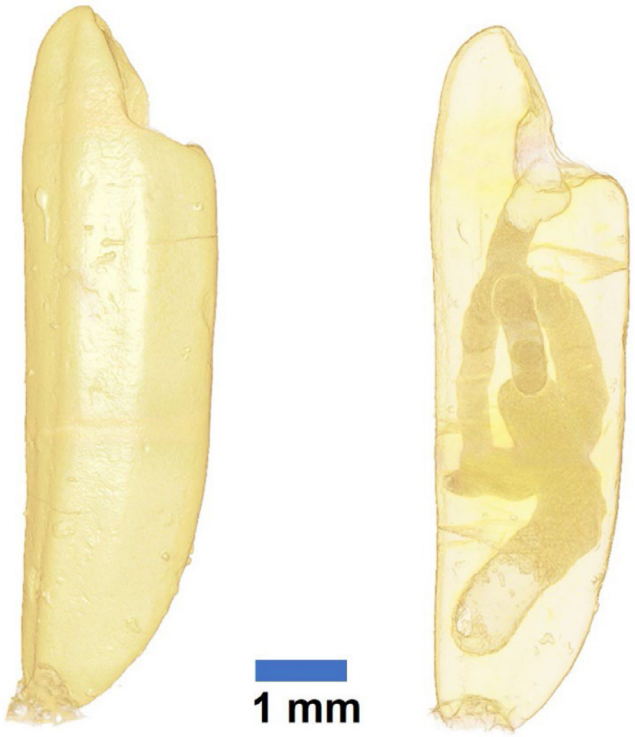

Fig. 14. 3D tomographic visualization of exterior and interior of the weevil-infested rice. Images obtained from the XTM beamline of the Thailand Synchrotron Light Research Institute.

change also affected the textural properties, allowing the easy penetration of water during cooking and promoting a softer texture [201].

Cross-sectional micro-X-ray-fluorescence mapping of uncooked grains showed that the distribution of nutrients in rice grains is also highly inhomogeneous and, furthermore, the inward diffusion of iron fortifying agents at different rates, reaching the kernel core.

3.5. Human heritage and paleobiology

Shortly after synchrotron X-ray imaging reached high resolution and high contrast, it started to be used to analyze issues relevant to human heritage and paleobiology specimens, such as fossils, yielding very interesting results [202]. Synchrotron X-ray tomography examination is now a standard procedure in paleobiology.

There are requirements similar to brain imaging to perform these studies. The specimens for human heritage research and paleobiology are often rare if not unique. Sectioning them to examine the microstructure in three dimensions is seldom an option. Tools to non-invasively examine the internal structures of large and small samples with sub-μm resolution are needed.

3.5.1. Internal structures of minute fossils

One example of these studies is the analysis of fossils of marine spiralian animal embryos [203]. These microscopic specimens preserve minute details at the cellular level, allowing considerable insight into the embryonic and larval stages of many early microanimals.

For example, X-ray microtomography detected signs of bilateral symmetry in many of the fossils. The evolution to animals of bilateral symmetry, a common feature in many present-day animals, was considered later than the Precambrian period, during the "Cambrian Explosion" [204]. The tunnels in Fig. 15, likely the "foot-print" of a infested animal, however, are bilaterally symmetrical as far as their cross section is concerned. This suggested that these bilaterally symmetrical animals might have appear in these Weng'an fossil specimens dated as at least 580 million years old [205–208].

The most interesting results obtained with synchrotron microtomography concerned the embryo development. Fig. 15(b) and (c) shows such an example: the polar lobe formation is one of the symmetry-breaking mechanisms that segregates maternal cytoplasmic substances only to certain blastomeres and not to others.

These fossil embryos similar to present lobe-forming embryos have been found in the Weng'an site. Microtomography results interestingly imply that lobe formation is an evolutionarily ancient process of embryonic specification [209,210].

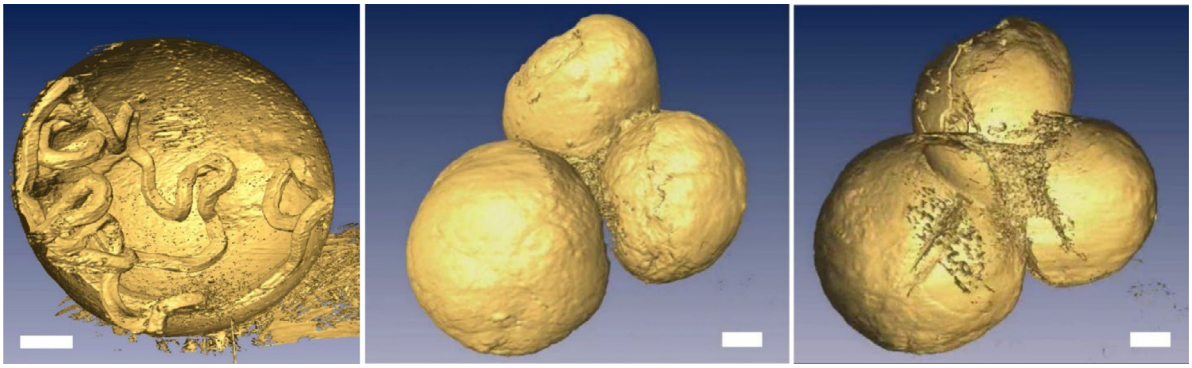

Fig. 15. (a) 3D-reconstructed microtomography image of a microfossil with tunnels inside. The clear bilaterally symmetrical cross section of those tunnels suggests that they had been formed by bilaterally symmetry nematodes embedded in the fossil embryo. (b) Surface rendered microtomography images of a cluster of microfossils and (c) image made transparent showing the lobes are connected. Scale bars: 100 μm.

3.5.2. Imaging ancient manuscripts

In the domain of human heritage, the analysis of ancient handwritings plays a key role to process the corresponding huge collections which are only marginally exploited. Digitization often requires handling the specimens in a potentially destructive way.

These challenges are very similar to those affecting the brain mapping. Indeed, there are many other techniques can provide detailed information on a macroscopic specimen, but the speed of processing limits the full exploration.

What makes synchrotron tomography applicable to ancient handwritings in the first place [211,212]? This is a fortunate fact: for more than a millennium, most of the European manuscripts used inks containing iron, an X-ray-absorbing element. The compositions varied but guaranteed the iron presence. The corresponding inks are collectively known as "iron gall inks". This fact provides the high contrast, much like the Golgi staining for the brain mapping with X-rays.

The marked advantage of X-ray tomography is the possibility to image entire volumes without opening them. Very fast 3D imaging, therefore, provide the incentive, similar to the brain mapping. Then, advanced reconstruction techniques can extract the writings page-by-page. This approach can be also applied to particularly difficult specimens like ancient, fragile scrolls.

Extensive chemical analysis verified the presence of iron in different specimens over several centuries [213]. Real specimens were then analyzed revealing internal characters and words without opening them. The results were quite interesting and fascinating. In one case, the analysis was applied to the testament of the Venetian lady Catharuçia Savonario, unopened for many reasons, including a legal one, for seven centuries [214].

These studies stressed the importance of multidisciplinarity, which is a ubiquitous requirement for synchrotron tomography and in particular for brain mapping. In the case of lady Catharuçia's testament, the revealed text is often so abbreviated that makes no sense without the analysis of specialists. Tackling these problems required indeed the contributions of experts in literature and history.

With the manuscript-reading techniques ready for large volumes, the condition of specimen, such as page warping and the slow deterioration of the writings, remain non-negligible problems, again similar to those affecting brain mapping. Such problems often require a massive use of computer analysis and other specialized instruments.

3.6. What we can learn

What is the message of the above examples? In essence, they demonstrate the imaging techniques for SYNAPSE, are very advanced, and well beyond the exploratory stage.

They are, in fact, used to tackle a variety of issues in different disciplines. And they illustrate the power and versatility of synchrotron tomography, in particular in its micro and nano versions.

In essence, these tests demonstrate that the SYNAPSE strategy relies on a solid and established technical background. Furthermore, their results show that the SYNAPSE partners are fully qualified for the task, having developed hands-on experience on the necessary techniques.

This does not mean that the road to SYNAPSE is devoid of obstacles, but only that such obstacles are not insurmountable. Among them, we should note the computing aspect related to the sheer mass of data, to be discussed later.

4. Brain mapping with X-rays: Scientific justification and detailed assessment

4.1. General background

The current experimental situation illustrated above creates the opportunity to progress towards the "holy grail" in science that constitutes the objective of SYNAPSE: mapping with X-rays individual cells and their connections in whole large-animal brains [215–226], including human ones. Until recently, the issue did not really exist because of the estimated very long total time to obtain a comprehensive map. The evaluations reached indeed centuries.

However, our evolving X-ray imaging techniques now reach a speed that makes the task reasonably feasible. Even though, before presenting new estimates, we must carefully define what is "the task" within the SYNAPSE initiative. This definition is also necessary to explain why the task is important and justifies the required, massive efforts.

Realistically speaking, SYNAPSE cannot – at least in its first phase – map the entire human brain down to the individual signal channels. However, it will provide new information well beyond present knowledge.

Based on our present performance, this initial task is feasible and can be completed in a few years. Indeed, with the demonstrated X-ray imaging speed of 1 mm^3/min, analyzing one entire human brain will take less than 1000 days.

Note, however, that mapping one whole human brain with present experimental strategies will not provide "the" map of the human brain. In fact, conventional staining only allows detecting a portion of the neurons and of their connections. Even with the most optimistic improvements of the staining procedures, this portion will remain limited. Thus, a comprehensive map will require analyzing a rather large number of individual brains — of the order of 100.

This task would be prohibitively long with the present imaging speed. However, three facts must be considered to obtain the correct perspective. First, the speed performance of our techniques did not yet reach their ultimate levels. There is much room for improvement, and this is why working for more rapid imaging is an essential part of the SYNAPSE strategy.

Second, the overall mapping time can be shortened by analyzing specimens at different synchrotron facilities, in parallel and in a coordinated fashion. This is indeed the pillar of the SYNAPSE strategy. The coordination is a formidable challenge, but the expected results fully justify the efforts to achieve it.

The third positive factor is that the results of SYNAPSE, even from its first stage, will open the door to reverse engineering of the brain. This is similar to a hypothetical reverse engineering of silicon-based computers, starting from maps of their circuitry as the first step.

Summarizing, the path of SYNAPSE will first target the analysis of one partially stained human brain and then tackle the challenge of a complete map by analyzing many brains. The first phase is already underway and has been preceded by concrete achievements. These are not limited to the example illustrated by the previous chapter but extend to cases directly dealing with brain mapping.

Indeed, using the AXON instrumentation we implemented an innovative strategy, combining synchrotron X-ray microtomography and optimized staining. More specifically, the strategy relies on two different AXON instruments combined in the same system: micro-AXON and nano-AXON.

As already outlined in Section 2.1.1, micro-AXON projects X-rays through the sample onto a scintillator and then captures the visible light images with a high-resolution optical microscope. This method images the interior of a large specimen with <0.5 μm resolution. We have also seen that Nano-AXON reaches, instead, $\sim$20 nm resolution by magnifying the projected image with a Fresnel zone plate. And it also enhances the contrast with a Zernike-type phase ring. To overcome the limitation of the field of view (FOV), multiple projection images can be combined, specifically for neuron fibers extending over a large volume.

The combined instruments work best by using nano-AXON to zoom in the regions of interest, previously identified by micro-AXON. The three-dimensional information carried by the projection images can be extracted by tomographic processing [227]. Such a processing typically requires large sets of two-dimensional images for different specimen-detector geometries, obtained by rotating the sample and/or the detector. Specialized computer programs convert such images into 3D information without deteriorating the resolution.

An important activity prior to SYNAPSE was the use of the above strategy to investigate the brain of Drosophila. This was a very useful exercise, practically demonstrating the feasibility of the strategy for brains of limited size and with less components than those targeted by SYNAPSE.

4.2. Why does brain mapping matter?

This is a key point and a rather controversial one. Will mapping contribute or not to our understanding of how the brain works — or malfunctions? After all, microscopic information already clarified the internal processes of a single neuron and the possible mechanisms controlling the information flow. Why is this not sufficient?

Our answer is two-sided: On one hand, the question cannot be really answered in advance, prior to obtaining a good map. This is not an unusual situation for research: plenty of historical facts show the futility of trying to plan in advance all the details of the results of science. Consider for example the experimental foundations of quantum physics. They specifically required decades of work to measure the optical spectra of hydrogen and other elements, with no guarantee that the results would be useful.

And there is another facet to be considered. There is plenty of evidence that a mere "reductionist" approach based on microscopic information about the "building blocks" will not be sufficient to really understand how the brain works. Macroscopic-level information is also required, specifically including the structural information that will be provided by SYNAPSE.

This conclusion was discussed in great detail by Sporns, Tononi and Kötter [215] and by Morgan and Lichtman [228]. The last article is particularly interesting, since it takes one by one all the standard attacks against brain connection mapping ("connectomics") and presents convincing counterarguments. This is not, in our view, a demonstration that mapping will eventually contribute to the understanding of the brain: as mentioned above, such a demonstration will only arrive after the fact. But Morgan and Lichtman did demonstrate the fallacy of the arguments used to impede this effort even before any mapping is attempted.

Without trying to add more elements to the lucid and complete argumentations of Ref. [228], we would like to explain here why we believe in the need for comprehensive macroscopic-level information, as a prerequisite for really understanding how the brain works. Our belief is based on two lessons from the history of physics.

The first is the development of superconductivity. Below its transition temperature, a material is in a superconducting state. This is not just the state of a "good" conductor, but is characterized by other properties besides zero resistance, notably the magnetic "Meissner effect". The nature of the superconducting state is still largely unknown, and the situation was complicated by the discovery of high-temperature superconductors.

What is clear, however, is that the superconducting state cannot be constructed from the properties of individual electrons. The facts demonstrating this impossibility are striking. Consider for example the so-called "coherence length", one of the main characteristics of the superconducting state. In the so-called "BCS" (Bardeen–Cooper–Schrieffer) theory of superconductivity, the coherence length roughly corresponds to the size of the "Cooper pairs", formed by electrons interacting through phonons.

For aluminum, the coherence length reaches 1.6×10^{-7} m, which corresponds to a volume of 4.1×10^{-21} m^3. This volume contains 2.5×10^9 core electrons and 7.4×10^8 valence electrons. One cannot, therefore, imagine the superconducting state as a mere perturbation of individual electrons that largely retain their properties.

The state is instead a collective electronic feature. Similarly, brain mapping may reveal structural features involving many neurons and synapses, making it impossible to consider the brain as a mere combination of independent components.

The second lesson from the history of physics is related to particle accelerators, including the storage rings used as synchrotron radiation sources of X-rays. Treating the accelerated particles as individual entities cannot explain how the machines work. Collective phenomena dominate, in particular in the instabilities that determine the accelerator properties and must guide its design and operation.

Ignoring the collective aspects would be a pointless exercise. Likewise, a brain composed of neurons working independently is a pointless exercise far from reality.

This is why comprehensive mapping is a worthy enterprise. But a very challenging one. There are in a human brain more than 80 billion neurons, each with thousands of synapses connecting them to many other neurons. The result is a massive and extremely complicated network.

These facts explain why the estimates for complete mapping were so far rather pessimistic. One exception has been the European Human Brain Project [229], which adopted a computer simulation strategy. SYNAPSE is based on a different philosophy, targeting real maps obtained with X-ray imaging methods coordinated with other imaging techniques.

More specifically, SYNAPSE is based on breaking down the brain complexity into different levels of connection details based on the known "hierarchical" structure of physically mapped neural networks. The strategy thus includes multiscale, multimodality three-dimensional imaging approaches, targeting each level of the brain structure with a combination of specific tools.

4.3. 3D multiscale imaging

The brain is a 3D system that requires 3D analysis. This is not a trivial point: imaging techniques not based on X-rays may reach high levels of resolution and speed but are not three-dimensional. The limitation specifically applies to electron microscopy — notwithstanding its excellent resolution performance.

Without 3D probes, the experimental solution is specimen sectioning . But this is far from optimal. Not only does it complicate specimen preparation, but it compromises its integrity and the reliability of the information for brain mapping. Furthermore, it significantly increases the duration of the experiments, making once again whole-brain mapping unfeasible over a reasonable time span.

The need for 3D imaging is not the only problem. The use of the information provided by SYNAPSE, which should be open and free for all qualified researchers, also requires the organization of the results in a scalable fashion. This is essentially a philosophy like that of Google maps. To reach the desired information on a specific neighborhood, one does not need a microscopic picture of an entire city or region. The exploration can start from a wide area with limited resolution, progressively increasing the resolution of particular regions of interest when higher magnification is required.

SYNAPSE will work in a similar fashion. Information at the micron level will be obtained for the entire brain, and then coupled to results at the nanometer level available for specific regions of interest. The basic information will be structural and provided by X-ray imaging. But it will not be isolated. Complementary information, notably about local chemistry and functionality, will be obtained with other techniques. The resulting "maps", therefore, will be scalable and will combine structural information with other elements, becoming very useful.

4.4. Why X-rays and why synchrotrons?

We already indirectly dealt with several facets of this question. Which is not irrelevant, since our advanced X-ray imaging requires gigantic instruments like synchrotron sources — which are expensive and complicated to use. One could legitimately ask if the results could be obtained without them.

The answer is negative for several reasons. As already mentioned, X-rays combine high penetration in solids with short wavelengths, which in turn allows high resolution. And advanced X-ray imaging requires a source of high brightness and high lateral coherence. Alternate sources have been routinely proposed over more than half a century. As of today, however, synchrotron sources are the only feasible solution. And they are truly excellent, as explained above.

4.5. Emerging techniques: MAXWELL (microscopy by achromatic X-rays with emission of laminar light)

SYNAPSE leads to a number of interesting byproducts. Among these, we note the realization of innovative instrumentation like AXON. Another recent example is MAXWELL, a new X-ray light-sheet technique developed at SPring-8 (Fig. 16) [230].

Two remarkable factors that make the MAXWELL microscope superior to visible light-sheet microscopes are (i) in-depth resolution of ≈50 nm and (ii) an FOV of ≈400 μm (with a light-sheet width of ≈100 nm), thanks to the tight focusing and large depth of focus of X-rays.

We have shown at SPring-8 that these results are attainable by a Wolter type-I mirror. Biological samples containing Scintillating NanoParticles (SciNPs) were prepared and placed in the focal plane of the X-ray light-sheet. SciNPs excited by an extremely thin cross-section (∼50 nm width) X-rays emit visible fluorescence. Such a distribution is measured with a high-resolution visible microscope placed perpendicularly to the X-ray optical axis.

By translational movement of the sample relative to the X-ray light-sheet, the three-dimensional distribution of SciNPs can be measured for thick biological samples (Fig. 16). Thin cross sectional views are obtained without any special computer algorithm for reconstruction. And MAXWELL imaging is much more tolerant to radiation damage than standard tomography. There is even the possibility to reduce the X-ray focus size to 20 nanometers in the future.

Three more factors make the MAXWELL microscope very attractive for biological research. First, the use of very small, e.g., 10 nm, SciNPs for super-resolution imaging in three dimensions. Second, an effective tissue clearing method. Third, a >20 keV X-ray light-sheet for imaging large specimens. We developed 10 nm SciNP families, $NaGdF_4$:Eu and $NaGdF_4$:Tb, emitting red (∼615 nm) and green (543 nm) light. Hard X-ray focusing with >10 keV photon energies was also demonstrated.

Besides the X-ray-induced phenomena, the visible microscope in MAXWELL makes it possible to implement other fluorescence imaging techniques. For example, the nuclei distribution and the cell outline can be detected by acquiring UV-induced fluorescence images of the specimens with cells stained with DAPI and phalloidin.

This and other techniques can be implemented in parallel to X-ray-induced fluorescence microscopy, delivering complementary information. And the efforts to develop new staining approaches can be shared between different techniques. For example, various ways to conjugate SciNPs to biotin or antibodies are being developed.

We would like to report here one of the first results of the MAXWELL microscope. CHO-K1 Cells (Chinese Hamster Ovary) stained with SciNPs and DAPI were observed. Eu-doped and Tb-doped SciNPs are found to be concentrated inside and at the envelope of the nuclei of HCT-116, as shown in Fig. 17(a), (b). The unique staining performance of our SciNPs and the three-dimensional high-resolution character of MAXWELL, evidenced by this experiment, clearly illustrate the strong potential of MAXWELL for key issues in biology, in particular brain imaging.

5. From SYNAPSE to SYNAPSE 2.0

5.1. The SYNAPSE partnership

We have seen that the present performance of X-ray imaging is promising but not yet sufficient to yield a map of a human brain within a reasonable time. This led, as we have seen, to the coordinated and parallel use of several facilities within SYNAPSE.

An international coalition was thus created including partners in Australia, China, Japan, Korea, Singapore and Taiwan — not only synchrotron laboratories but also four high-performance computing (HPC) centers. Recently, SLRI in Thailand and SESAME in Jordan also joined the collaboration.

On January 15, 2020, representatives of the founding partner facilities and many individual scientists met in Singapore to sign two memoranda of understanding, pledging to use their resources within the consortium for brain mapping [231]. The ambitious objective of SYNAPSE was also announced: mapping the neurons and their connections of one human brain with advanced X-ray imaging techniques.

Presentations from the members illustrated a massive research network and emphasized the need for an international collective effort to meet the challenge of human brain mapping. Just for the images of one human brain, a huge mass of data – exceeding exabytes – will be acquired and will have to be stored and analyzed within a reasonable time.

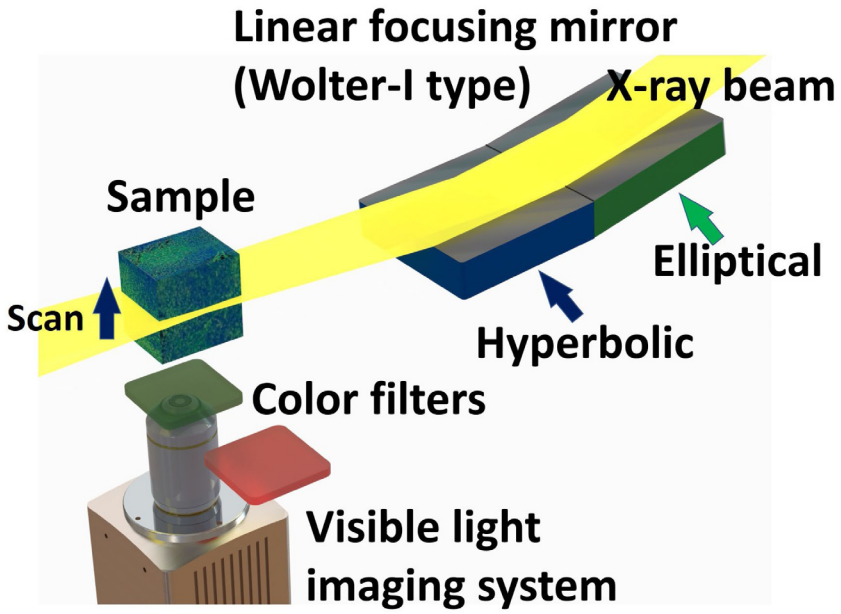

Fig. 16. Schematic diagram showing the MAXWELL experimental setup.

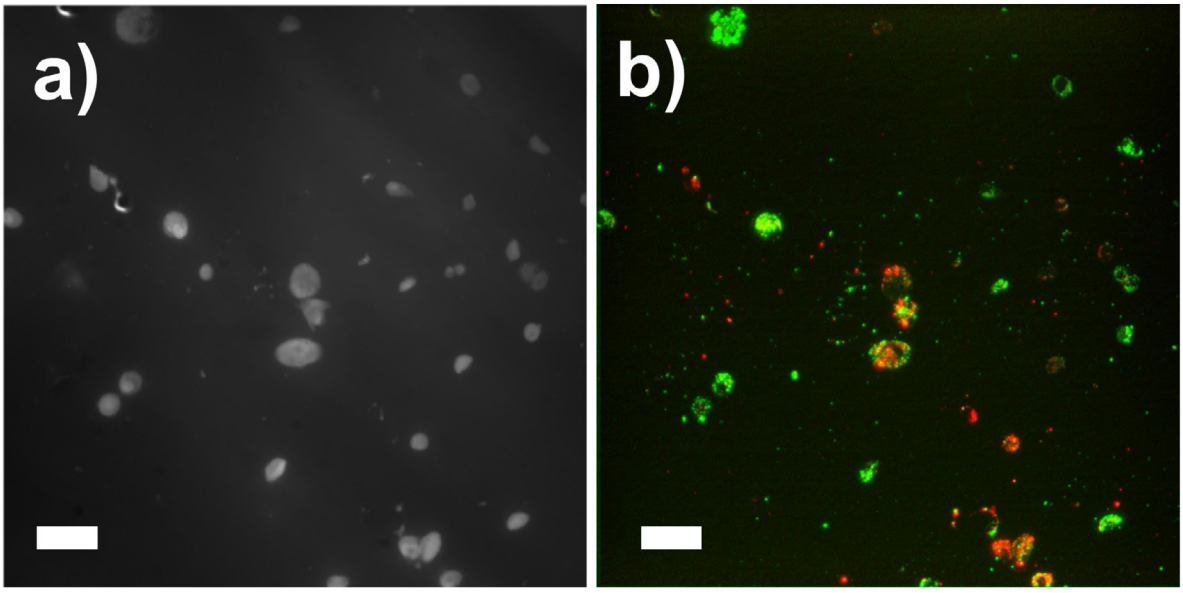

Fig. 17. Images of CHO-K1 Cells (Chinese Hamster Ovary) stained with SciNP (Eu & Tb doped $NaGdF_4$) and DAPI obtained using the visible microscope of the MAXWELL system with a 20x objective lens. (a) DAPI image excited by UV (405 nm); (b) MAXWELL image. Scale bar: 100 μm.

The concrete results of an extensive series of tests were presented to demonstrate the capabilities of the AXON techniques. Excellent imaging performances, including a 0.3 μm sub-cellular resolution and a tomography imaging speed of 1 mm^3 in 3 min, was demonstrated by a large number of three-dimensional data sets of whole brains of mice and fruit flies (*Drosophila*). Based on these performances, the images required for mapping a whole human brain with a volume of $\sim 1.2 \times 10^6$ mm^3 may be taken in 6×10^6 min ($\approx 4.2 \times 10^3$ days, or $\approx$11 years) of AXON experimental time. The SYNAPSE consortium guaranteed the delivery of this beamtime. Furthermore, by working in parallel at several facilities the actual time with respect to the above duration may be shortened, which is still unacceptably long.

The SYNAPSE consortium specifically targets the following milestone objectives in the forthcoming years:

(1) Imaging one entire human brain with 0.3 μm resolution in all three dimensions, mapping primary connections.

(2) Mapping 200 mouse brains with the same resolution.
(3) Developing new imaging and computation techniques to enhance data taking and processing speed by up to two orders of magnitude.
(4) Developing new multimodal experimental strategies to connect structural information with functional properties.

Note the imaging speed of AXON is strongly related to the 10–20 keV photon flux which varies between different sources. Therefore, calibration and cross-verification is critical to guarantee uniform image quality for different partner facilities. This quality is defined as 0.3 μm resolution with good contrast, allowing accurate stitching of three-dimensional tomographic images for different parts of the same brain. This justifies the already operating quality control task force monitoring the operations of all SYNAPSE-based facilities.

SYNAPSE will greatly profit from the interactions with advanced neurobiology/brain science research institutions and its individual member facilities. These interactions are already active. Specifically, the importance of the information that SYNAPSE will deliver was certified by several top neurobiology experts [232] from Switzerland, China, Taiwan, Singapore and Japan. The responses were clearly positive. These experts specifically stated that the results will significantly contribute to the understanding of how the brain works or fails. In general terms, the interactions between the synchrotron and neurobiology communities is establishing functional links even before SYNAPSE starts to deliver its connectome maps.

Concrete collaborations are already underway delivering the first results of SYNAPSE — e.g., data for parts of brains or for a limited number of mouse specimens, at the disposal of neurobiologists linked to associated institutions. These exploratory activities, mostly conceived by the brain science partners, are already playing a positive role in the evolution of SYNAPSE.

Preliminary results of these cooperation projects were presented at the SYNAPSE inauguration event. For example, the main interest of the Singapore neuroscientists in accessing SYNAPSE results is focused on brain aging and the structure-function relationship of the neural network of non-human primates (NHP). The SSRF (Shanghai Synchrotron Research Facility) will concentrate its research on the objectives of the Chinese Brain Initiative — and adapt its strategies to take advantage of the world-leading capabilities in China in genomic/proteomic sequencing and the cloning of non-human primates. These research themes are different from the objectives of SYNAPSE, but their association to the consortium is justified to engage the neuroscience community without delays, preparing the future use of the brain maps.

A workshop on high-performance-computing, HPC, took place after the SYNAPSE inauguration event, illustrating the computational capabilities available for SYNAPSE from the four national facilities in Korea, Japan, Taiwan, and Singapore. Key challenges for the development of HPC for SYNAPSE were identified. This led to the formulation of an international roadmap. The related issues will be discussed later.

5.2. Recent SYNAPSE achievements

We shall now present the progress of SYNAPSE after its inauguration and towards the four above-mentioned strategic objectives. SYNAPSE was of course seriously affected by the COVID pandemics whose start coincided with the inauguration event. In particular, there were severe disruptions of the research-related travel to SYNAPSE member facilities.

SYNAPSE responded dynamically with an adjusted approach and an evolving timeline. Instead of deploying AXON instruments with equal performance in all SYNAPSE facilities, priority was given to improving the imaging performance and gain time by accelerating image taking. Many of the related improvements were implemented and tested earlier than the original plan, becoming ready for deployment at all the SYNAPSE synchrotrons.

5.2.1. Improvements of the AXON systems

Is the present AXON performance adequate or should they be improved? This is of course a central question for the success of SYNAPSE.

And the answer is positive. As shown by the results, in particular those presented at the inauguration event, the objectives of SYNAPSE are no longer a projection to the future, depending on additional technical developments. The AXON performance was indeed already suitable in 2017–18 [233] for mapping individual neurons and their connections in entire *Drosophila* and mouse brains. We also projected that by a coordinated exploitation of this performances at multiple SYNAPSE facilities we can handle large animals – including NHPs – and finally humans.

We also found from our preliminary tests that ample room exists for further improvements. As mentioned, the imaging speed can be increased by 1–2 orders of magnitude [234]. This will enable each AXON system to image a whole human brain in a few days. It will thus become possible to obtain and compare data for a sufficient number of healthy or diseased brains, in order to extract statistically meaningful information. This comparison will be largely performed by artificial intelligence (AI) or machine learning, and will automatically detect minute structural differences between different specimens, linking them to the symptoms and causes of diseases.

In essence, the first human connectome map produced by SYNAPSE for only one brain is a demonstration effort, paving the way to comprehensive maps. The future capability to image a large number of human brains will target instead a complete human connectome. Therefore, the initial period of SYNAPSE is a first step of a long-term effort not limited to one human brain.

The first fully dedicated SYNAPSE beamline, BIB (Brain Imaging Beamline [234]) was commissioned in Taiwan in 2020. Its AXON system now reaches the targeted 0.3 μm resolution with an imaging speed of 1 mm^3/min, exceeding the

original specifications and significantly decreasing the imaging time. These improvements will be transferred to all AXON instruments, scheduled for commissioning within one year.

Imaging Speed

SYNAPSE also implemented and tested new devices to further enhance imaging performance. The key point is, again, to enhance imaging speed. For this, we must first identify what limits the current performance.

The typical intensity from a bending magnet of a 3rd generation synchrotron is $\sim 10^{13}$–10^{15} photon s^{-1} mm^{-2}. This is sufficient for X-ray imaging at a speed of 1 μs per image with 0.2 μm pixels. This imaging speed has been realized in several synchrotron X-ray imaging experiments exploring ultrafast dynamics with lower spatial resolution [101,235]. For a large sample like an entire human brain, 20–40 keV X-ray photons could penetrate the entire specimen and still form images with sufficient contrast. With such a high imaging speed, for tomography of an entire brain with 10^3 projection images could potentially be imaged in a fraction of a second! Such speeds may be considered as the upper limit, which exceeds our current performances by several orders of magnitude.

What limits our performances? First, not all the photons from the X-ray source are available for imaging. In a typical synchrotron beamline including a monochromator, only one ten-thousandth of the emitted photons are used for imaging.

In fact, for imaging applications it is better to avoid any effort to enhance the properties of the emission, since this causes a great loss in intensity. This problem was solved by early tests demonstrating that X-ray microtomography is not negatively affected by the use of a broad spectrum of X-ray photon energies. As explained in Sec. I.1.c, the required longitudinal coherence in high-resolution X-ray imaging is provided by the "white" radiation from a bending-magnet source. Thus, 3–4 orders of magnitude more X-ray photons can be used than for conventional X-ray imaging and tomography with monochromatized synchrotron radiation or laboratory X-ray sources. This is a milestone that made synchrotron X-rays tomography a leading approach for human brain mapping.

Second, a large FOV and high-resolution limit each other in all imaging systems, often imposing unsatisfactory compromises. In our case, this problem is not caused by synchrotron X-rays — which actually alleviate the problem better than any other type of imaging. We are still, however, limited by the detection system. For example, to maintain the pixel size $(0.1\ \mu m)^2$ for a 0.3 μm image resolution, the FOV must be only 0.2×0.2 mm^2 (using a 2 K $\times$ 2 K image sensor). Thus, a brain of size $\sim 200 \times 200 \times 200$ mm^3, would require at least 10^9 tomographic data sets, which affects, of course, the total mapping time.

Third, the detection of X-ray photons is not very efficient. To achieve high resolution, we use a scintillator screen to convert X-rays to visible light, which is then captured by an imaging device. The conversion of X-rays to visible light has low efficiency. For high-resolution imaging using a thin scintillator, only $\sim$0.1% of the photons hitting the scintillator screen are captured by visible light magnification-imaging systems.

Fourth, the number of projection images required for a "lossless" tomographic reconstruction by the standard filtered back-projection approach, should be similar to the pixel number along the direction perpendicular to the specimen rotation axis. Therefore, even if a hypothetical imaging device with 2 M $\times$ 2 M pixel is used, will require some 2 M projections for each tomographic image — instead of the 1000 projections that we previously estimated.

The above analysis of the different limiting factors was exploited to decide the details of the SYNAPSE strategy, targeting the removal of the identified problems. The full power of X-ray imaging will be unleashed by the following measures, all designed to enhance imaging speed:

(1) exclusively use unmonochromatized X-rays;
(2) use imaging sensors with the largest pixels possible;
(3) improve the conversion efficiency of the scintillator and its coupling to the optical system;
(4) develop methods for tomographic reconstruction that use fewer projection images.

Such improvements were partially realized with extensive tests in the past two years. We used a set of custom-designed visible microscope objective lenses with large FOV and high NA. They were matched with a large-pixel-number sCMOS (scientific complementary metal-oxide semiconductor) detector. The results lead us to realistically project an overall gain in imaging speed sufficient for the SYNAPSE strategy.

Using unmonochromatized X-rays is not without its own problems: they can damage the visible light objective lenses used for high-resolution imaging. We analyzed the situation and found that high-energy X-ray photons cause most of the damage [236] while weakly contributing to the image contrast. We therefore added to the BIB facility a high-photon-energy cut-off mirror before the specimen.

The elimination of high-energy photons was also enhanced by placing filters before the mirror. These filters absorb more X-ray photons at specific energies. For example, a 100 μm Ag thin foil absorbs 2 orders of magnitude more X-ray photons with energies above 14 keV, the K absorption edge of Ag, than those below it.

With the mirror and the filters, the visible-light objectives remained intact even when using unmonochromatized X-rays from the Taiwan Photon Source running at a maximum electron beam current of 450 mA. The combination of each protection device reduces the X-ray photon flux by 5–10 times, while still allowing us to take a projection image in $\sim$1 ms. This constitutes a 10$\times$ gain in imaging speed with respect to the approach of using a multilayer mirror monochromator, and a 100$\times$ gain over a double-crystal monochromator.

The successful tests strongly relied on the new X-ray mirror technology reviewed in Section 1.2.2. The ultrasmooth mirrors, developed in association with the RIKEN/SPring-8 partner of SYNAPSE, guarantee high reflectivity with no defects

on the mirror surface that would cause image artifacts. Note that such artifacts cannot be removed by simple image normalization and could affect any tomography reconstruction. The above solution, implemented at the BIB beamline, strongly enhances imaging speed.

After several months of exposure, some X-ray damage was observed for the visible-light components in our setup. We are therefore testing a new measure that would all together eliminate the problem: a third level of protection transparent to visible light while blocking all X-rays. The materials to protect the lens must be carefully selected and not subject to X-ray damage such as observed with glass optical components.

The realization of lenses with large FOV and high NA is already a very difficult task. The incorporation of an X-ray attenuator further complicates this goal. We tested a number of materials and identified LuAG (Lutetium Aluminum Garnet) as the most promising, ensuring good lens protection through strong X-ray absorption and transparency to visible light and for good optical quality [236].

Note the additional absorber also improves spatial resolution. In fact, its high refractive index in the visible increases the NA and therefore the resolution. Considering the big potential improvements, 10x in speed and 50% in resolution, we are allocating substantial resources to this subproject.

Another important improvement in the imaging speed is the reduction of downtime by automating the sample exchange, loading and alignment, as well as the imaging. This will also reduce the manpower required for large-scale mapping while enhancing the practical speed of the experiments. In practice, we would like the downtime to be shorter than the new image taking times after the above-mentioned technical improvements.

The first version of a robotized system was successfully tested at BIB. Continuous image acquisition was achieved for more than one week with no human intervention. The downtime between tomographic measurements was reduced from $\sim$20 min to $<$1 min. Automation will be extended to all processes and implemented in all SYNAPSE imaging facilities.

Incorporating Information from other Synchrotron Imaging Techniques

We are planning to use several other imaging techniques to obtain detailed local information on the brain neural network. Most of them are based on synchrotron X-rays and use the same specimens and the same preparation procedures as nanotomography (nano-AXON), the X-ray fluorescence microprobe, and MAXWELL. The feasibility of combining this additional information with the 3D structural network maps was successfully tested.

For example, the high-resolution images (e.g., Fig. 18b) from nano-AXON could be merged with lower-resolution micro-AXON images (e.g., Fig. 18a) of the same specimen [236]. The procedure relied on aligning obviously similar features. Merging is straightforward if accurate "landmarks", either intrinsic or artificial, can be exploited. These initial tests were performed by visually identifying small features for 3D alignment. However, automatic alignment is now being developed with no human intervention [237].

Automatic feature identification was first developed to align the projection images taken by nano-tomography and compensate for any non-systematic rotation movement [238]. The procedure can now reliably work for stitching together tomographic images and for the merging of different 3D image data sets. However, this approach will become more problematic with the increasing complexity within each image set. Indeed, larger specimens or denser staining will diminish the ability to identify small features. Introducing high-contrast artificial landmarks, such as metal nanoparticles or nanopatterns, can be a solution. Some of these approaches were successfully tested within SYNAPSE.

Fig. 19 shows an example of the results of merging sets of 3D images taken from different brains. A high-resolution tomographically reconstructed image of a mouse neural network is merged with a lower-resolution image of the blood vessels. Without identifying internal features common to both images, the alignment used only the outline of the brain. Therefore, the alignment could not accurately correlate these two types of information, nevertheless it could be used to identify the overall neuron network structure with respect to the microvasculature in different brain regions.

5.2.2. Staining

For high-resolution X-ray imaging of neuronal systems, the low contrast must be compensated for staining with a high-contrast material. Small particles – typically metallic – can "decorate" relevant microstructures, for example, binding to specific protein with antibodies, or neurons by Golgi staining. Specifically, Golgi metal staining, originally developed by Camillo Golgi in 1873 [239], was the first method allowing the visualization of neurons with visible light microscopy. For one and a half centuries, this "random" staining enabled neurobiologists to reveal the complete structure of individual neurons in extremely dense brain specimens and led to numerous landmark discoveries in neuroscience. Our previous tests demonstrated that it is also an excellent choice for SYNAPSE X-ray imaging and connectome mapping but requires critical modifications and improvements.

Basically, we want to visualize as many neurons as possible for brain mapping: could we simply stain all of them? Unfortunately, the answer is negative. In mapping the brain we are interested in revealing its circuitry. Therefore, the objective of the staining is to separate the connections from each other. In animal brains, the volume is filled by neurons, other type of cells and their connections with a low percentage ($\sim$20%) [240] of the so-called extracellular matrix. Tomographic reconstruction cannot be performed if X-ray transmission is largely blocked because the entire specimen is filled with heavy-metal based stains.

Furthermore, if closely packed neuron cells were all made visible by staining, it would be impossible to derive the connectome from the tomographic data. High-resolution nanotomography could offer the resolution to separate nearby connections, but its image taking is very slow [62] and therefore incompatible to the general SYNAPSE strategy.

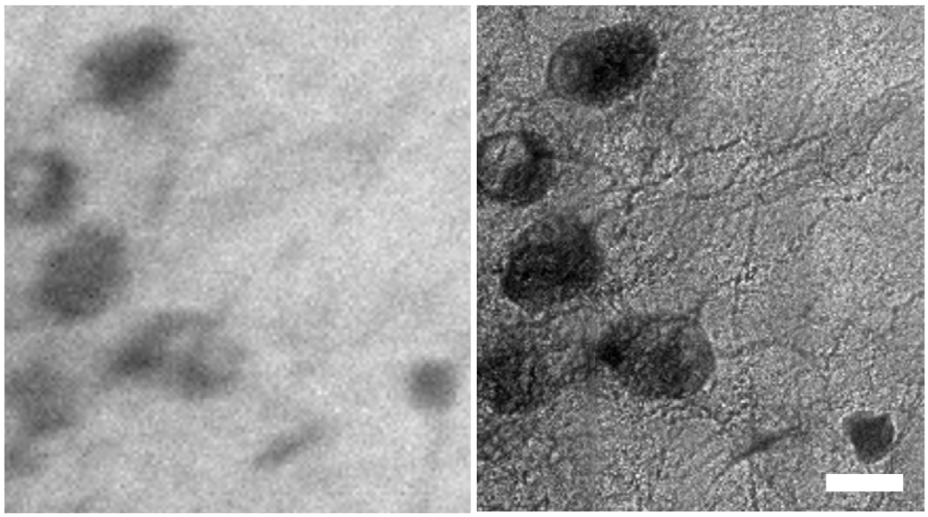

Fig. 18. Left: micro-AXON projection image of a mouse brain specimen with 0.3 μm resolution. right: nano-AXON image of the same specimen showing more details with ∼20 nm resolution. Scale bar: 5 μm.

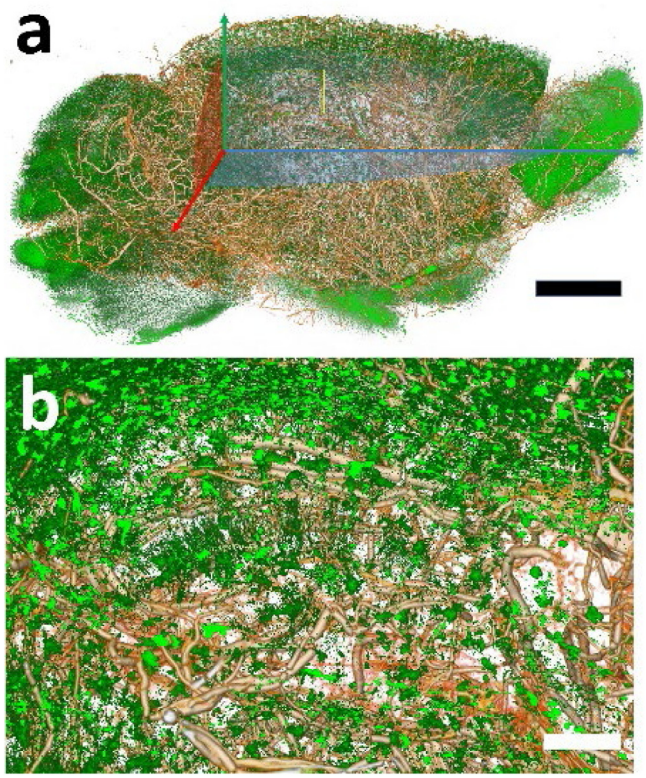

Fig. 19. AXON imaging reveals neural network structures of the mouse brain at different FOV's and resolution. (a) Micro-AXON shows a full-brain view of the blood vessels (golden) filled with barium sulfate particles and Golgi-stained neural networks (green). (b) A magnified view of the area marked in (a). Scale bars: 2 mm (a); 200 μm (b).

We therefore went back to the original approach by Golgi and Cajal [241], i.e., to sparsely stain neurons with heavy metals. We demonstrated that this approach works even better for X-rays, revealing with sub-micron resolution individual neurons deep in brain tissues [233].

Golgi staining, however, can impregnate only 1% to 5% of the total neurons in a random manner [242]. The low efficiency and unpredictability of Golgi staining creates consistency, reproducibility, and specificity challenges [243–245]. Nonetheless, there are still many avenues to explore and improve the art of staining as the science underlying this phenomenon remains partly elusive.

We can envisage from the works documenting how factors such as neuronal differentiation, membrane integrity, intracellular pH and metabolism affects Golgi staining [246] and to improve coverage. It was reported that the ratio of chromate to dichromate ions affects neuron staining [247,248]. It is also possible to promote silver reduction [249] using aldehydes and osmium tetroxides as post-fixation processes. These results motivate efforts to improve the method [245].

Note that the Golgi method stains a neuron either completely or not at all. The low fraction of stained neurons in mouse brains leads us to a plan based on sparse staining and on a statistical procedure (similar to the FlyCircuit method [250]), morphing and merging many different partial 3D images to cover all neurons and connections. For *Drosophila* brains, the 1%–5% Golgi staining rate required >100 brains to complete the connectome map. We are implementing the same strategy for mouse brains within SYNAPSE reaching significant improvements in the Golgi staining efficiency with the following approaches.

Tissue Clearing and Expansion

By using chemical reactions to expand the polymer skeleton the entire specimen can be uniformly expanded without altering local microstructures [251]. With tissue clearing procedures [252], this allows visible-light imaging beyond the diffraction limit. However, X-ray imaging already achieved much higher resolution in 3D. And a larger volume strongly increases the image-taking time, so tissue expansion is not interesting for SYNAPSE.

However, the tissue treatment procedures dissolve the cell membrane and replace the tissue with a polymer network: this improves the perfusion of labeling agents. The resulting tissue is much more "permeable" to labeling nanoparticles and Golgi staining precursors. As a result, more neurons are impregnated revealing more details with higher contrast in large specimens.

High pressure and Other Treatments

High-pressure immersion and ultrasound tissue treatment was found to considerably increase the efficiency of Golgi staining. The precipitations are also more connected within each neuron reducing artifacts due to segmentation as well as improving network tracing [253].

Better Understanding Golgi Staining

Is the mechanism really random, or are there factors determining which neurons are stained? We are tackling this fundamental issue with several approaches, specifically investigating:

(a) The neuronal differentiation state: Golgi staining produces different results in brain tissues, for example, of different maturity/age [254,255].
(b) Intracellular pH: by using an acidic chromatin solution of the Golgi–Kopsch method led to increased formation of soluble dichromate ions [243].
(c) Metabolic state and mitochondria activity: the neuron metabolic state may affect its Golgi impregnation [249,256].

Systematic studies of these factors are underway. These investigations will allow us to optimize the process parameters and enhance the percentage of visualized neurons.

In general terms, from our tests on *Drosophila* and mouse brains we estimate that the Golgi-staining coverage can be expanded by $>30\%$ before causing problems for the resolution of connected structures. This increase would of course reduce the number of brains required for complete connectome mapping.

5.2.3. Labeling with metal nanoparticles

Staining/labeling methods developed for other imaging techniques can be transferred to X-ray. None of them, however, has been successful for large tissue specimens. For 3D X-ray imaging, we must develop new labeling agents and methods.

We already identified a potential solution: a neuron-specific labeling technique for brain mapping combining enzyme signal amplification, enzyme metallography [257], and metal exchange in deep tissues. These procedures are also compatible with genetic expression and immunolabeling and work on reasonable large tissue specimens.

Using the similar approach of immunolabeling with metal nanoparticles, the key is to use as small particle as possible, while the tissue treatments, such as tissue expansion, could increase the permeation of the labeling agents into deep tissue. With functionalized Au nanoparticles (AuNPs) staining specific neurons in an entire *Drosophila* brain and were imaged by micro-AXON. A similar approach using scintillating nanoparticles (SciNPs) worked for MAXWELL [230]: Mouse brain staining using streptavidin-conjugated SciNPs (st-SciNPs) was demonstrated for $\sim 50\ \mu$m thick samples.

Another recent strategy modified peroxidases as genetically encoded X-ray-sensitive tags (GXET) for site-specific labeling of proteins-of-interest in mammalian cells [258]. Using this novel tag, protein locations associated with the alteration of a DNA-methylation pathway can be imaged by nano-AXON.

These preliminary tests all successfully stained the targeted cells and delineated the neuropil structures in large tissue specimens. The speed and resolution of these imaging results are far superior to visible light or electron microscopies and is fully compatible with other neuro-anatomical techniques and results [233].

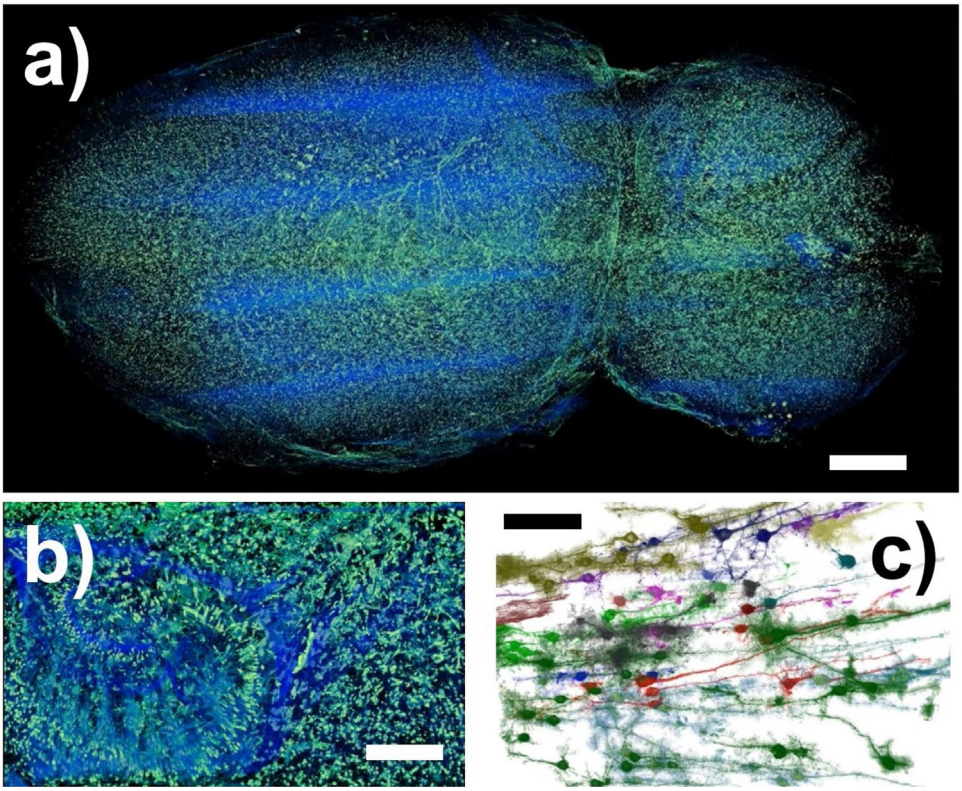

Fig. 20. Tomography reconstructed images of (a) a whole mouse brain, (b) hippocampus region, and (c) example of neurons segmented from the 3D data. Scale bars: (a) 1 mm, (b) 200 μm, and (c) 50 μm.

5.2.4. Specimen preparation

Other aspects of specimen preparation can be quite critical besides staining. Notably, the tomographic reconstruction often yields poor resolution or fails completely due to specimen instability — specifically, local distortions due to heating, dehydration or other phenomena. The standard filtered back projection (FBP) reconstruction does not tolerate any parts of the minimum reconstruction volume (voxel) to deviate from its ideal circular trajectory by more than its size.

Reconstruction thus imposes a stringent condition to specimen stability: radiation damage and other causes of distortion must be minimized. Iterative reconstruction algorithms correct minor s increase the reconstruction time. We extensively tested standard fixation methods and found that the approach of Wu et al. [62] meets our requirements.

5.2.5. Toward large animal brains

So far, the SYNAPSE-related tests were limited to *Drosophila* and mouse brains. More than 500 *Drosophila* brains, and three mouse brains were imaged with the micro-AXON tomographic imaging. Fig. 20 shows for example one complete mouse brain. With the improvement in the speed mentioned before, such an image would take only a few days to complete.

However, we must rapidly move to large animal and human specimens – including pigs and NHPs – for which staining is a key concern and little information exists. We must verify that large animal brains can be uniformly stained while extracting sufficient details using the optimized Golgi staining method. The successful tests on *Drosophila* and mice do not necessarily apply for large animals.

Fig. 21 shows AXON images from a large section of a pig brain. Fig. 21c is the high-resolution tomographic reconstructed image of the marked region in Figs. 21a and 21b. These images are of good quality, comparable to that for mouse brains. But we must be cautious since the freshness of the specimen is critical for best staining results. The post-mortem delay (PMD) must be minimized: in the case of Fig. 21, the specimen was prepared within 2 h after sacrifice.

The PMD is a critical issue in the move of SYNAPSE towards human brains. The corresponding specimens are usually obtained by donation, and their handling poses logistic and legal problems that can affect the PMD. Unfortunately, there are very few studies on how this impacts staining. We are certainly aware of this problem and will dedicate to its solution all the required attention.

Along this direction, we explored PMD effects on the morphology and structural changes of pyramidal neurons located in the mice cerebral cortex of mice. We used mouse tissues kept *in vitro* for different times to simulate the changes that

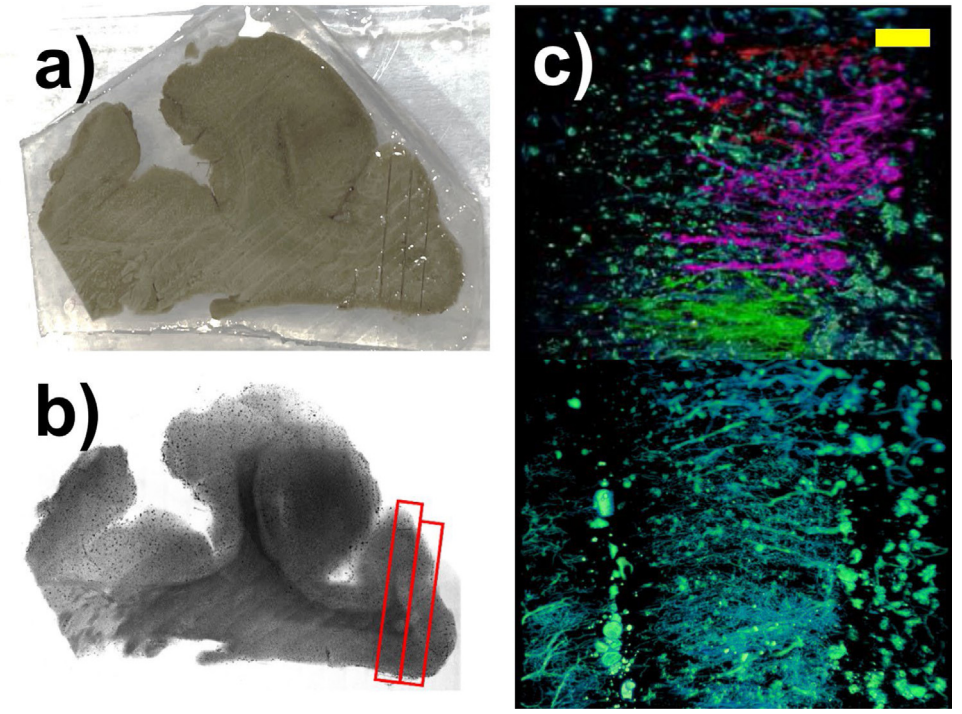

Fig. 21. Images of one slice of pig brain Golgi stained. (a) Photograph of the slice and (b) the X-ray image. (c) Stitched AXON tomography reconstructed images of areas marked by the red boxes. A few neurons are segmented and colored to show detailed structures. Scale bar: 100 μm.

might be expected with PMD of the human brain. We obtained visible microimages with Golgi and Nissl staining [259,260]. We also used synchrotron X-ray micro-tomography to perform analysis in 3D.

Our analysis [261] as a function of the PMD revealed that the completeness and complexity had decreasing trends. Statistical results on dendritic spines also exhibited a decrease [253]. The 3D X-ray images confirmed these findings.

Verification that our staining processes can be applied to human brains was obtained with the tests on *Macaca fascicularis* (*M. fascicularis*) brain described in Ref. [262]. Fig. 22(b) shows a stitched projection radiograph revealing fine details of the neuron system in the hippocampus region. The structure revealed by the tomography reconstructed images shows high quality staining, obtained with the same optimized Golgi staining method that was used in *Drosophila*, mouse and pig specimens shown above.

In essence, the tests demonstrated that our modified Golgi method uniformly stains very large specimens (>5 cm diameter) even very complex brain systems. The PMD was minimized to less than 1 h. Because of the brain size, Golgi staining time was extended to 1 month to guarantee good metal contrast.

Similar tests on degraded brains produced no recognizable neuron structures: there was no metallic aggregation inside the brain tissue and the X-ray images were blank. This is most likely due to the neuron cell death. We are planning experiments to investigate neuron cell death with respect to brain death.

5.3. Multimodality imaging and fusion of 3D image information

We already mentioned that, in addition to X-ray imaging results, we plan to integrate in the SYNAPSE Google-like map information from other 3D imaging techniques. These will notably include approaches using visible or infrared light and electrons.

To successfully integrate the information from complementary techniques, we must improve their performance — notably for large-volume analysis and speed. For example, Fig. 23 shows the first 3D imaging of mouse brains using infrared spectromicroscopy [263]. The penetration of infrared light is limited and the 3D imaging is achieved by continuous sectioning, e.g., ∼1000 slices. The targeted 3D resolution of 3-5 μm was achieved and the imaging speed was reached by fast scanning of the quantum cascade tunable laser.

The 3D infrared spectromicroscopy images were merged with the X-ray tomographs of the microvascular structure to identify the correlation with local biochemical changes with respect to the glioma tumor and the tumor-induced angiogenesis. Fig. 24 shows how an AXON image of the entire mouse brain can be used as a template for the merging process

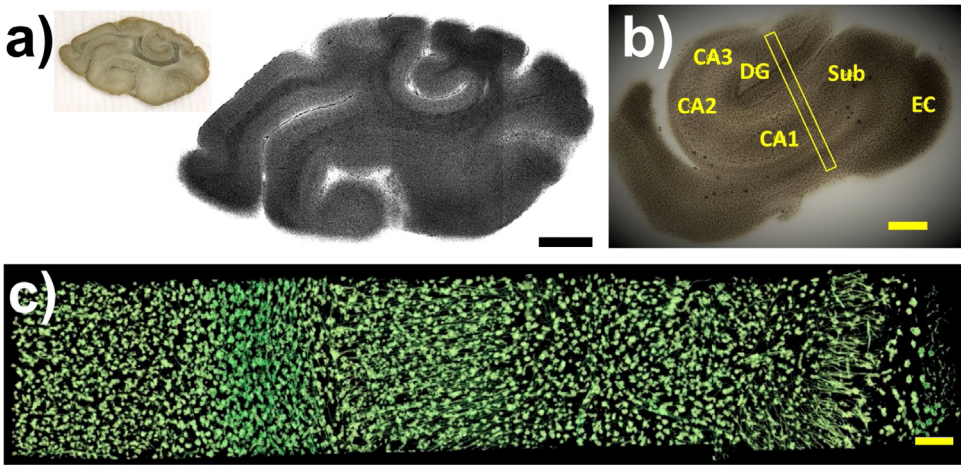

Fig. 22. Image of a slice of brain of Macaca Fascicularis (see Ref. [262]). (a) Patched X-ray images of one brain slice. Inset: photograph of the specimen. (b) Patched X-ray image of the hippocampus area. CA: Cornu Ammonis; Sub: Subiculum; EC: Entorhinal Cortex. (c) Tomography of one specimen rod from the hippocampus. Scale bars: 5 mm (a); 1 mm (b); 100 μm (c).

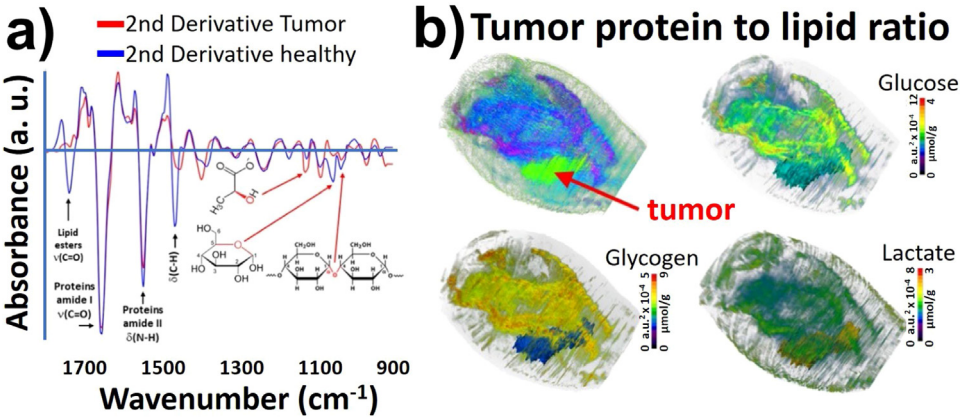

Fig. 23. 3D IR-imaging for quantitative metabolic analysis of the brain. From the second derivative of the 3D spectrum matrix (a), the glucose, glycogen and lactate IR absorptions are quantified and mapped for the whole brain (b). The tumor is identified and can be delimited using the protein-to-lipid ratio from absorbances of amide I (peak centered at 1654 cm^{-1}) and lipid esters (peak centered at 1735 cm^{-1}).

A similar approach will be applied to connectome mapping. In spite of the large difference in spatial resolution with respect to AXON, infrared imaging provides valuable biochemical information not yielded by other imaging methods. Thus, its integration is very desirable.

Similar image merging approaches can be applied to most other 3D imaging techniques that rely on specimen sectioning. We also specifically tested merging reconstructions with cryo-electron microscopy (cryo-EM) images and with stochastic optical reconstruction microscopy (STORM) images [264]. The co-registration is of limited accuracy because of the differences in resolution. However, these techniques already play a very important role in brain imaging. We are developing preparation methods for them and other approaches to allow accurate integration.

Accurate image merging is not a trivial task: we plan to use machine learning to facilitate it. The successful integration of information from different techniques in SYNAPSE connectome maps will of course have a strong impact.

5.4. The next phase: SYNAPSE 2.0

The above achievements pave the way for the next period of human brain connectome mapping. This specifically requires a 10–100 times speed-up in imaging acquisition at all AXON partner facilities and adequate computation tools. The detailed targeted performances are:

- AXON tomographic imaging of one human brain with 0.3 μm resolution within a few days of beamtime.
- On the same brain specimens, nano-AXON imaging with a speed of $(100\ \mu m)^3$/min and <20 nm resolution.

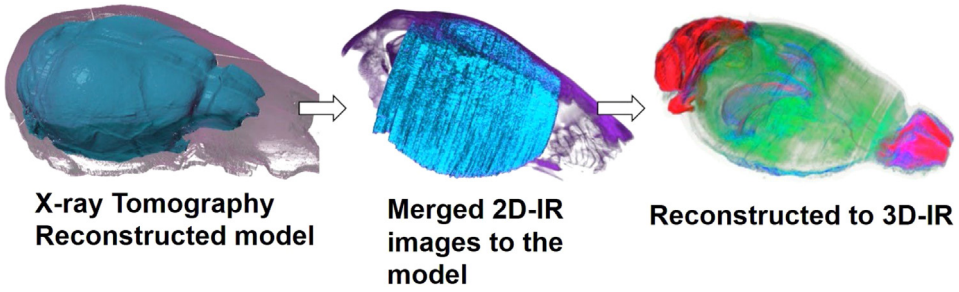

Fig. 24. From X-ray tomography image of a healthy mouse brain to the 3D reconstructed IR image of brain chemical contents. Left: X-ray tomography defining the dimensions of the brain; Center: alignment of 2D IR images of the mouse brain after extraction of the brain, cryosectioning (682 slices) and morphological corrections; Right: 3D-IR image reconstruction using the protein-to-lipid ratio from absorbances of amide I (peak 1654 cm^{-1}) and lipid esters (peak 1735 cm^{-1}).

- Development and construction of a set of "standard" brain models allowing deposition of brain data from all AXON instruments at different synchrotron facilities.
- Data structuring that allows the integration of information from other image techniques.

The scale of the next phase SYNAPSE 2.0 will most likely require an expanded alliance. For example, we estimate that 1 exabyte of data storage is required for the 3D data set of one human brain. And a complete human brain connectome map will require in the future 100 exabytes.

This is an unprecedented challenge, but even more problematic will be to move the mass of data through the Internet. We plan to establish distributed high-performance computation facilities at each partner site, responsible for all data processing. Only the end-product – the connectome map from a single brain – will be available for public access at a central server. This infrastructure will require a broad international collaboration involving the public and private sectors.

In parallel, the donation of human brain specimens must be managed by the SYNAPSE members in collaboration with their local neurobiology and medical institutions, within a coordination plan tailored for their specific objectives. This strategy must reduce the problems of transferring human specimens across borders.

After the next phase, we expect SYNAPSE to further evolve with a strongly expanded international collaboration. Development will continue for an indefinite time. Indeed, we envision SYNAPSE 2.0 to evolve into an institution like CERN, facilitating the parallel contributions to structural neurobiology of many countries.

6. Computational issues

6.1. The Spring Board: Computational Procedures for the Drosophila Connectome

Computation is a major pillar of the SYNAPSE project. Four national HPC facilities currently participate in the coalition, guaranteeing sufficient support for the needs of unprecedented magnitude. The starting point is the accumulated experience in processing the AXON data for *Drosophila* brains. The same procedures are applied to the ongoing analysis of the mouse brain connectome.

6.1.1. Tomographic reconstruction — from 2D images to a 3D model

Reconstruction first converts a series of 2D images into quantitative values of the absorption coefficient for each specimen voxel, which are then used to produce 3D maps by tomographic reconstruction [265]. With the most effective FBP (filtered back projection) method [266], a typical reconstruction of one set of standard AXON tomographic data can be completed within a few minutes on a standard (XEON CPU, 256 GB RAM, nVIDEA RTX 20 series GPU) workstation.

There is certainly room for improving the reconstruction performance and accelerate connectome mapping. In fact, several new methods have been proposed to exploit increasing computer power. A common strategy is to obtain an accurate 3D structure by iteratively correcting at each step the results of the previous step with fits of 2D images. This approach, when it converges, can reduce the number of required 2D images and/or their angular range [267].

Artificial Intelligence (AI) or machine learning is likely to play a key role in the reconstruction process [268]. We specifically envision using the a priori knowledge of individual neuron shapes and of the connection distribution and characteristics to develop more effective reconstruction algorithms. This could notably accelerate the convergence of iterative reconstruction and achieve the best compromise between the final image quality and the overall speed.

6.1.2. Transforming the raw images into structural data

A successful tomographic reconstruction should preserve all the details of network structures down to the desired 3D resolution, producing an accurate "bitmap", voxel by-voxel, of volumetric data. The "bitmap" information is then converted to a vector representation of the network. In connectome mapping, the critical information for each voxel is

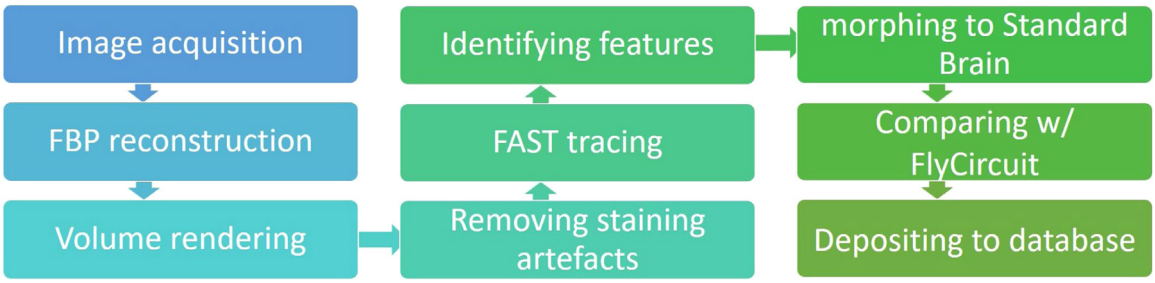

Fig. 25. The computation reconstruction procedure for constructing a database from X-ray micro-radiographic images of *Drosophila* brain.

if it belongs or not to the neural network. Therefore, the conversion can be limited to "black-and-white" maps thereby decanting only the essential information and limiting information overflow.

Data conversion is achieved using the "segmentation" process — which separates the stained voxels from unstained ones. If the gray scale value, corresponding to the local X-ray absorption coefficient, is higher than a well-defined threshold corresponding to the unstained tissue absorption, indicates that the voxel includes absorbing components other than the tissue. One can thus conclude that it is affected by the heavy-metal Golgi stain and must, therefore, be part of the neural network. The final steps must connect all the voxels that are related to all stained neurons and provide a picture of the complete network structure, suitable for tracing through connected voxels to extract a wire diagram.

This procedure is not trivial. Noise interferes with it, in particular when the signal is weak: one needs special algorithms [269,270] to handle the limited contrast of very fine structures. This problem can be partially solved by using Golgi staining and acquiring images with high contrast, marginally sacrificing imaging speed. The uneven background, caused in the tomographically reconstructed images by the irregular and fluctuating background in the projection radiographs, makes it difficult to use a universal threshold for the segmentation. Our solution, the FAST (Fast Automated Structure Tracing) and NeuroRetriever algorithms, developed for segmentation using local contrast [271], has been optimized and is now rapid enough to be part of the SYNAPSE image processing procedure.

The segmentation and neuron tracing steps produce a vector representation of the network that does not occupy too much memory space — and can be easily used for further structural analysis without accessing the original projection images. Fig. 25 outlines the standard procedures for the image processing described above.

6.1.3. Obtaining a complete connectome from different brains with structural variations

Before describing the pipeline highlighted in Fig. 25, we must address one fundamental question concerning the exact nature of the "map". If one could image all neurons and their finest connections, imaging one brain would be sufficient. However, this would require very high 3D resolution, $\approx$10 nm, and constructing a map from the images would take a prohibitively long time (millions of years). Instead, the SYNAPSE strategy is to compromise on resolution and focus on the major stationary structures that can be extracted with 0.3 μm resolution and sparse Golgi staining. Therefore, we must build a model brain that contains many partial connectomes and describe the most probable wiring.

Furthermore, brains are inherently plastic. In *Drosophila*, an adult brain is subdivided into $\sim$50 small regions, called "local processing units" [250]. Most of which are separated from each other with distinct boundaries as a result of clustered neurites, from intrinsic local interneurons mixed with axons/dendrites to extrinsic input/output neurons. At the mesoscopic level, information from each sensory function is relayed via stereotyped projection neurons, and processed by specific sets of local processing units [272]. Thus, regardless of local synaptic plasticity, a neuron in a well-developed brain does not significantly change its pre- and postsynaptic partners.

Therefore, our high-speed microscale X-ray mapping gives us the opportunity to describe neuron-to-neuron connectivity on the scale of the entire brain, using a statistical approach. With a large number of data sets, e.g., $>$500 adult male and female *Drosophila* brains, we first extracted the 3D structures of all labeled neurons (1%–5% of total population) for each individual brain. Then, we merged these partial representations by a non-linear spatial transformation into a model brain with an average size and shape. By oversampling more than five times the normal neuron population, we obtain a model brain that contains most (if not all) neuron types and connections between local processing units.

Note that this process does not assume that the structure and the connections of neurons in each brain are identical after morphing. The assumption is instead that when a sufficient number of specimens is processed, each neuron-to-neuron connection can be characterized by a "likelihood index". One can then focus on small regions of interest to validate the index value with nanoscale X-ray tomography or serial-section electron microscopy [273] with synapse-resolution.

Thus, the derived connectome map will include all possible variations between different *Drosophila* brains and the corresponding wiring can be a guide in additional functional studies. The problem of variability between individual connectomes increases for large mice and human brains. However, oversampling (number of analyzed brains) is set by the percentage of stained neurons, which is basically the same as for *Drosophila*. Thus, the approach should also work for mouse and human brains.

6.2. Challenges for large brains

The size of the neurons and of their connections are not really larger for large brains than for *Drosophila*. Therefore, resolution requirements cannot be relaxed. The time to obtain 3D images therefore increases, which scales with the third power of brain size. Before the establishment of SYNAPSE, this was the major barrier for large-brain mapping.

SYNAPSE provides a solution by allowing the acquisition of the required large volume of image data. But it also requires a clear, articulated, and flexible strategy to process the data and arrive at quantitative information.

We estimated the amount of 3D data for one human brain assuming a voxel volume of $\sim(0.1\ \mu\mathrm{m})^3$, and a brain volume of $\sim 1.2 \times 10^6$ mm^3. The result exceeds 10^{18} byte (1 exabyte) of 3D data, assuming that only one byte is used to describe each voxel. For reference, this is comparable to the entire volume of data generated in the world in one day. And is obviously beyond the capability of any current high-performance computing system.

The sheer amount of data did already create problems in data processing for *Drosophila*. The entire strategy for large brains needs to be reconsidered: we summarize here what we already achieved, outlining a strategy validated by positive tests.

6.3. Computing strategy for SYNAPSE

6.3.1. Image alignment

At the image acquisition stage, the most problematic issue is to guarantee that the projection images allow tomographic reconstruction without distortion. The problem is mechanical inaccuracy when the image resolution is high. For example, when the pixel size is $\approx$10 nm, even a slight mechanical vibration can jeopardize accurate reconstructions. Mechanical instability while rotating the object can cause a 5–30 pixel position inaccuracy even with a very accurate holder.

Holder position can be accurately determined during image acquisition, but this would take a long time, causing an excessive X-ray dose on the object. Therefore, manual adjustments are generally required.

We can solve this problem with a feature-based alignment (FA) [238] to correct the displacements caused by mechanical problems. FA directly aligns the images in the vertical direction. However, the horizontal direction is more problematic.

Indeed, the horizontal calibration is based on the projected feature points that form a sine-shaped locus, i.e., a "sinogram", in the x-θ coordinate system — where x and θ are the horizontal location and the projection angle. This calibration involves three steps: detecting projected feature points, matching projected feature points to construct a set of loci, and fitting the loci to sine curves to adjust the horizontal image displacements. The details of the process follow below.

Detecting Projected Feature Points

This problem is handled using the "local extrema" approach, which are selected using the scale-invariant feature transform (SIFT) algorithm from the Differences of Gaussian (DoG) pyramid in the projection image. The details can be found in Refs. [274–276].

Matching Projected Feature Points

Since the object rotation angle is small, the projected feature points are close to each other and have similar information in two consecutive images. However, the distance between the two matched projected feature points depends on the distance between the feature and the object rotation axis. This means that an affine transform cannot match the projected feature points in the two images. Therefore, FA uses a "greedy algorithm" [277] for classifying the projected feature points. For each pair of images, the random sample consensus (RANSAC) method [278] is first applied, and a tracking method then matches the projected feature points in the next image [279].

Horizontal Displacement Estimation

In the next step, FA approximates the loci of the matched feature points in the x-θ coordinate system by using a least-square curve fitting. The deviation between the loci and the sine waves provides information for horizontal calibration.

Fig. 26(a) shows an example: a projection image of a HeLa cell. Six reliable feature points were selected from the identified projected feature points. Fig. 27(a) shows the loci of the selected points in the x-θ coordinate system. Fig. 27(b) shows the sine waves that most effectively fit the loci. The projection images are aligned according to the fitted sine waves, and Fig. 27(c) shows the loci of the projected feature points after alignment. Fig. 26(b) shows a tomographic image reconstructed from the aligned projection images. Texture-based volume rendering was used to produce a 3D image of the volume data. Fig. 26(c) shows the volume-rendering result.

Rotation Axis Bias Correction

The bias of the rotational axis is one of the relevant problems in tomography [280,281]. Several computer-based solutions are possible [282–284]. The method based on gradient descent can efficiently suppress artifacts and errors in the projection angle [238]. Fig. 28(a) shows a reconstructed image without error corrections. Fig. 28(b) presents the enlarged view of the region. Fig. 28(c) shows the image obtained using the gradient descent-based method. Fig. 28(d) shows the enlarged view of Fig. 28(c) .

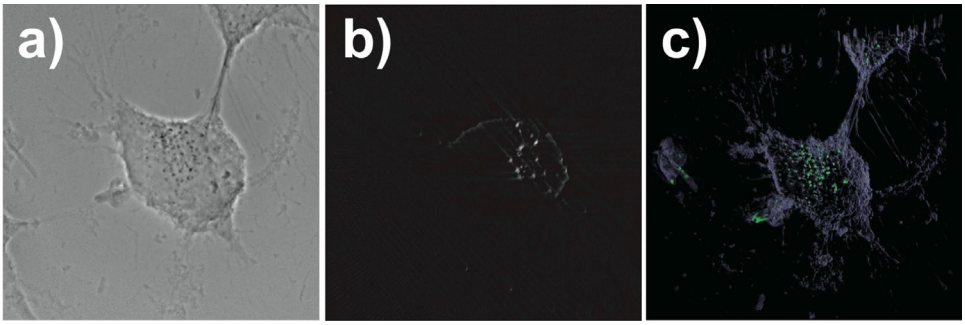

Fig. 26. Misalignment correction. (a) X-ray image of HeLa cell. (b) CT result. (c) Volume rendering result.

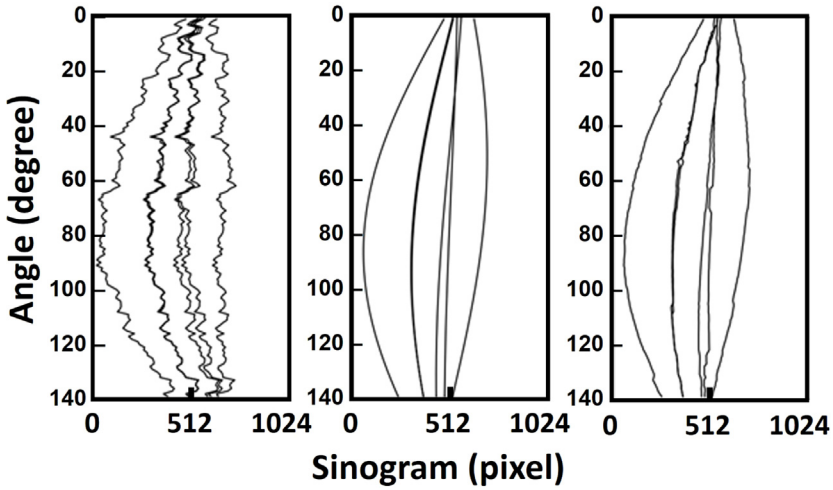

Fig. 27. The loci of the reliable projected feature points of HeLa. (a) Six reliable feature loci found in the acquired images of HeLa. (b) Most suitable sine waves of HeLa. (c) Aligned loci.

6.3.2. Tomography reconstruction: Filtered back projection (FBP) and beyond

We already saw that deriving a neural network from X-ray images covering the entire brain is a formidable challenge in terms of computational speed and throughput. Fast image taking is essential, but high processing speed is also required.

The algorithms for image processing must be very accurate to avoid artifacts or information waste. Unfortunately, speed and accuracy are often in conflict with each other. The SYNAPSE strategy deals with speed first using algorithms of limited accuracy, with the option of later improving the accuracy if refinements are needed. We present here some details of this approach.

FBP Reconstruction

As discussed in [234,236], standard FBP is the first reconstruction step. After reconstruction, voxels intensity (corresponding to an X-ray absorption cross-section) is inspected to verify that it is higher than for unstained tissues.

The FBP-reconstructed data can be used as the "ground truth" for machine learning, to develop tomography algorithms using fewer projections (sparse-view tomography), to remove artifacts (such as ring artifacts or motion blur due to specimen motion), and for segmentation and tracing.

Sparse-view Reconstruction

High-resolution FBP tomography requires long image acquisition times and can result in sample damage. A low-dose alternative is sparse-view computer tomography [285] (SVCT) that uses X-ray projections only in a few directions.

The problems of SVCT can be approximately solved by compressed sensing [286–288], a method which can reconstruct a sine wave from a few inputs. Another SVCT method [289] process tomographic images with a set of equally sloped projections on a pseudo-polar grid, by applying fast Fourier transforms to reconstruct the image.

One of our first efforts is based on the convolutional neural network (CNN), a deep learning algorithm, which was successfully demonstrated for low-dose CT [288,290,291]. In addition, we used the generative adversarial network

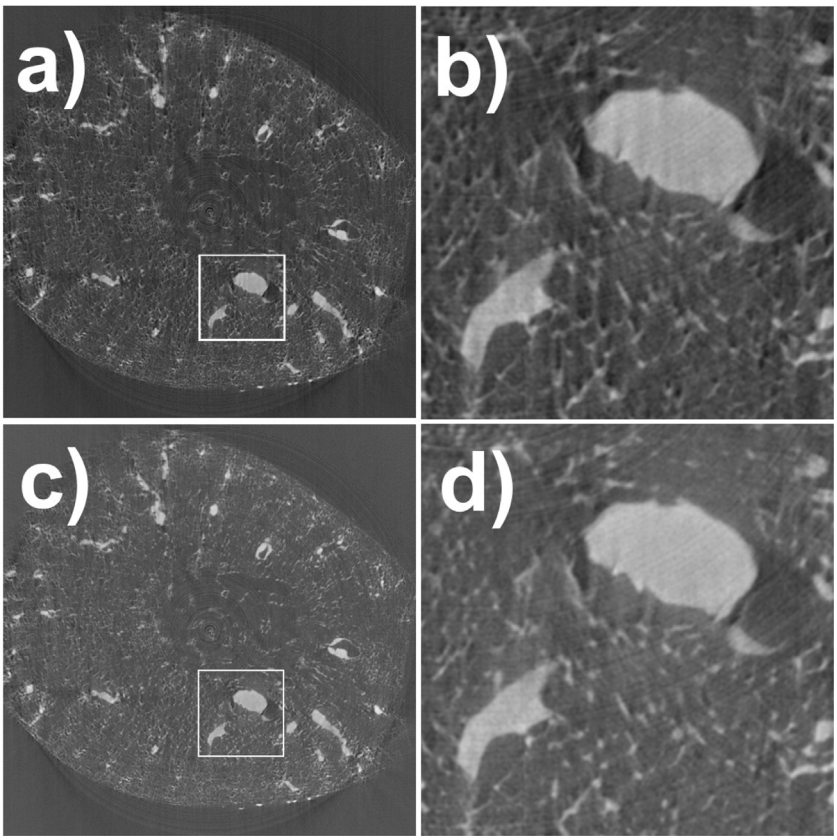

Fig. 28. Tomographic reconstructed images of a mouse kidney. (a) Reconstructed without any correction. (b) Region marked by the box in (a). (c) and (d) Reconstruction with error correction.

(GAN) [292–295] method to generate missing images in the sinogram and achieved the tomographic reconstruction using a much smaller number of projections.

Fig. 29 presents the test result using the GAN algorithm on a reduced (256 of 256 × 256 pixel projection image) image set. After a training that spanned 200 epochs, 200 additional sinograms of *Drosophila* brain were used for testing. Fig. 29(a) shows a test sinogram and 29 (e) is its FPB reconstructed image. Fig. 29(b) shows 13 (the white horizontal lines) of the 256 projections that were used to test the trained GAN. By linear interpolation Fig. 29(c) and GAN Fig. 29(d) , sinograms are generated from the 13 projections and produce a tomography reconstructed slice: Fig. 29(f) from Fig. 29(c) and (g) from Fig. 29(d). Clearly, GAN results in a superior performance than linear interpolation and achieved a quality close to that of the original FBP reconstruction with 600 projections.

6.3.3. Image stitching

The limited field-of-view of the projection images, determined by the combination of the magnification and of the sensor size, makes it necessary to acquire tomographic images only on small portions of the brain and to stitch them together. The key issue here is to minimize the overlap of the stitched images thereby limiting the acquisition speed, while allowing accurate feature recognition within the overlapping regions to obtain accurate alignment.

At present, the overlap ranges from 15%–20%. Each block was moved to maximize the similarity of the features in the overlapped regions. The multi-band image blending method [296] was used for this task.

Fig. 30 shows an example of the results of this alignment procedure [297]. Specifically, Fig. 30(a) shows 3 × 3 projection images of a mouse kidney without processing. Fig. 30(b) shows instead the alignment results after maximizing the similarities. Fig. 30(c) shows the reconstructed volume.

Note that to optimize the image contrast and the quality of the reconstruction, to minimize radiation damage and to distribute specimens to different facilities our preparation includes dissecting future brains samples into rod-shaped sections, whose cross section is 2–3 times the field of view. This requires stitching algorithms more sophisticated than those outlined above to handle the regions with no overlap because of the dissection-induced loss of tissue. For that, we use projection images acquired before the dissection and machine learning.

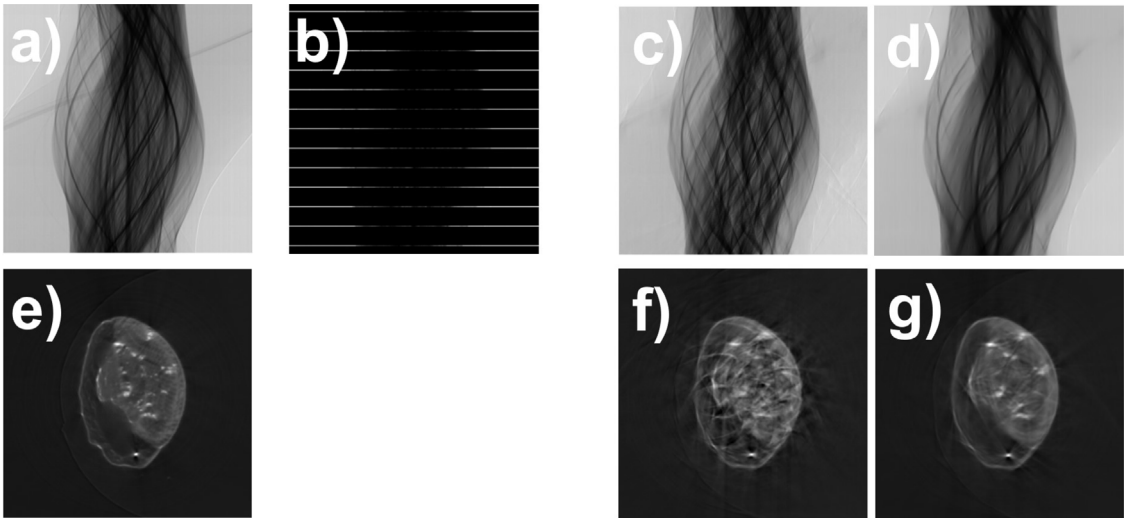

Fig. 29. Sparse-view tomography. (a) The sinogram of a slice with 256 projections (views). (b) Resampled sinogram with 13 views at angles marked by the white horizontal lines. (c) Sinogram recovered via linear interpolation of the 13 views. (d) Sinogram recovered via GAN. (e) (f) (g) Tomography reconstructed slice images from (a) (c) (d).

6.3.4. Neuron network tracing

Segmentation and Tracing

The FAST algorithm [271], originally developed for neuron imaging by confocal microscopy, was used with limited modification for X-ray brain results. The tests were quite satisfactory, so it was adopted.

The FAST algorithm is able to convert in one step the 3D tomographically reconstructed images to wire frame data. The idea of FAST is to trace using as the starting point one specific voxel, stained and therefore part of a neuron, and search neighboring voxels for connections. A voxel identified as "stained" because its gray scale is above a given threshold is assigned a value of the "source field" index. At each step away from the starting point, the index is increased by one, so its value corresponds to the distance.

In addition to the distance from the starting point, tracing must also identify branching. This is done by defining the "codelet", i.e., the range of the source field values of the voxels connected to the one under consideration. By following the propagation of the codelets in this way, FAST identifies the branching points, endpoints and central points of each branch, i.e., all the information required to describe the network structure. Details of FAST and its use can be found in [271].

This approach is quite successful in terms of segmentation and tracing accuracy as well as computation efficiency. It was integrated into the overall image processing package for SYNAPSE following FBP reconstruction. An organized structured database is thus produced, i.e. the wire diagram maps, from which specific information can be extracted without dealing with the entire volume of image data.

This strategy was evaluated by assessing the effects of the segmentation threshold on the tracing results. Fig. 31 shows such results for a *Drosophila* brain image segmented with different intensity thresholds from 19,000 to 24,000 (over the grayscale of 64,000). The total number of branches are 14,185,622, 9,027,943, 3,097,989 and 1,657,377 for the increasing gray scale thresholds 19,000, 21,000, 23,000 and 24,000; thus, it decreases as expected. Fig. 32 shows the distributions of lengths and average areas for branches from 226 *Drosophila* brain images, using different grayscale thresholds.

We see that the statistical features and the total branch number changes with the threshold. However, the general distribution is quite similar. In particular, the log–log plots of the distributions of average areas in Fig. 32(d) have similar slopes for different thresholds (except for very small areas).

Statistical Analysis: Our Drosophila Images vs FlyCircuit

The above results of the FAST algorithm were compared to those of the Flycircuit V1.2 database [298] — with data for $>$20,000 neurons obtained using confocal microscopy. We focused on the differences between the length distributions and the average branch areas. For FlyCircuit, 17,287 neurons were segmented with the NeuroRetriever algorithm [271]. All segmented images were traced by FAST to obtain distributions. The log–log plots of the distribution of average areas as function of the segment length are shown in Fig. 33.

For our X-ray images, 252 whole brains were segmented as described above. The log–log distribution of the average areas extracted by FAST is consistent with a straight line (in red Fig. 33(a)), i.e., the distribution is proportional to (Average Area)$^{-\alpha}$ with $\alpha = 2.6$. The corresponding distribution for FlyCircuit data is also a straight line, but with a slight bend and may be shown more easily by shifting the FlyCircuit curve by -0.71. Thus, our data indicate a higher percentage of branches with small areas than Flycircuit. This difference implies that the area analyzed by visible microscopy is about

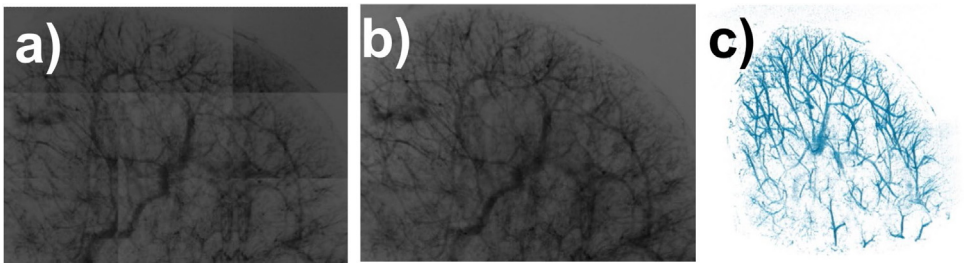

Fig. 30. Reconstruction test for a mouse kidney. (a) Stitching of 3 × 3 projection images without alignment. (b) The result of stitching for the same image (a) after alignment. (c) The result of stitching for the entire reconstructed volume.

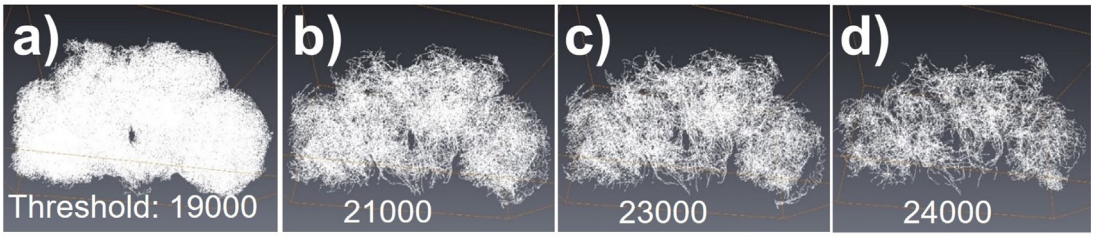

Fig. 31. Tracing results for one of our *Drosophila* images segmented with different grayscale thresholds.

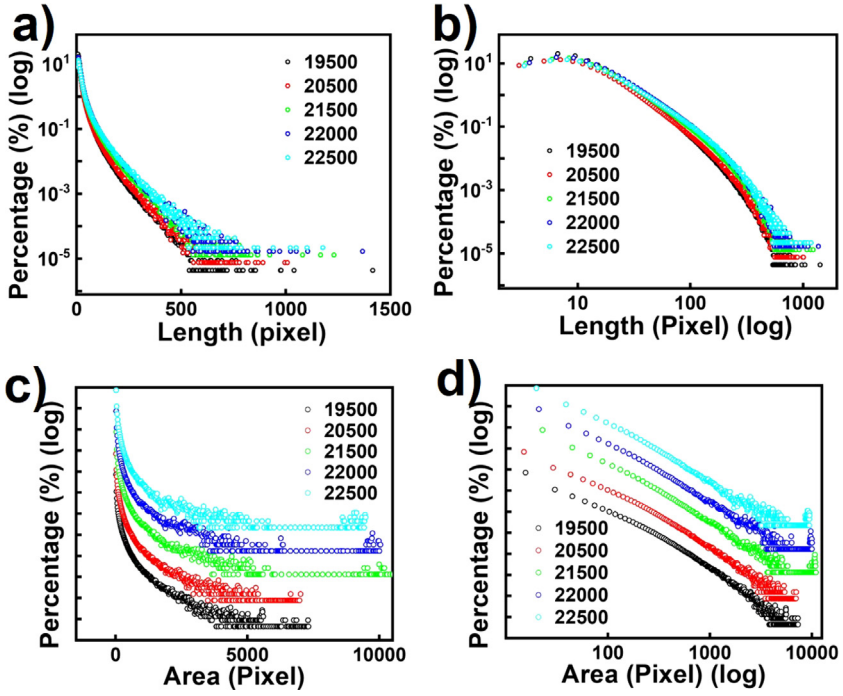

Fig. 32. The distributions of branch lengths, (a) and (b), and branch cross-sectional area, (c) and (d), extracted from our X-ray images with different intensity thresholds (shown in legends). The data are plotted in semi-log ((a) and (c)), and log–log ((b) and (d)) scales. The data of (c) and (d) are shifted vertically for stacking.

5 times larger than for X-ray imaging. This is consistent with the different 3D resolutions of visible (1 μm) and X-ray microscopy (0.5 μm).

Analogous similarities and differences are also visible for the log–log plot of the average area vs. the branch length. Fig. 33(b) shows again that after shifting downward by 0.71 the plot for FlyCircuit, matches our X-ray data well. The exception is the small region identified by a green circle.

6.3.5. Automatic soma detection

The FAST algorithm does not classify the different components of the network, such as the somas, the axons, or the synapse connections. However, brain mapping cannot be limited to wires, and therefore, we must go beyond the FAST processing discussed above to identify other structural features.

For this task, we developed a machine learning process called "Computer Vision Assisted Feature Enhancer" (CAFE). This approach automatically identifies specific signature features based on their morphology and can specifically discern different types of brain cells and blood micro-vessels. Moreover, CAFE supports parallel computing and can be used on major cloud platforms, such as Hadoop, Amazon Web Service (AWS) and Google Cloud Platform (GCP), to improve scalability.

CAFE is still under development. In general, it is not easy to identify specific neuron features from large and complicated 3D images based on limited information. Neurobiologists are still unable to provide the required information for the "training" of machine learning models. As a result, it is challenging to directly use existing deep learning models (e.g., CNN series [298–304] or YOLO series [305–308]) for this task.

Consequently, the application of this strategy to the specific case of automated soma detection takes many steps, with refinements by iterative feedback from experts. Even with these problems, our tests already demonstrated the power of the process. Details of CAFE are described in the Appendix.

The information extracted by CAFE processing, such as the locations of neuron somas to be used as starting points for the tracing, can also accelerate the FAST strategy. Furthermore, the identification of specific features can assist other imaging processing tasks described above, i.e., image alignment, stitching, iterative reconstruction and sparse tomography, by reducing training time and thus accelerating processing tasks.

CAFE was first tested for the identification of somas in the *Drosophila* brain. The results reach excellent accuracy in terms of precision and recall, 74%–85%. These results are quite encouraging in view of image processing for large animal brains. In fact, the soma shape makes the *Drosophila* results harder to process even manually. In essence, the CAFE strategy appears scalable from *Drosophila* to large animals without major problems.

6.3.6. Morphing 3D data to a standard brain

The strategy to create the SYNAPSE connectome database is adapted from the well-established FlyCircuit approach. However, we require a new "model brain" to morph the AXON results for *Drosophila*. The "standard brain" for FlyCircuit is built by averaging results of 34 whole brains without skulls. It is different from our AXON results due to the distortions after removal from the skull. In our case, the brains are left in the skull and the results better reflect the natural shape. This is of course a marked advantage of using X-rays.

Our standard brain was obtained by selecting a brain most similar to the average brain from 226 specimens with a procedure like FlyCircuit [250]. The tomography of a whole *Drosophila* brain reconstructed from AXON results provides the locations of thousands of neurons. Their geometrical description after tracing is processed with an affine transformation that preserves collinearity and distance ratios to best fit the standard brain.

AXON Brain Image Registration

We developed a two-step warping procedure to fit the data into the standard brain. The first step was the affine registration mentioned above, which was followed by non-rigid warping with the CMTK (Computational Morphometry ToolKits) [309] software. The corresponding 3D transformation matrix was used to deposit each neuron into the standard model. Thus, a neuron has a normalized position in a 3D coordinate system with respect to the standard brain. The entire process took 72 h using 64 cores of our computer system.

Identifying Anatomical Landmarks and Similar Neurons

Since the Golgi method only stains a few neurons, individual neurons cannot be used as references for morphing. Fortunately, we found good reference features: the neuron bundles involving parallel segments of several cells visible in every stained brain. This was the corresponding procedure: after preliminary warping with CMTK, we used the segments to identify the bundle structures. The procedure was verified for olfactory projection neurons from the antennal lobe to the mushroom body and the lateral horn — finding that the corresponding bundle is an accurate and reliable landmark for further image morphing.

Identifying Single Neurons or Neuron Bundles with Individual Neuronal Data in FlyCircuit

The next processing step reached the level of single neurons or neuron bundles. We searched suitable neuron candidates for this stage from the FlyCircuit database. Then, the X-ray data were morphed into the FlyCircuit standard brain. The NBLAST algorithm [310] was then used to identify similarities at the level of individual neurons. Fig. 34 shows an example of the results.

6.3.7. Compression and storage

These are two of the biggest problems of the SYNAPSE data handling, as the data for just one human brain could exceed 1 exabyte, requiring 50,000 20TB hard-drive memories. Data compression is certainly required. However, image data must not be compressed before completing processing to obtain the wire diagram. Afterwards, the raw data can be stored with techniques not providing high speed input and output, for example in magnetic tapes.

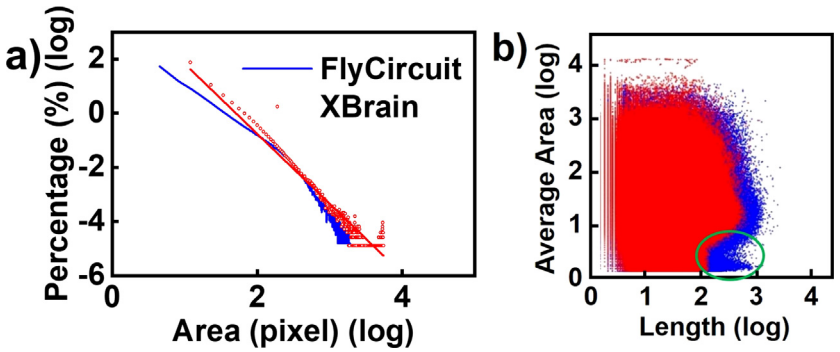

Fig. 33. Log–log plots of distributions of (a) cross-sectional areas of branches and (b) of average areas vs. branch lengths. The data are from 17,287 neurons from FlyCircuit (blue), and 252 of our X-ray images segmented with an intensity threshold of 21,500 (red). The data for FlyCircuit neurons are shifted toward the left by a constant −0.71 for comparison. A red straight line with slope −2.6 is shown in (a). (b) The data circled in green of the FlyCircuit are missing from our x-images, possibly because of limited resolution. The total branch numbers are 6,312,464 (FlyCircuit) and 7,642,936 (XBrain).

Note, however, that the data for projection images are only ∼20%–30% (number of projection images/number of pixels) of the reconstructed data. In a sense, the projection images constitute, themselves, compressed data. Therefore, we plan to save only the projection images and the tracing results, plus the processing parameters so that reconstruction can be repeated as required.

Note that the RIKEN Center for Computational Science (R-CCS) developed a high-efficiency compression system collaborating with SPring-8/SACLA [311] and is now developing its application for tomography that could further reduce the total data size.

After the FAST tracing, the wire diagram data is typically 1% of the FBP reconstructed data: again, a very significant data compression, with all the critical information saved. For example, the wire diagram produced by FAST from a 25 GB tomography reconstructed data set is ≈200–300 MB. The overall compression process reduced the data of 200 mouse brains to ≈1TB, compatible with all HPC facilities in the SYNAPSE consortium for subsequent analysis.

6.3.8. Visualization

The 3D reconstructed images are currently visualized using the Amira software. However, this is difficult when the tomography set exceeds ∼25 GB — a limit primarily set by the performance of the graphic display. Solutions to visualize larger data sets such as the whole brain of large animals are not yet clear. The power of graphic displays is not expected to increase by orders of magnitude as required to view many reconstructed brain tomographies stitched together.

Note, however, that visualization is not required for deriving the whole network, since the process is automatic. Nevertheless, some degree of visualization is still desirable to check the process and analyze the wire diagram. Therefore, we conceived a strategy similar to that of Google Maps. Basically, the image resolution scales with the size of the visualized region. In our case, the resolution change is not performed in real time, but using stored reconstructions with reduced resolution levels.

6.3.9. Image merging

Images obtained with other imaging techniques will be morphed with specific approaches that will require identifying structural features and markers. Linking markers in images of different kinds is not trivial, however. This will be an important development area of SYNAPSE, involving experts of different imaging techniques

6.4. Outlook

The processing strategy of SYNAPSE demonstrated for *Drosophila* brains and in part for mouse brains was not yet tested for human brains. However, considering the combined resources of the HPC facilities participating in the SYNAPSE consortium, we can make reasonable evaluations of the performances. This allows us to reach positive conclusions: the tasks for human brain mapping are not beyond our capabilities.

6.4.1. Data types: Definition, memory and storage design

The goal of the automatic processing of connectome mapping must deal with several data types, requiring different memory solutions for computing and storage. The frequency of access is also very different. Therefore, it is necessary to assign to each data type a specific data structure.

In general terms, the "vectorial" data obtained with the FAST processing are easier to handle than the "raster" data of the projection images or of the results of FBP reconstruction. In fact, their size is smaller and their processing easier

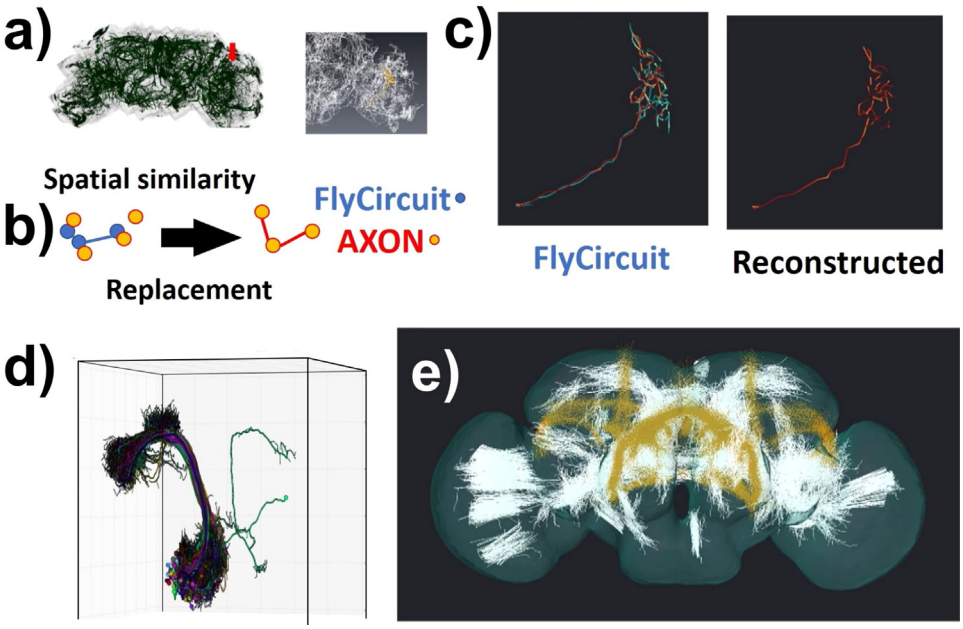

Fig. 34. (a), (b) and (c): Identification of brain structural features such as bundles, in the AXON *Drosophila* images. We applied the spatial similarity algorithm to identify neurons with similar morphology. (c) We applied an iterative closest-points algorithm to linearly align our X-ray data with the X-ray standard brain and the FlyCircuit standard brain. (d) We specifically extracted the well-known bundle iACT that carries olfactory information from the antennal lobe to a lateral horn and mushroom body. (e) Bundles that we found in our data (white) and in FlyCircuit (yellow).

[312–319]. And the visualization and user access are also simpler [320–323]. Vectorization is therefore crucial. For example, it would be impossible for users to remotely access the ∼1 exabytes of raster data and extract whole-brain structural information.

Our strategy must also deal with the incorporation of high-resolution or functional information in the database. In fact, "meta data" must be associated with the connectome down to local brain regions. For that, there are many powerful candidate algorithms for vectorized models [324–326].

6.4.2. Development of new algorithms

In addition to those mentioned above, other algorithms will be required, specifically for the large data sets of mouse and human brains. SYNAPSE specifically plans to implement different deep-learning schemes for tomographic reconstruction and segmentation.

There are for example many interesting developments using deep learning for image segmentation. Convolutional Neural Networks (CNN) models [327–331] – particularly the U-Net model and its variants – have been successfully shown for the segmentation of biological features in microscopy.

6.4.3. Overall data management and distribution

This poses several challenges due to the distributed nature and massive size of the SYNAPSE data. These challenges are similar, although with much bigger magnitude than other large-scale research projects such as the Large Hadron Collider (LHC) and the Square Kilometer Array (SKA) — requiring massive amounts of data to be collected, processed and distributed to local and international users. Their experience can assist in handling our own problems. Solutions relevant to SYNAPSE include:

- scalable data workflows for pre-processing, storing and archiving the data
- minimizing the distance to transfer data from acquisition to processing
- distributing and processing data with a tiered HPC framework
- high speed network connections of participating HPC centers
- high-speed input/output storage systems matching the connection bandwidth

Fig. 35 shows the scheme of the SYNAPSE data management implementing a tiered structure. The primary data from the various sources are consolidated at a central Tier-0 repository that is coupled to a HPC and hierarchical storage system for data compression/archiving and primary analysis. The processed data can be distributed to partner Tier-1 centers for redundancy and to local users for secondary analysis.

The National Supercomputing Center (NSCC) in Singapore is the Tier-1 center because of its extensive multiple redundant 100 G high speed links (100 Gbps) to major regions by APONET and the Asia-Pacific Europe Ring (AER). The two petascale supercomputers (aggregate 10 PFLOPS), and the GPU processors of NSCC will process vectorial wire diagram information to construct the whole brain connectome maps and will manage the data over its multi-petabyte parallel files systems (I/O >150 Gbytes/sec read/write) for user access.

This strategy for large scale scientific computer tasks was successfully tested by the GenomeAsia100K consortium [332]. The high-speed links were critical for data transfer of large genomic data sets from different sequencing centers in the US (Genentech), Korea (Macrogen) and India (Medgenome) to NSCC, where primary data could be centrally managed [333,334]. The high-bandwidth data transfer [335,336] – now reaching 11 GB/s – was demonstrated in the 2021 Data Mover Challenge, organized by the 100 G intercontinental infrastructure network [337].

Using such rapid data transfer and the access to HPC resources, the GenomeAsia100K consortium accelerated their large-scale analysis to uncover genomic variants critical for the Asian population, discovering variants for disease susceptibilities — which is also important for SYNAPSE.

In parallel, with the Singapore SG10K project NSCC supports a genome sequencing farm with direct high-speed InfiniBand interconnections for direct read/write into secure disks at the NSCC ASPIRE1 supercomputer data center 13 petabyte parallel file storage system (two kilometers away). This demonstrates that data gathering sites can be at a reasonable distance from the computing servers without suffering too much latency — a model that SYNAPSE will adopt for its Data Source and Tier-0 HPC facilities [338].

6.4.4. Orchestration of computation workflows

The processing pipeline to extract the connectome from the primary tomographic data at the Tier-0 centers involves multiple stages, each requiring different applications and tools. Given the complexity and iterative development cycle of SYNAPSE data processing, special consideration is given to the reproducibility and scalability of the pipeline. These depend on the ability (i) to deploy and track different versions of the workflows and tools in a portable manner, and (ii) to orchestrate the stage-wise execution of the workflow and, if possible, to parallelize and distribute the workload across multiple computer nodes.

In addition to storing the information on the samples, the measurement and the previous data processing parameters, a laboratory imaging management system (LIMS) is crucial for the supervision of data and specimens across the consortium. Commercially available LIMS systems handle data in one laboratory. This is not sufficient for our case, since our LIMS will need to also manage a large amount of specimens, different (existing or newly developed) processing algorithms and the processing history, distributed at different SYNAPSE partners.

For computation, our LIMS also needs to incorporate a computer resource management system (CRMS) to design the automated processing pipeline using different processing algorithms. And to assign data processing to each different type of newly generated intermediate data, depending on the results of the intermediate analysis and on the availability of computing resources. The automated sequence should also allow human intervention, if needed, by an online supervisory team.

In addition to the architecture of workflows to organize and manage the data, by the LIMS and CRMS, a robust framework security is required to distribute the data to SYNAPSE partners (e.g., regional Tier-1 centers) and external users. Such a system could control data access through an authentication and authorization system that can be federated across the consortium. One potential candidate is Rucio [339], developed for the ATLAS experiment at the LHC.

Specifically, SYNAPSE will integrate the containers (e.g., Singularity software platform [340]) runtime environment to the CRMS to package the code and its dependencies as an image built from user-defined specifications. These images can be executed in compatible computing environments ensuring portability. Furthermore, these container images can be tagged by version and stored in a repository for distribution. [341].

Several tools have been developed for orchestrating pipelines for processing biological data (e.g., NextFlow, Common Workflow Language). The orchestrator builds a directed acyclic graph of the different stages and uses it to track the execution as it dispatches the compute jobs to the nodes in a fault-tolerant manner by handling any errors and retries.

By using a combined approach of workflow orchestrator and container environments, the data processing pipeline can be developed in a reproducible manner even with the distributed nature of the work in the SYNAPSE consortium and scaled up to meet the data-intensive needs by facilitating the parallelization of stages across multiple nodes.

6.4.5. Exabyte data and exaflop computation

With all the compression schemes implemented which reduced data of one human brain to ∼10 PB, the current tiered data processing pipeline is feasible. However, beyond the first demonstration of brain mapping of one human brain, the data processing faces the huge challenge of mapping multiple brains.

The amount of raw image data, ≈1 exabyte for a human brain, making technically infeasible the transport of such a volume of data through international internet connections. Therefore, meeting the corresponding needs will not be possible with a single Tier-1 center with a hub-and-spoke configuration to Tier-0 HPCs. Instead, a distributed HPC processing network as part of a Global Research Platform [342] might be a suitable strategy. Within Asia, the APRP (Asia Pacific Research Platform) started its tests, and SYNAPSE members are part of this platform.

The fast development of graphic processing units (GPU) is crucial for SYNAPSE. New tomographic reconstruction and segmentation algorithms, using deep-learning toolkits (such as Torch [343]), can achieve ten times the acceleration through the use of GPU computing.

By integrating the data and computing resources across multiple sites, we expect to be able to handle data-intensive workflows at the exascale level for SYNAPSE and beyond, without building a new data processing and storage facility.

7. Concluding remarks

We trust that the extensive and detailed discussion of the SYNAPSE enterprise was able to deliver some essential messages. The most important are the following three.

First, the task is massive and requires hard work in different directions, including sources, optics, detectors, staining, coordination, data processing, data storage and availability, plus other imaging techniques beyond phase-contrast radiology. This requires a huge and continuing effort.

Second, the strategy to attack a single problem with multiple synchrotron facilities is a novelty that will influence the entire field. This new paradigm of collaboration specifically changes how the scientific community can look at the use of advanced X-ray sources and other such user-based sources for basic sciences.

Third, the objective of the enterprise is absolutely justified on scientific ground. And can become one of the most important challenges attacked by the scientific community in our time. In short, it is an enterprise worth our best efforts.

Declaration of competing interest

The authors declare that they have no known competing financial interests or personal relationships that could have appeared to influence the work reported in this paper.

Acknowledgments

This work is supported by National Science and Technology Council (NSTC, Taiwan.107-2119-M-001-047; 109-2123-M-001-001; 108-2923-M-001-008-MY2; 107-2923-M-001-012-MY3); National University of Singapore (R-184-000-261-101, and R-184-000-310-733 to Chian-Ming Low; R-184-000-289-133 to Chian-Ming Low and Eng Soon Tok); National University of Singapore & National Supercomputing Center (N-184-000-042-001 to Chian-Ming Low). We thank SYNAPSE Project for the technical support. This work was partially supported by the Brain Research Center under the Higher Education Sprout Project, co-funded by the Ministry of Education and the NSTC in Taiwan. The BIB beamline of Taiwan Photon Source of National Synchrotron Radiation Research Center (NSRRC) is supported by SYNAPSE project and NSTC (Taiwan).

Appendix. Computer vision assisted feature enhancer (CAFE)

The CAFE process was developed to identify somata of animal brains in 3D high-resolution images and to locate their centers. Although using the decision tree models may provide strong interpretability and good efficiency, however, the simple structures of decision tree models often cause poor performance in testing data due to overfitting. CAFE also uses artificial neural networks [344–353], which demonstrated significant power in object detection.

CAFE locates the centers of somata from the 3D images of Drosophila brains in three steps. First, it processes the images to identify soma candidates, then extracts characteristic features of these candidates, and finally uses machine learning with these features to achieve automated detection. Specifically, in the first step the Difference of Gaussian (DoG) algorithm locates regions that potentially contain blob-shaped objects.

After finding such potential regions, general and neurobiology features are extracted. General features include textures extracted by Gabor filtering and co-occurrence matrices, and local descriptor extracted by SIFT (Scale-Invariant Feature Transform) and shape context descriptor. The neurobiology features include edge lengths and angles extracted by edge filter or the Hidden Markov Model (HMM), and density extracted by DoG.

Finally, all the features are sent to classifiers for training and testing. Note that these features could be also used in other tasks, such as image alignment, stitching, iterative reconstruction and sparse tomography.

Most of the previous works on automated soma detection dealt with 2D image stacks with anisotropic resolution [354–356]. As the 3D data from visible fluorescent microscopy of animal brains increased, new processing methods were developed [357]. Many algorithms achieved significant improvements in soma detection using different approaches [358–366]. Furthermore, 3D image processing took advantage of machine learning: many studies reported success in improving the automated soma detection using deep neural networks [367–377].

However, our extensive tests show that almost all these methods fail to achieve satisfactory detection for our 3D X-ray microtomography images. They produce many false positive identifications or require human intervention during the process. The failure, in general, can be attributed to the weak, and often inhomogeneous, contrast of high-resolution X-ray images and tomography reconstructions. It is not easy to obtain an universal threshold for classification as for fluorescence or electron microscopy. However, our isotropic 3D resolution enabled us to develop a new strategy for feature detection.

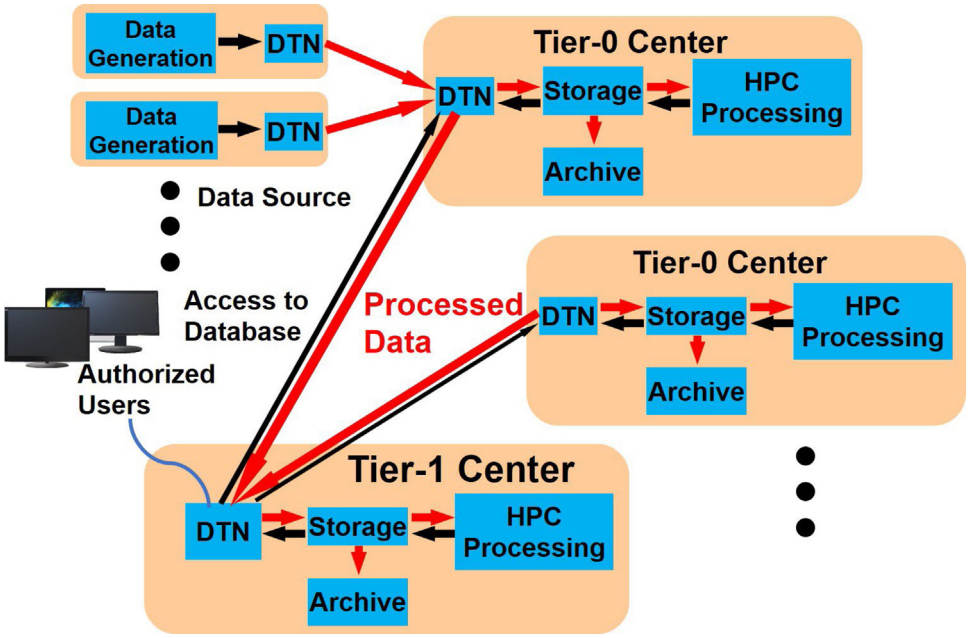

Fig. 35. Diagram of architecture for SYNAPSE computation. The data is transferred via data transfer nodes (DTN) by high-speed network links to nearby Tier-0 centers for storage, archiving and primary processing. The processed data is transferred to Tier-1 center for assembling and secondary analysis. Tier-1 center is also the portal for accessing the whole brain connectome database from authenticated users.

To extract features, a baseline approach is to use the convolutional neural network (CNN) to extract latent features from raw images. However, deep learning models require a huge amount of labeled data to train their kernels. Furthermore, it is difficult to integrate the domain knowledge via labeled data – for example just showing where the somata are without further descriptions – into the deep learning architectures. Our CAFE approach solved these problems by extracting discriminative features from the images in collaboration with neurobiology experts. The flowchart of feature extraction is shown in Fig. 36.

The 3D image data for the whole brain is first partitioned into cubes with $50 \times 50 \times 50$ pixels. Substantial overlaps are left between these "data boxes", 25 pixels in each direction, to guarantee not to miss relevant features at the boundaries.

Each of the data boxes is processed by a structure-aware adaptive thresholding method to binarize and yield candidate somata. Finally, computer vision methods extract features with the aid of neurobiology information on the structural features of neurons and the neural network.

Adaptive thresholding was implemented to deal with the above-mentioned problems caused by the weak absorption contrast of high-resolution X-ray imaging, by image noise, by background from the X-ray source and by the low contrast from small metal labeling particles. Note that a gray scale threshold can be defined for each data box for identifying soma candidates. To avoid missing true features (false negatives), or extracting false features from noise or image artifacts (false positives), CAFE exploited the Otsu's method [378–380] for adaptive thresholding.

Specifically, our Otsu process calculates the L-bin normalized intensity histogram for each data box. Then, a threshold t is derived by minimizing the intra-class variance $\sigma^2_{intra}(t)$, defined as follows:

$$\sigma^2_{intra}(t) = p_0(t)\,\sigma^2_0(t) + p_1(t)\,\sigma^2_1(t)\,,$$

where $p_0(t)$ and $p_1(t)$ are the probabilities of the two classes (bright and dark) separated by the threshold t, and $\sigma^2_0(t)$ and $\sigma^2_1(t)$ are their variances. The class probabilities $p_0(t)$ and $p_1(t)$ are derived from the L-bin normalized histogram:

$$p_0(t) = \sum_{i=0}^{t-1} h(i)$$

$$p_1(t) = \sum_{i=t}^{L} h(i)\,,$$

where $h(i)$ is the probability of the ith bin. Note that minimizing the intra-class variance in histogram has been proved to be equivalent to maximizing the inter-class variance [378] $\sigma^2_{inter}(t)$, defined as follows:

$$\sigma^2_{inter}(t) = \sigma^2 - \sigma^2_{intra}(t) = p_0(t)\,p_1(t)\,[\mu_0(t) - \mu_1(t)]^2\,,$$

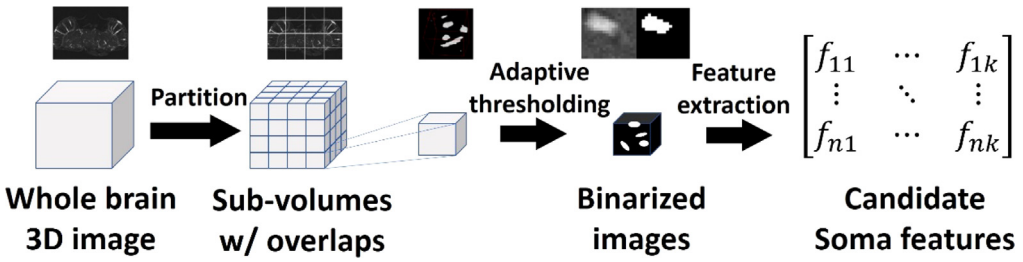

Fig. 36. Flow chart of CV-assisted Feature Enhancer (CAFE).

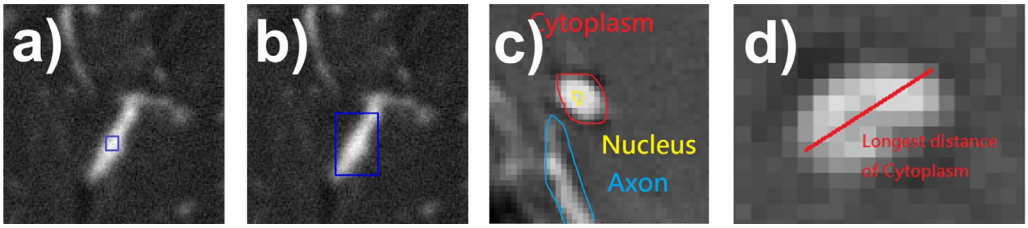

Fig. 37. (a) and (b) show the adaptive thresholding results using Otsu's method (a) and our method (b). (c) and (d) show an example of feature extraction. (c) The candidate soma. (d) Longest dimension of cytoplasm.

where $\mu_0(t)$ and $\mu_1(t)$ are the average intensities of class 0 and 1. This strategy is likely to require less computer time than directly deriving $\sigma^2_{intra}(t)$.

Overall, the Otsu's method first calculates histograms and probabilities of each intensity level and searches the maximum $\sigma^2_{inter}(t)$ for $t = 1, \ldots, L$. The 2D Otsu's method also considers the gray-level value of each pixel as well as the average value of its neighbors: this improves its robustness, especially for noisy images.

Note that our Otsu's process could yield undesired results. For example, Fig. 37(a) shows that the blue box does not cover the entire white (soma candidate) area, due to the gradual decay of the highest intensity from the center to the boundary. Thus, the blue box marks the location of the soma, but does not cover the entire soma area allowing CAFE to extract relevant soma features.

To correct this problem, we only utilized the Otsu's method as the first step to locate a starting point (as in Fig. 37(a)). CAFE then searches along six directions to find the boundaries of the candidate soma. The corresponding improved result is shown in Fig. 37(b). A genuine candidate soma is reported only if the extracted box is large enough (500 to 10,000 voxels) to match the typical soma size.

After identifying candidate somata, the next step was to extract for them with computer vision (CV) methods characteristic morphology features. These features correspond to the shapes of candidate somata and of their axons: for example, the length or the ratio between the nucleus and cytoplasm and the shape of the soma axon connection. Fig. 37(c) shows the identified nucleus, cytoplasm and axons. Fig. 37(d) is an example of the longest distance of cytoplasm. Finally, based on the features identified by CAFE for a substantial number of somata, classifiers specific for different machine learning process (e.g., SVM, random forests and neural networks) were elaborated and used in the soma-identification processing of other images.

Results of Case Studies of Drosophila Brain

CAFE was first applied using one Drosophila brain for training and five for testing. A five-fold cross-validation was adopted to avoid overfitting. For validation, we used Support Vector Machine (SVM) with RBF (Radial Basic Function) kernel in Scikit-learn API [381] as the classifier. Each brain was described as a 3D tensor with 16 bit voxel data. The ground-truth somata were manually labeled by neurobiology experts.

Table 1 presents the results of CAFE detection for the 5 Drosophila brains. The precision and recall are at least 73.89% and 85.14%. The results show that the extracted features are discriminative. Furthermore, the CAFE performances are better than those of human identification, but of course require much less time and can process large data sets.

To further understand the false positives and false negatives, Fig. 38 visualizes four cases in brain #1. The false positives in Fig. 38(a) and (b) look round and bright, but they are not somata according to the neurobiology experts. Indeed, the one in Fig. 42(a) is located in the middle of an axon, whereas the other is a bouton. As to false negatives, Fig. 38(c) and (d) present two undetected somata. Both lie in an area with similar intensity levels. Therefore, it is hard to isolate them with any thresholding method. According to the neurobiology experts, it is difficult to classify them with the current resolution.

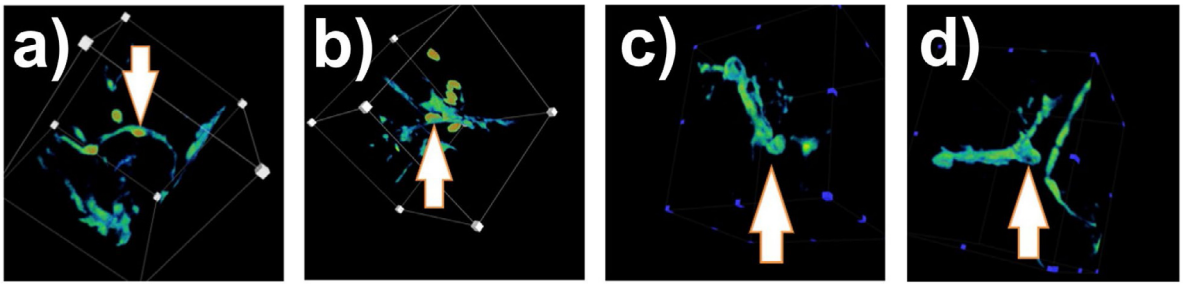

Fig. 38. Visualization of misclassified cases. (a) False positive; (b) False positive; (c) False negative; (d) False negative.

Table 1
Performance of CAFE in the testing Drosophila brains.

Brain no.	#1	#2	#3	#4	#5
Reported Soma	330	216	246	261	295
True positive	263	149	174	199	91
False positive	22	40	41	13	32
False negative	12	26	8	5	7
Precision (%)	91.64	78.84	80.93	93.87	73.39
Recall (%)	95.64	85.14	95.60	94.55	92.86

References

[1] G. Margaritondo, Introduction to Synchrotron Radiation, Oxford, New York, 1988;
G. Margaritondo, Elements of Synchrotron Light for Biology, Chemistry, and Medical Research, Oxford, New York, 2002.
[2] W.C. Röntgen, Über eine neue Art von Strahlen, in: Sitzungsberichte Der Physikalisch Medizinischen Gesellschaft Zu Würzburg, vol. 29, 1895, pp. 132–141.
[3] S. Mobilio, F. Boscherini, C. Meneghini, Synchrotron Radiation Basics, Methods and Applications, Springer, Berlin, 2015.
[4] A. Einstein, Zur Elektrodynamik bewegter körper, Ann. Phys. 322 (1905) 891–921, http://dx.doi.org/10.1002/andp.19053221004.
[5] J. Rafelski, Relativity Matters: From Einstein's EMC2 to Laser Particle Acceleration and Quark-Gluon Plasma, Springer, Berlin, 2017.
[6] Y. Hwu, G. Margaritondo, Synchrotron radiation and X-ray free electron lasers (X-FELs) explained to all users, active and potential, J. Synchrotron Radiat. 28 (2021) 1014–1029, http://dx.doi.org/10.1107/S1600577521003325.
[7] H.C. Pollock, The discovery of synchrotron radiation, Amer. J. Phys. 51 (1983) 278–280, http://dx.doi.org/10.1119/1.13289.
[8] F.R. Elder A.M. Gurewitsch, R.V. Langmuir, H.C. Pollock, Radiation from electrons in a synchrotron, Phys. Rev. 71 (1947) 829–830, http://dx.doi.org/10.1103/PhysRev.71.829.5.
[9] G. Margaritondo, Coherence: Elementary introduction to a quantum revolution in X-ray science, in: A. Di Cicco, G. Giuli, A. Trapananti (Eds.), Synchrotron Radiation Science and Applications, in: Springer Proceedings in Physics, vol. 220, Springer, Heidelberg, 2021, http://dx.doi.org/10.1007/978-3-030-72005-6_1.
[10] J.M.J. Madey, Stimulated emission of bremsstrahlung in a periodic magnetic field, J. Appl. Phys. 42 (1971) 1906–1913, http://dx.doi.org/10.1063/1.1660466.
[11] R. Bonifacio, L. De Salvo, P. Pierini, N. Piovella, C. Pellegrini, Spectrum, temporal structure, and fluctuations in a high-gain free-electron laser starting from noise, Phys. Rev. Lett. 73 (1994) 70–73, http://dx.doi.org/10.1103/PhysRevLett.73.70.
[12] E. Allaria, R. Appio, L. Badano, W.A. Barletta, S. Bassanese, S.G. Biedron, A. Borga, E. Busetto, D. Castronovo, P. Cinquegrana, S. Cleva, D. Cocco, M. Cornacchia, P. Craievich, I. Cudin, G. D'Auria, M. Dal Forno, M.B. Danailov, R. De Monte, G. De Ninno, P. Delgiusto, A. Demidovich, S. Di Mitri, B. Diviacco, A. Fabris, R. Fabris, W. Fawley, M. Ferianis, E. Ferrari, S. Ferry, L. Froehlich, P. Furlan, G. Gaio, F. Gelmetti, L. Giannessi, M. Giannini, R. Gobessi, R. Ivanov, E. Karantzoulis, M. Lonza, A. Lutman, B. Mahieu, M. Milloch, S.V. Milton, M. Musardo, I. Nikolov, S. Noe, F. Parmigiani, G. Penco, M. Petronio, L. Pivetta, M. Predonzani, F. Rossi, L. Rumiz, A. Salom, C. Scafuri, C. Serpico, P. Sigalotti, S. Spampinati, C. Spezzani, M. Svandrlik, C. Svetina, S. Tazzari, M. Trovo, R. Umer, A. Vascotto, M. Veronese, R. Visintini, M. Zaccaria, D. Zangrando, M. Zangrando, Highly coherent and stable pulses from the FERMI seeded free-electron laser in the extreme ultraviolet, Nat. Photon. 6 (2012) 699–704, http://dx.doi.org/10.1038/nphoton.2012.233.
[13] G. Margaritondo, Y. Hwu, Imaging with coherent X-rays: From the early synchrotron tests to SYNAPSE, J. Imaging 7 (2021) 132, http://dx.doi.org/10.3390/jimaging7080132.
[14] G. Margaritondo, G. Tromba, Coherence-based edge diffraction sharpening of X-ray images: A simple model, J. Appl. Phys. 85 (1999) 3406–3408, http://dx.doi.org/10.1063/1.369697.
[15] Y. Hwu, H.H. Shieh, M.J. Lu, W.L. Tsai, H.M. Lin, W.C. Goh, B. Lai, J.H. Je, C.K. Kim, D.Y. Noh, H.S. Youn, G. Tromba, G. Margaritondo, Coherence-enhanced synchrotron radiology: Refraction versus diffraction mechanisms, J. Appl. Phys. 86 (1999) 4613–4619, http://dx.doi.org/10.1063/1.371411.
[16] T. Hara, T. Tanaka, T. Tanabe, X.M. Marechal, S. Okada, H. Kitamura, In-vacuum undulators of SPring-8, J. Synchrotron Radiat. 5 (1998) 403–405, http://dx.doi.org/10.1107/S0909049597015720.
[17] T. Hara, M. Yabashi, T. Tanaka, T. Bizen, S. Goto, X.M. Maréchal, T. Seike, K. Tamasaku, T. Ishikawa, H. Kitamura, The brightest X-ray source: A very long undulator at SPring-8, Rev. Sci. Instrum. 73 (2002) 1125–1128, http://dx.doi.org/10.1063/1.1445866.
[18] M. Yabashi, T. Mochizuki, H. Yamazaki, S. Goto, H. Ohashi, K. Takeshita, T. Ohata, T. Matsushita, K. Tamasaku, Y. Tanaka, T. Ishikawa, Design of a beamline for the SPring-8 long undulator source 1, Nucl. Instrum. Methods A 467–468 (2001) 678–681, http://dx.doi.org/10.1016/S0168-9002(01)00444-2.
[19] D. Einfeld, M. Plesko, A modified QBA optics for low emittance storage-rings, Nucl. Instrum. Methods A 335 (1993) 402–416, http://dx.doi.org/10.1016/0168-9002(93)91224-B.

[20] R. Chasman, G.K. Green, E.M. Rowe, Preliminary design of a dedicated synchrotron radiation facility, IEEE Trans. Nucl. Sci. 22 (1975) 1765, http://dx.doi.org/10.1109/TNS.1975.4327987.

[21] P.F. Tavares, S.C. Leemann, M. Sjöström, Å. Andersson, The MAX IV storage ring project, J. Synchrotron Radiat. 21 (2014) 862–877, http://dx.doi.org/10.1107/S1600577514011503, (https://www.maxiv.lu.se).

[22] Pantaleo Raimondi, ESRF-EBS: The extremely brilliant source project, Synchrotron Radiat. News 29 (2016) 8–15, http://dx.doi.org/10.1080/08940886.2016.1244462, (ESRF-EBS).

[23] L. Liu, N. Milas, A.H.C. Mukai, X.R. Resende, F.H. de Sá, The Sirius project, J. Synchrotron Radiat. 21 (2014) 904–911, http://dx.doi.org/10.1107/S1600577514011928, (https://www.lnls.cnpem.br/sirius-en/).

[24] H. Hama, T. Muto, F. Hinode, Ground design of a 3 GeV accelerator-complex for the synchrotron light in Tohoku, Japan (SLiT-J), J. Phys.: Conf. Ser. 425 (2013) 072010, http://dx.doi.org/10.1088/1742-6596/425/7/072010, (The SLiT-J in Japan, http://www.slitj.tagen.tohoku.ac.jp).

[25] Y. Jiao, G. Xu, X.H. Cui, Z. Duan, Y.Y. Guo, P. He, D.H. Ji, J.Y. Li, X.Y. Li, C. Meng, Y.M. Peng, S.K. Tian, J.Q. Wang, N. Wang, Y.Y. Wei, H.S. Xu, F. Yan, C.H. Yu, Y.L. Zhao, Q. Qin, The HEPS project, J. Synchrotron Radiat. 25 (2018) 1611–1618, http://dx.doi.org/10.1107/S1600577518012110.

[26] B.G. Cho, Y. Kim, S. Shin, T.Y. Koo, Comparative study of hard X-ray undulator beamline performance in the Korean 4GSR and the PLS-II, J. Korean Phys. Soc. 78 (2021) 467–475, http://dx.doi.org/10.1007/s40042-021-00062-w.

[27] P. Sunwong, SPS-II: A 4th generation synchrotron light source in Southeast Asia - (SLRI), in: Proceedings of 13th International Particle Accelerator Conference, IPAC2022, Bangkok, Thailand, 2022, (SLRI new ring).

[28] Hitoshi Tanaka, Current status of the SPring-8 upgrade project, Synchrotron Radiat. News 27 (2014) 23–26, http://dx.doi.org/10.1080/08940886.2014.970935;
H. Tanaka, T. Ishikawa, S. Goto, S. Takano, T. Watanabe, M. Yabashi, SPring-8 upgrade project, in: K.S. Kim, I.S. Ko, K.R. Kim, V.R.W. Schaa (Eds.), Proceedings of 7th International Particle Accelerator Conference, IPAC2016, Busan, Korea, 2016, WEPOW019. (SPring-8 upgrade).

[29] P. Emma, R. Akre, J. Arthur, R. Bionta, C. Bostedt, J. Bozek, A. Brachmann, P. Bucksbaum, R. Coffee, F.-J. Decker, Y. Ding, D. Dowell, S. Edstrom, A. Fisher, J. Frisch, S. Gilevich, J. Hastings, G. Hays, Ph Hering, Z. Huang, R. Iverson, H. Loos, M. Messerschmidt, A. Miahnahri, S. Moeller, H.-D. Nuhn, G. Pile, D. Ratner, J. Rzepiela, D. Schultz, T. Smith, P. Stefan, H. Tompkins, J. Turner, J. Welch, W. White, J. Wu, G. Yocky, J. Galayda, First lasing and operation of an angstrome-wavelength free-electron laser, Nat. Photon. 4 (2010) 641–647, http://dx.doi.org/10.1038/NPHOTON.2010.176.

[30] S.V. Milton, E. Gluskin, N.D. Arnold, S. Berg, W. Berg, Y.C. Chae, E.A. Crosbie, R.J. Dejus, P.D. Hartog, H. Friedsam, J.N. Galayda, A. Grelick, J. Jones, Y. Kang, S. Kim, J.W. Lewellen, A.H. Lumpkin, J.R. Maines, G.M. Markovich, E.R. Moog, A. Nassiri, E. Trakhtenberg, I. Vasserman, N. Vinokurov, D.R. Walters, J. Wang, B. Yang, Status of the advanced photon source low-energy undulator test line, Nucl. Instrum. Methods. A 407 (1998) 210–214, http://dx.doi.org/10.1016/S0168-9002(97)01398-3.

[31] E. Kako, P. Pierini, C.E. Reece, TESLA's high gradient march: Thirty years anniversary of TESLA technology collaboration (TTC), CERN Courier 60 (2020) 35–38, https://www.osti.gov/servlets/purl/1699504, (https://tesla.desy.de/).

[32] G. Grübel, G. Stephenson, C. Gutt, H. Sinn, T. Tschentscher, XPCS at the European X-ray free electron laser facility, Nucl. Instrum. Methods Phys. Res. Sect. B 262 (2007) 357–367, http://dx.doi.org/10.1016/j.nimb.2007.05.015, (https://xfel.eu).

[33] I. Eom, S.H. Chun, J.H. Lee, D. Nam, R. Ma, J. Park, S. Park, S.H. Park, H. Yang, I. Nam, M.H. Cho, C.H. Shim, G.K., C.K. Min, H. Heo, H.S. Kang, C. Kim, Recent progress of the PAL-XFEL, Appl. Sci. 12 (2022) 1010, http://dx.doi.org/10.3390/app12031010, (http://pal.postech.ac.kr/paleng/).

[34] C. Milne, T. Schietinger, M. Aiba, A. Alarcon, J. Alex, A. Anghel, V. Arsov, C. Beard, P. Beaud, S. Bettoni, M. Bopp, H. Brands, M. Brönnimann, I. Brunnenkant, M. Calvi, A. Citterio, P. Craievich, M. Csatari Divall, M. Dällenbach, M. D'Amico, A. Dax, Y. Deng, A. Dietrich, R. Dinapoli, E. Divall, S. Dordevic, S. Ebner, C. Erny, H. Fitze, U. Flechsig, R. Follath, F. Frei, F. Gärtner, R. Ganter, T. Garvey, Z. Geng, I. Gorgisyan, C. Gough, A. Hauff, C. Hauri, N. Hiller, T. Humar, S. Hunziker, G. Ingold, R. Ischebeck, M. Janousch, P. Juranić, M. Jurcevic, M. Kaiser, B. Kalantari, R. Kalt, B. Keil, C. Kittel, G. Knopp, W. Koprek, H. Lemke, T. Lippuner, D. Llorente Sancho, F. Löhl, C. Lopez-Cuenca, F. Märki, F. Marcellini, G. Marinkovic, I. Martiel, R. Menzel, A. Mozzanica, K. Nass, G. Orlandi, C. Ozkan Loch, E. Panepucci, M. Paraliev, B. Patterson, B. Pedrini, M. Pedrozzi, P. Pollet, C. Pradervand, E. Prat, P. Radi, J.-Y. Raguin, S. Redford, J. Rehanek, J. Réhault, S. Reiche, M. Ringele, J. Rittmann, L. Rivkin, A. Romann, M. Ruat, C. Ruder, L. Sala, L. Schebacher, T. Schilcher, V. Schlott, T. Schmidt, B. Schmitt, X. Shi, M. Stadler, L. Stingelin, W. Sturzenegger, J. Szlachetko, D. Thattil, D. Treyer, A. Trisorio, W. Tron, S. Vetter, C. Vicario, D. Voulot, M. Wang, T. Zamofing, C. Zellweger, R. Zennaro, E. Zimoch, R. Abela, L. Patthey, H.-H. Braun, Swissfel: The swiss X-ray free electron laser, Appl. Sci. 7 (2017) http://dx.doi.org/10.3390/app7070720, (https://www.psi.ch/swissfel/).

[35] Z. Zhao, D. Wang, Z. Yang, L. Yin, SCLF: An 8-GeV CW SCRF Linac-based X-ray FEL facility in Shanghai, in: Proceedings of the International Free Electron Laser Conference, No. 38, FEL'17, Santa Fe, New Mexico, 2017, JACoW, Geneva, Switzerland, 2018, pp. 182–184, http://dx.doi.org/10.18429/JACoW-FEL2017-MOP055.

[36] K. Ayyer, A.J. Morgan, A. Aquila, H. Demirci, B.G. Hogue, R.A. Kirian, P.L. Xavier, C.H. Yoon, H.N. Chapman, A. Barty, Low-signal limit of X-ray single particle diffractive imaging, Opt. Express 27 (2019) 37816, http://dx.doi.org/10.1364/OE.27.037816.

[37] J. Miao, T. Ishikawa, I.K. Robinson, M.M. Murnane, Beyond crystallography: Diffractive imaging using coherent X-ray light sources, Science 348 (2015) 530–535, http://dx.doi.org/10.1126/science.aaa1394.

[38] T.-Y. Lan, P.-N. Li, T.-K. Lee, Method to enhance the resolution of X-ray coherent diffraction imaging for non-crystalline bio-samples, New J. Phys. 16 (2014) 033016, http://dx.doi.org/10.1088/1367-2630/16/3/033016.

[39] A.V. Martin, N.D. Loh, C.Y. Hampton, R.G. Sierra, F. Wang, A. Aquila, S. Bajt, M. Barthelmess, C. Bostedt, J.D. Bozek, N. Coppola, S.W. Epp, B. Erk, H. Fleckenstein, L. Foucar, M. Frank, H. Graafsma, L. Gumprecht, A. Hartmann, R. Hartmann, G. Hauser, H. Hirsemann, P. Holl, S. Kassemeyer, N. Kimmel, M. Liang, L. Lomb, F.R.N.C. Maia, S. Marchesini, K. Nass, E. Pedersoli, C. Reich, D. Rolles, B. Rudek, A. Rudenko, J. Schulz, R.L. Shoeman, H. Soltau, D. Starodub, J. Steinbrener, F. Stellato, L. Strüder, J. Ullrich, G. Weidenspointner, T.A. White, C.B. Wunderer, A. Barty, I. Schlichting, M.J. Bogan, H.N. Chapman, Femtosecond dark-field imaging with an X-ray free electron laser, Opt. Express 20 (2012) 13501–13512, http://dx.doi.org/10.1364/OE.20.013501.

[40] S. Marchesini, S. Boutet, A.E. Sakdinawat, M.J. Bogan, S. Bajt, A. Barty, H.N. Chapman, M. Frank, S.P. Hau-Riege, A. Szöke, C. Cui, D.A. Shapiro, M.R. Howells, J.C.H. Spence, J.W. Shaevitz, J.Y. Lee, J. Hajdu, M.M. Seibert, Massively parallel X-ray holography, Nat. Photonics 2 (2008) 560, http://dx.doi.org/10.1038/nphoton.2008.154.

[41] T. Shintake, Possibility of single biomolecule imaging with coherent amplification of weak scattering X-ray photons, Phys. Rev. E 78 (2008) 041906, http://dx.doi.org/10.1103/PhysRevE.78.041906.

[42] C. Kim, Y. Kim, C. Song, Enhancing resolution in coherent X-ray diffraction imaging, J. Phys.: Condens. Matter 28 (2016) 493001, http://dx.doi.org/10.1088/0953-8984/28/49/493001.

[43] Y. Takayama, K. Yonekura, Cryogenic coherent X-ray diffraction imaging of biological samples at SACLA: A correlative approach with cryo-electron and light microscopy, Acta Crystallogr. Sect. A: Found. Adv. 72 (2016) 179–189, http://dx.doi.org/10.1107/s2053273315023980.

[44] J.C.H. Spence, XFELs for structure and dynamics in biology, IUCrJ 4 (2017) 322–339, http://dx.doi.org/10.1107/S2052252517005760.

[45] T. Koyama, S. Ichimaru, T. Tsuji, H. Takano, Y. Kagoshima, T. Ohchi, H. Takenaka, Optical properties of MoSi2/Si multilayer Laue lens as nanometer X-ray focusing device, Appl. Phys. Express 1 (2008) 117003, http://dx.doi.org/10.1143/APEX.1.117003.

[46] H. Takano, T. Tsuji, T. Hashimoto, T. Koyama, Y. Tsusaka, Y. Kagoshima, Sub-15 nm hard X-ray focusing with a new total-reflection zone plate, Appl. Phys. Express 3 (2010) 076702, http://dx.doi.org/10.1143/APEX.3.076702.

[47] P. Kirkpatrick, A.V. Baez, Formation of optical images by X-rays, J. Opt. Soc. Amer. 38 (1948) 766–774, http://dx.doi.org/10.1364/JOSA.38.000766.
[48] Hans Wolter, Spiegelsysteme streifenden Einfalls als abbildende Optiken für Röntgenstrahlen, Ann. Der Phys. 445 (1952) 94–114, http://dx.doi.org/10.1002/andp.19524450108.
[49] S. Egawa, G. Yamaguchi, H. Motoyama, S. Owada, Y. Kubota, K. Tono, H. Ohashi, M. Yabashi, H. Mimura, An optical design of twin wolter mirrors for focusing and imaging experiments with soft X-ray free electron lasers, in: Advances in X-Ray/EUV Optics and Components XIV; Proc. SPIE, vol. 11108, 2019, p. 1110804, http://dx.doi.org/10.1117/12.2529039.
[50] H. Takano, K. Yokota, S. Aoki, A soft X-ray dark-field imaging microscope with Wolter-type grazing incidence mirrors, Jpn. J. Apl. Phys. 38 (1999) L1485–L1487, http://dx.doi.org/10.1143/JJAP.38.L1485.
[51] H. Takano, S. Aoki, M. Kumegawa, N. Watanabw, T. Ohhigashi, T. Aota, K. Yamamoto, H. Yokosuka, R. Tanoue, Y. Tsujita, M. Ando, X-ray scattering microscope with a Wolter mirror, Rev. Sci. Instrum. 73 (7) (2002) 2629–2633, http://dx.doi.org/10.1063/1.1487888.
[52] S. Matsuyama, S. Yasuda, J. Yamada, H. Okada, Y. Kohmura, M. Yabashi, T. Ishikawa, K. Yamauchi, 50-Nm-resolution full-field X-ray microscope without chromatic aberration using total-reflection imaging mirrors, Sci. Rep. 7 (2017) 46358, http://dx.doi.org/10.1038/srep46358.
[53] W.B. Yun, P.J. Viccaro, B. Lai, J. Chrzas, Coherent hard X-ray focusing optics and applications, Rev. Sci. Instrum. 63 (1992) 582, http://dx.doi.org/10.1063/1.1142711.
[54] S.R. Wu, Y. Hwu, G. Margaritondo, Hard-X-ray zone plates: Recent progress, Materials 5 (2012) 1752–1773, http://dx.doi.org/10.3390/ma5101752.
[55] H. Takano, Y. Suzuki, A. Takeuchi, Sub-100 nm hard X-ray microbeam generation with Fresnel zone plate optics, Japan. J. Appl. Phys. 42 (2003) L132–134, http://dx.doi.org/10.1143/JJAP.42.L132.
[56] T.N. Lo, Y.T. Chen, C.W. Chiu, C.J. Liu, S.R. Wu, I.K. Lin, C.I. Su, W.D. Chang, Y. Hwu, B.Y. Shew, C.C. Chiang, J.H. Je, G. Margaritondo, E-beam lithography and electrodeposition fabrication of thick nanostructured devices, J. Phys. D: Appl. Phys. 40 (2007) 3172–3176, http://dx.doi.org/10.1364/OE.19.019919.
[57] N. Kamijo, Y. Suzuki, H. Takano, S. Tamura, M. Yasumoto, A. Takeuchi, M. Awaji, Microbeam of 100 keV X ray with a sputtered-sliced Fresnel zone plate, Rev. Sci. Instrum. 74 (12) (2003) 5101–5104, http://dx.doi.org/10.1063/1.1614882.
[58] T. Koyama, H. Takano, S. Konishi, T. Tsuji, H. Takenaka, S. Ichimaru, T. Ohchi, Y. Kagoshima, Circular multilayer zone plate for high-energy X-ray nano-imaging, Rev. Sci. Instrum. 83 (2012) 013705, http://dx.doi.org/10.1063/1.3676165.
[59] H. Takano, S. Konishi, T. Koyama, Y. Tsusaka, S. Ichimaru, T. Ohchi, H. Takenaka, Y. Kagoshima, Point spread function measurement of an X-ray beam focused by a multilayer zone plate with narrow annular aperture, J. Synchrotron Radiat. 21 (2014) 446–448, http://dx.doi.org/10.1107/S1600577513034644.
[60] Y.T. Chen, T.N. Lo, C.W. Chiu, C.J. Liu, S.R. Wu, S.T. Jeng, C.C. Yang, J. Shiue, C.H. Chen, Y. Hwu, G.C. Yin, H.M. Lin, J.H. Je, G. Margaritondo, Fabrication of high aspect ratio Fresnel zone plates by E-beam lithography and electroplating, J. Synchrotron Radiat. 15 (2008) 170–175, http://dx.doi.org/10.1107/S0909049507063510.
[61] Y.T. Chen, T.N. Lo, Y.S. Chu, J. Yi, C.J. Liu, J.Y. Wang, C.L. Wang, C.W. Chiu, T.E. Hua, Y. Hwu, Q. Shen, G.C. Yin, K.S. Liang, H.M. Lin, J.H. Je, G. Margaritondo, Full-field hard X-ray microscopy below 30 nanometers: A challenging nanofabrication achievement, Nanotechnology 19 (2008) 395302, http://dx.doi.org/10.1088/0957-4484/19/39/395302.
[62] H.R. Wu, S.T. Chen, Y.S. Chu, R. Conley, N. Bouet, C.C. Chien, H.H. Chen, C.H. Lin, H.T. Tung, Y.S. Chen, G. Margaritondo, J.H. Je, Y. Hwu, Nanoresolution radiology of neurons, J. Phys. D 45 (2012) 242001, http://dx.doi.org/10.1088/0022-3727/45/24/242001.
[63] A. Snigirev, V. Kohn, I. Snigireva, A. Souvorov, B. Lengeler, Focusing high-energy X rays by compound refractive lenses, Appl. Opt. 37 (1998) 653–662, http://dx.doi.org/10.1364/AO.37.000653.1.
[64] C.G. Schroer, J. Tuemmler, B. Lengeler, M. Drakopoulos, A. Snigirev, I. Snigireva, Compound refractive lenses: High-quality imaging optics for the X-FEL, Proc. SPIE 4143 (2001) 60–68, http://dx.doi.org/10.1117/12.413680.
[65] H. Mimura, S. Handa, T. Kimura, H. Yumoto, D. Yamakawa, H. Yokoyama, S. Matsuyama, K. Inagaki, K. Yamamura, Y. Sano, K. Tamasaku, Y. Nishino, M. Yabashi, T. Ishikawa, K. Yamauchi, Breaking the 10 nm barrier in hard-X-ray focusing, Nat. Phys. 6 (2010) 122–125, http://dx.doi.org/10.1038/nphys1457.
[66] H.C. Kang, J. Maser, G.B. Stephenson, C. Liu, R. Conley, A.T. Macrander, S. Vogt, Nanometer linear focusing of hard-X-rays by a multilayer Laue lens, Phys. Rev. Lett. 96 (2006) 127401, http://dx.doi.org/10.1103/PhysRevLett.96.127401.
[67] T. Koyama, H. Takenaka, S. Ichimaru, T. Ohchi, T. Tsuji, H. Takano, Y. Kagoshima, Development of multilayer Laue lenses; (1) linear type, AIP Conf. Proc. 1365 (2011) 24–27, http://dx.doi.org/10.1063/1.3625296.
[68] T. Koyama, T. Tsuji, H. Takano, Y. Kagoshima, S. Ichimaru, T. Ohchi, H. Takenaka, Development of multilayer Laue lenses; (2) circular type, AIP Conf. Proc. 1365 (2011) 100–103, http://dx.doi.org/10.1063/1.3625314.
[69] S. Bajt, M. Prasciolu, H. Fleckenstein, M. Domaracký, H.N. Chapman, A.J. Morgan, O. Yefanov, M. Messerschmidt, Y. Du, K.T. Murray, V. Mariani, M. Kuhn, S. Aplin, K. Pande, P. Villanueva-Perez, K. Stachnik, J.P.J. Chen, A. Andrejczuk, A. Meents, A. Burkhardt, D. Pennicard, X. Huang, H. Yan, E. Nazaretski, Y.S. Chu, C.E. Hamm, X-ray focusing with efficient high-NA multilayer Laue lenses, Light Sci. Appl. 7 (2018) 17162, http://dx.doi.org/10.1038/lsa.2017.162.
[70] Y. Hwu, G. Margaritondo, Synchrotron radiation and sensors: A history of synergies, IEEE Sensors J. 21 (2021) 12764–12773, http://dx.doi.org/10.1109/JSEN.2020.3023292.
[71] T. Kameshima, A. Takeuchi, K. Uesugi, T. Kudo, Y. Kohmura, K. Tamasaku, K. Muramatsu, T. Yanagitani, M. Yabashi, T. Hatsui, Development of an X-ray imaging detector to resolve 200 nm line-and-space patterns by using transparent ceramics layers bonded by solid-state diffusion, Opt. Lett. 44 (2019) 1403–1406, http://dx.doi.org/10.1364/OL.44.001403.
[72] H. Takano, Y. Suzuki, K. Uesugi, A. Takeuchi, N. Yagi, PSF measurement of imaging detectors with an X-ray microbeam, Proc. SPIE 4499 (2001) 126–133, http://dx.doi.org/10.1117/12.450230.
[73] B.M. Weon, J.H. Je, Y. Hwu, G. Margaritondo, Phase contrast X-ray imaging, Int. J. Nanotechnol. 3 (2006) 280–297, http://dx.doi.org/10.1504/IJNT.2006.009584.
[74] A. Snigirev, V. Kohn, I. Snigireva, B. Lengeler, A compound refractive lens for focusing high-energy X-rays, Nature 384 (1996) 49–51, http://dx.doi.org/10.1038/384049a0.
[75] K.M. Sowa, B.R. Jany, P. Korecki, Multipoint-projection X-ray microscopy, Optica 5 (2018) 577–582, http://dx.doi.org/10.1364/OPTICA.5.000577.
[76] T.Y. Chen, Y.T. Chen, C.L. Wang, I.M. Kempson, W.K. Lee, Y.S. Chu, Y. Hwu, G. Margaritondo, Full-field microimaging with 8 keV X-rays achieves a spatial resolutions better than 20 nm, Opt. Express 19 (2011) 19919–19924, http://dx.doi.org/10.1364/OE.19.019919.
[77] Y.T. Chen, T.Y. Chen, J. Yi, Y.S. Chu, W.K. Lee, C.L. Wang, I.M. Kempson, Y. Hwu, V. Gajdosik, G. Margaritondo, Hard X-ray Zernike microscopy reaches 30 nm resolution, Opt. Lett. 36 (2011) 1269–1271, http://dx.doi.org/10.1364/OL.36.001269.
[78] D.S. Coburn, E. Nazaretski, W. Xu, M. Ge, C. Longo, H. Xu, K. Gofron, Z. Yin, H.H. Chen, Y. Hwu, W.K. Lee, Design, characterization, and performance of a hard x-ray transmission microscope at the national synchrotron light source II 18-ID beamline, Rev. Sci. Instrum. 90 (2019) 053701, http://dx.doi.org/10.1063/1.5088124.
[79] S.R. Wu, C.H. Lin, Y.S. Chen, Y.Y. Chen, Y. Hwu, Y.S. Chu, G. Margaritondo, At the frontiers of high-resolution hard-X-ray microscopy: An international programme, Phys. D: Appl. Phys. 46 (2013) 494005, http://dx.doi.org/10.1088/0022-3727/46/49/494005.

[80] S.V. Hull, A.D. Falcone, E. Bray, M. Wages, M. McQuaide, D.N. Burrows, Hybrid CMOS detectors for the Lynx X-ray surveyor high definition X-ray imager, J. Astron. Telescopes, Instrum. Syst. 5 (2) (2019) 021018, http://dx.doi.org/10.1117/1.JATIS.5.2.021018.
[81] J. Dudak, High-resolution X-ray imaging applications of hybrid-pixel photon counting detectors Timepix, Radiat. Meas. 137 (2020) 106409, http://dx.doi.org/10.1016/j.radmeas.2020.106409.
[82] C. Ponchut, M. Cotte, A. Lozinskaya, A. Zarubin, O. Tolbanov, A. Tyazhev, Characterisation of GaAs:Cr pixel sensors coupled to Timepix chips in view of synchrotron applications, J. Instrum. 12 (2017) C12023, http://dx.doi.org/10.1088/1748-0221/12/12/C12023.
[83] R. Ballabriga, J. Alozy, G. Blaj, M. Campbell, M. Fiederle, E. Frojdh, E.H.M. Heijne, X. Llopart, M. Pichotka, S. Procz, L. Tlustos, W. Wong, The Medipix3RX: A high resolution, zero dead-time pixel detector readout chip allowing spectroscopic imaging, J. Instrum. 8 (2013) http://dx.doi.org/10.1088/1748-0221/8/02/C02016.
[84] E. Wenger, S. Dahaoui, P. Alle, P. Parois, C. Palin, C. Lecomte, D. Schaniel, XPAD X-ray hybrid pixel detector for charge density quality diffracted intensities on laboratory equipment, Acta Crystallogr. B 70 (2014) 783–791, http://dx.doi.org/10.1107/S2052520614017338.
[85] C. Brönnimann, P. Trüb, Hybrid pixel photon counting X-ray detectors for synchrotron radiation, in: E. Jaeschke, S. Khan, J. Schneider, J. Hastings (Eds.), Synchrotron Light Sources and Free-Electron Lasers, Springer, Cham, 2019, pp. 1–33, http://dx.doi.org/10.1007/978-3-319-04507-8_36-2.
[86] A. Allahgholi, J. Becker, L. Bianco, A. Delfs, R. Dinapoli, P. Goettlicher, H. Graafsma, D. Greiffenberg, H. Hirsemann, S. Jack, R. Klanner, A. Klyuev, H. Krueger, S. Lange, A. Marras, D. Mezza, A. Mozzanica, S. Rah, Q. Xia, B. Schmitt, J. Schwandt, I. Sheviakov, X. Shi, S. Smoljanin, U. Trunk, J. Zhang, M. Zimmer, AGIPD, a high dynamic range fast detector for the European XFEL, J. Instrum. 10 (2015) C01023, http://dx.doi.org/10.1088/1748-0221/10/01/C01023.
[87] A. Kenter, R. Kraft, T. Gauron, Monolithic CMOS detectors for use as X-ray imaging spectrometers, in: O.H. Siegmund (Ed.), UV, X-Ray, and Gamma-Ray Space Instrumentation for Astronomy XXI, in: Proc. SPIE, vol. 11118, 2019, http://dx.doi.org/10.1117/12.2530000.
[88] G. Margaritondo, Y. Hwu, J.H. Je, Synchrotron light in medical and materials science radiology, La Riv. Del Nuovo Cimento 27 (2004) 1–40, http://dx.doi.org/10.1393/ncr/i2005-10004-0.
[89] H. Takano, H. Azuma, S. Shimomura, T. Tsuji, Y. Tsusaka, Y. Kagoshima, Development of hard X-ray dark-field microscope using full-field optics, Jpn. J. Appl. Phys. 55 (2016) 102401, http://dx.doi.org/10.7567/JJAP.55.102401.
[90] C.C. Chien, P.Y. Tseng, H.H. Chen, T.E. Hua, S.T. Chen, Y.Y. Chen, W.H. Leng, C.H. Wang, Y. Hwu, G.C. Yin, K.S. Liang, F.R. Chen, Y.S. Chu, H.I. Yeh, Y.C. Yang, C.S. Yang, G.L. Zhang, J.H. Je, G. Margaritondo, Imaging cells and sub-cellular structures with ultrahigh resolution full-field X-ray microscopy, Biotechnol. Adv. 31 (2013) 375–386, http://dx.doi.org/10.1016/j.biotechadv.2012.04.005.
[91] H.H. Chen, C.C. Chien, C. Petibois, C.L. Wang, Y.S. Chu, S.F. Lai, T.E. Hua, Y.Y. Chen, X. Cai, I.M. Kempson, Y. Hwu, G. Margaritondo, Quantitative analysis of nanoparticle internalization in mammalian cells by high resolution X-ray microscopy, J. Nanobiotechnol. 9 (2011) 14, http://dx.doi.org/10.1186/1477-3155-9-14.
[92] K. Yamamoto, N. Watanabe, A. Takeuchi, H. Takano, T. Aota, M. Fukuda, S. Aoki, Mapping of a particular element using an absorption edge with an X-ray fluorescence imaging microscope, J. Synchrotron Radiat. 7 (2000) 34–39, http://dx.doi.org/10.1107/S0909049599014260.
[93] T. Ohigashi, T. Aota, N. Watanabe, H. Takano, H. Yokosuka, S. Aoki, Time-laspe observation of electrolysis of copper sulfate with a full-field X-ray fluorescence imaging microscope, Japan. J. Appl. Phys. 47 (2008) 4742–4745, http://dx.doi.org/10.1143/JJAP.47.4742.
[94] M.E. Finnegan, N. Visanji, I. Romero-canelon, E. House, S. Rajan, J.F.W. Mosselmans, L. Hazrati, J. Dobson, J.F. Collingwood, Synchrotron XRF imaging of Alzheimer's disease basal Ganglia reveals linear dependence of high-field magnetic resonance microscopy on tissue iron concentration, J. Neurosci. Methods 319 (2019) 28–39, http://dx.doi.org/10.1016/j.jneumeth.2019.03.002.
[95] M. Shimura, H. Shindou, L. Szyrwiel, S.M. Tokuoka, F. Hamano, S. Matsuyama, M. Okamoto, A. Matsunaga, Y. Kita, Y. Ishizaka, K. Yamauchi, Y. Kohmura, R. Lobinski, I. Shimizu, T. Shimizu, Imaging of intracellular fatty acids by scanning X-ray fluorescence microscopy, FASEB J. 30 (2016) 4149–4158, http://dx.doi.org/10.1096/fj.201600569R.
[96] H. Takano, K. Yoshida, T. Tsuji, T. Koyama, Y. Tsusaka, Y. Kagoshima, Fast X-ray micro-CT for real-time 4D observation, J. Phys. Conf. Ser. 186 (2009) 012049, http://dx.doi.org/10.1088/1742-6596/186/1/012049.
[97] H. Takano, M. Morikawa, S. Konishi, H. Azuma, S. Shimomura, Y. Tsusaka, S. Nakano, N. Kosaka, K. Yamamoto, Y. Kagoshima, Development of real-time X-ray micro-tomography system, J. Phys. Conf. Ser. 463 (2013) 012025, http://dx.doi.org/10.1088/1742-6596/463/1/012025.
[98] K. Vegso, Y. Wu, H. Takano, M. Hoshino, A. Momose, Development of pink-beam 4D phase CT for in-situ observation of polymers under infrared laser irradiation, Sci. Rep. 9 (2019) 7404, http://dx.doi.org/10.1038/s41598-019-43589-6.
[99] Y. Wu, H. Takano, A. Momose, Time-resolved X-ray stroboscopic phase tomography using albot interferometer for dynamic deformation measurements, Rev. Sci. Instrum. 92 (2021) 043702, http://dx.doi.org/10.1063/5.0030811.
[100] W. Voegeli, K. Kajiwara, H. Kudo, T. Shirasawa, X. Liang, W. Yashiro, Multibeam X-ray optical system for high-speed tomography, Optica 7 (2020) 514–517, http://dx.doi.org/10.1364/OPTICA.384804.
[101] Y. Wang, X. Liu, K.S. Im, W.K. Lee, J. Wang, K. Fezzaa, D.L.S. Hung, J.R. Winkelman, Ultrafast X-ray study of dense-liquid-jet flow dynamics using structure-tracking velocimetry, Nature Phys. 4 (2008) 305–309, http://dx.doi.org/10.1038/nphys840.
[102] C. Kallepitis, M.S. Bergholt, M.M. Mazo, V. Leonardo, S.C. Skaalure, S.A. Maynard, M.M. Stevens, Quantitative volumetric Raman imaging of three dimensional cell cultures, Nature Commun. 8 (2017) 14843, http://dx.doi.org/10.1038/ncomms14843Kallepitis.
[103] H.H. Chen, T.T. Lee, A. Chen, Y. Hwu, C. Petibois, 3D digital pathology for a chemical-functional analysis of glomeruli in health and pathology, Anal. Chem. 90 (2018) 3811–3818, http://dx.doi.org/10.1021/acs.analchem.
[104] H. Thiele, S. Heldmann, D. Trede, J. Strehlow, S. Wirtz, W. Dreher, J. Berger, J. Oetjen, J.H. Kobarg, B. Fischer, P. Maass, 2D and 3D MALDI-imaging: Conceptual strategies for visualization and data mining, Biochim. Biophys. Acta. 1844 (2014) 117–137, http://dx.doi.org/10.1016/j.bbapap.2013.01.040.
[105] R. Noreen, C.C. Chien, M. Delugin, S. Yao, R. Pineau, Y. Hwu, M. Moenner, C. Petibois, Detection of collagens in brain tumors based on FTIR imaging and chemometrics, Anal. Bioanal. Chem. 401 (2011) 845–852, http://dx.doi.org/10.1007/s00216-011-4899-1.
[106] R. Noreen, M. Moenner, Y. Hwu, C. Petibois, FTIR spectro-imaging of collagens for characterization and grading of gliomas, Biotechnol. Adv. 30 (2012) 1432–1446, http://dx.doi.org/10.1016/j.biotechadv.2012.03.009.
[107] D. Gabor, A new microscopic principle, Nature 161 (1948) 777–778, http://dx.doi.org/10.1038/161777a0.
[108] S. Marchesini, H.N. Chapman, S.P. Hau-Riege, R.A. London, A. Szoke, H. He, M.R. Howells, H. Padmore, R. Rosen, J.C.H. Spence, U. Weierstall, Coherent X-ray diffractive imaging: Applications and limitations, Opt. Express 11 (2003) 2344–2353, http://dx.doi.org/10.1364/OE.11.002344.
[109] D. Sayre, Some implications of a theorem due to Shannon, Acta Cryst. 5 (1952) 843, http://dx.doi.org/10.1107/s0365110x52002276.
[110] J.R. Fienup, Reconstruction of a complex-valued object from the modulous of its Fourier transform using a support constraint, J. Opt. Soc. Am. A. 4 (1987) 118–123, http://dx.doi.org/10.1364/JOSAA.4.000118.
[111] J. Miao, P. Charalambous, J. Kirz, D. Sayre, Extending the methodology of X-ray crystallography to allow imaging of micromere-sized non-crystalline specimens, Nature 400 (1999) 342–344, http://dx.doi.org/10.1038/22498.
[112] J.N. Clark, J. Ihli, A.S. Schenk, Y.Y. Kim, A.N. Kulak, J.M. Campbell, G. Nisbet, F.C. Meldrum, I.K. Robinson, Three-dimensional imaging of dislocation propagation during crystal growth and dissolution, Nature Mater. 14 (2015) 780–784, http://dx.doi.org/10.1038/nmat4320.
[113] Y. Kohmura, K. Sawada, T. Ishikawa, Berry-phase translation of X-rays inside deformed crystal, Phys. Rev. Lett. 104 (2010) 244801, http://dx.doi.org/10.1103/PhysRevLett.104.244801.

[114] Y. Kohmura, K. Sawada, S. Fukatsu, T. Ishikawa, Controlling the propagation of X-ray waves inside a heteroepitaxial crystal containing quantum dots using Berry's phase, Phys. Rev. Lett. 110 (2013) 057402, http://dx.doi.org/10.1103/PhysRevLett.110.057402.
[115] D. Nam, J. Park, M. Gallagher-Jones, S. Kim, S. Kim, Y. Kohmura, H. Naitow, N. Kunishima, T. Yoshida, T. Ishikawa, C. Song, Imaging fully hydrated whole cells by coherent X-ray diffraction microscopy, Phys. Rev. Lett. 110 (2013) 098103, http://dx.doi.org/10.1103/PhysRevLett.110.098103.
[116] J.R. Fienup, Phase retrieval algorithms: A comparison, Appl. Opt. 21 (1982) 2758–2769, http://dx.doi.org/10.1364/AO.21.002758.
[117] V. Elser, Phase retrieval by iterated projections, J. Opt. Soc. Amer. 20 (2003) 40–55, http://dx.doi.org/10.1364/JOSAA.20.000040.
[118] H.H. Bauschke, P.L. Combettes, D.R. Luke, Phase retrieval, error reduction algorithm, and Fienup variants: A view from convex optimization, J. Opt. Soc. Amer. 19 (2002) 1334–1345, http://dx.doi.org/10.1364/JOSAA.19.001334.
[119] C.C. Chen, J. Miao, C. Wang, T. Lee, Application of optimization technique to noncrystalline X-ray diffraction microscopy: Guided hybrid input–output method, Phys. Rev. B 76 (2007) 064113, http://dx.doi.org/10.1103/PhysRevB.76.064113.
[120] C.F. Huang, K.S. Liang, Y. Hwu, T.K. Lee, Y. Joti, Y. Nishino, T. Ishikawa, Simulation of single bio particles in XFEL coherent diffraction–master curve for photon counts estimation, AIP Conf. Proc. 2054 (2019) 050006, http://dx.doi.org/10.1063/1.5084624.
[121] C.F. Huang, W.H. Chang, T.K. Lee, Y. Joti, Y. Nishino, T. Kimura, A. Suzuki, Y. Bessho, T.T. Lee, M.C. Chen, S.M. Yang, Y. Hwu, S.H. Huang, P.N. Li, P. Chen, Y.C. Tseng, C. Ma, T.L. Hsu, C.H. Wong, K. Tono, T. Ishikawa, K.S. Liang, XFEL coherent diffraction imaging for weakly scattering particles using heterodyne interference, AIP Adv. 10 (2020) 055219, http://dx.doi.org/10.1063/1.5129406.
[122] C.F. Huang, K.S. Liang, T.L. Hsu, T.T. Lee, Y.Y. Chen, S.M. Yang, H.H. Chen, S.H. Huang, W.H. Chang, P. Chen, T.K. Lee, K.E. Peng, C.C. Chen, C.Z. Shi, Y.F. Hu, G. Margaritondo, T. Ishikawa, C.H. Wong, Y. Hwu, Free-electron-laser coherent diffraction images individual drug-carrying liposome particles in solution, Nanoscale 10 (2018) 2820–2824, http://dx.doi.org/10.1039/C7NR09395K.
[123] D. Papahadjopoulos, T.M. Allen, A. Gabizon, E. Mayhew, K. Matthay, S.K. Huang, K.D. Lee, M.C. Woodle, D.D. Lasic, C. Redemann, Sterically stabilized liposomes: Improvements in pharmacokinetics and antitumor therapeutic efficacy, Proc. Natl. Acad. Sci. USA 88 (1991) 11460–11464, http://dx.doi.org/10.1073/pnas.88.24.11460.
[124] A. Gabizon, R. Catane, B. Uziely, B. Kaufman, T. Safra, R. Cohen, F. Martin, A. Huang, Y. Barenholz, Prolonged circulation time and enhanced accumulation in malignant exudates of doxorubicin encapsulated in polyethylene-glycol coated liposomes, Cancer Res. 54 (1994) 987–992.
[125] D.W. Northfelt, F.J. Martin, P. Working, P.A. Volberding, J. Russell, M. Newman, M.A. Amantea, L.D. Kaplan, Doxorubicin encapsulated in liposomes containing surface-bound polyethylene glycol: Pharmacokinetics, tumor localization, and safety in patients with AIDS-related Kaposi's sarcoma, J. Clin. Pharmacol. 36 (1996) 55–63, http://dx.doi.org/10.1002/j.1552-4604.1996.tb04152.x.
[126] I.A. Vartanyants, I.K. Robinson, J.D. Onken, M.A. Pfeifer, G.J. Williams, F. Pfeiffer, H. Metzger, Z. Zhong, G. Bauer, Coherent X-ray diffraction from quantum dots, Phys. Rev. B 71 (2005) 245302, http://dx.doi.org/10.1103/PhysRevB.71.245302.
[127] J.C.H. Spence, U. Weierstall, M. Howells, Coherence and sampling requirements for diffractive imaging, Ultramicroscopy 101 (2004) 149–152, http://dx.doi.org/10.1016/j.ultramic.2004.05.005.
[128] H.N. Chapman, A. Barty, S. Marchesini, A. Noy, C. Cui, M.R. Howells, R. Rosen, H. He, J.C.H. Spence, U. Weierstall, T. Beetz, C. Jacobsen, D. Shapiro, High-resolution Ab initio three-dimensional X-ray diffraction microscopy, J. Opt. Soc. Am. A. 23 (2006) 1179–1200, http://dx.doi.org/10.1364/JOSAA.23.001179.
[129] S. Marchesini, H.N. Chapman, A. Barty, C. Cui, M.R. Howells, J.C.H. Spence, U. Weierstall, A.M. Minor, Phase aberrations in diffraction microscopy, IPAP Conf. Ser. 7 (2006) 380–382.
[130] J. Rodenburg, A. Hurst, A. Cullis, B. Dobson, F. Pfeiffer, O. Bunk, C. David, K. Jefimovs, I. Johnson, Hard-X-ray lensless imaging of extended objects, Phys. Rev. Lett. 98 (2007) 034801, http://dx.doi.org/10.1103/PhysRevLett.98.034801.
[131] M. Dierolf, A. Menzel, P. Thibault, P. Schneider, C.M. Kewish, R. Wepf, O. Bunk, F. Pfeifer, Ptychographic X-ray computed tomography at the nanoscale, Nature 467 (2010) 436–439, http://dx.doi.org/10.1038/nature09419.
[132] Y. Takahashi, A. Suzuki, N. Zettsu, Y. Kohmura, K. Yamauchi, T. Ishikawa, Multiscale element mapping of buried structures by ptychographic X-ray diffraction microscopy using anomalous scattering, Appl. Phys. Lett. 99 (2011) 131905, http://dx.doi.org/10.1063/1.3644396.
[133] A. Suzuki, S. Furutaku, K. Shimomura, K. Yamauchi, Y. Kohmura, T. Ishikawa, Y. Takahashi, High-resolution multislice X-ray ptychography of extended thick objects, Phys. Rev. Lett. 112 (2014) 053903, http://dx.doi.org/10.1103/PhysRevLett.112.053903.
[134] E. Nazaretski, X. Huang, H. Yan, K. Lauer, R. Conley, N. Bouet, J. Zhou, W. Xu, D. Eom, D. Legnini, R. Harder, C.H. Lin, Y.S. Chen, Y. Hwu, Y.S. Chu, Design and performance of a scanning ptychography microscope, Rev. Sci. Instrum. 85 (2014) 033707, http://dx.doi.org/10.1063/1.4868968.
[135] X. Huang, H. Yan, R. Harder, Y. Hwu, I.K. Robinson, Y.S. Chu, Optimization of overlap uniformness for ptychography, Opt. Express 22 (2014) 12634–12644, http://dx.doi.org/10.1364/OE.22.012634.
[136] C.C. Chien, C.H. Wang, C.L. Wang, E.R. Li, K.H. Lee, Y. Hwu, C.Y. Lin, S.J. Chang, C.S. Yang, C. Petibois, G. Margaritondo, Synchrotron microangiography studies of angiogenesis in mice with microemulsions and gold nanoparticles, Anal. Bioanal. Chem. 397 (2010) 2109–2116, http://dx.doi.org/10.1007/s00216-010-3775-8.
[137] C.C. Chien, H.H. Chen, S.F. Lai, K.C. Wu, X. Cai, Y. Hwu, C. Petibois, Y.S. Chu, G. Margaritondo, Gold nanoparticles as high-resolution X-ray imaging contrast agents for the analysis of tumor-related micro-vasculature, J. Nanobiotechnol. 10 (2012) 10, http://dx.doi.org/10.1186/1477-3155-10-10.
[138] C.C. Chien, I.M. Kempson, C.L. Wang, H.S. Chen, Y. Hwu, N.Y. Chen, T.K. Lee, C. Petibois, K.K.C. Tsai, M.S. Liu, K.Y. Chang, C.S. Yang, G. Margaritondo, Complete microscale profiling of tumor microangiogenesis: A microradiological methodology reveals fundamental aspects of tumor angiogenesis and yields an array of quantitative parameters for its characterization, Biotechnol. Adv. 31 (2013) 396–401, http://dx.doi.org/10.1016/j.biotechadv.2011.12.001.
[139] J.W. Kim, H.S. Seo, Y. Hwu, J.H. Je, A. Kim, C.W. Oh, S.Y. Suh, S.W. Rha, C.G. Park, D.J. Oh, In vivo real-time vessel imaging and ex vivo 3D reconstruction of atherosclerotic plaque in apolipoprotein E-knockout mice using synchrotron radiation microscopy, Int. J. Cardiol. 114 (2007) 166–171, http://dx.doi.org/10.1016/j.ijcard.2005.12.010.
[140] J. Folkman, E. Merler, C. Abernathy, G. Williams, Isolation of a tumor factor responsible for angiogenesis, J. Exp. Med. 133 (1971) 275–288, http://dx.doi.org/10.1084/jem.133.2.275.
[141] R. Kerbel, J. Folkman, Clinical translation of angiogenesis inhibitors, Nat. Rev. Cancer 2 (2002) 727–739, http://dx.doi.org/10.1038/nrc905.
[142] S. Goel, D.G. Duda, L. Xu, L.L. Munn, Y. Boucher, D. Fukumura, R.K. Jain, Normalization of the vasculature for treatment of cancer and other diseases, Physiol. Rev. 91 (2011) 1071–1121, http://dx.doi.org/10.1152/physrev.00038.2010.
[143] J. Holash, P.C. Maisonpierre, D. Compton, P. Boland, C.R. Alexanderd. D. Zagzag, G.D. Yancopoulos, S.J. Wiegand, Vessel cooption, regression, and growth in tumors mediated by angiopoietins and VEGF, Science 284 (1999) 1994–1998, http://dx.doi.org/10.1126/science.284.5422.1994.
[144] C. Wiesmann, G. Fuh, H.W. Christinger, C. Eigenbrot, J.A. Wells, A.M. de Vos, Crystal structure at 1.7 A resolution of VEGF in complex with domain 2 of the flt-1 receptor, Cell 91 (5) (1997) 695, http://dx.doi.org/10.1016/s0092-8674(00)80456-0.
[145] O.L. Chinot, W. Wick, W. Mason, R. Henriksson, F. Saran, R. Nishikawa, A.F. Carpentier, K. Hoang-Xuan, P. Kavan, D. Cernea, A.A. Brandes, M. Hilton, L. Abrey, T. Cloughesy, Bevacizumab plus radiotherapy–temozolomide for newly diagnosed glioblastoma, N. Engl. J. Med. 370 (2014) 709–722, http://dx.doi.org/10.1056/NEJMoa1308345.

[146] G. Auf, A. Jabouille, S. Guerit Gregor Auf, Arnaud Jabouille, Sylvaine Guérit, +12, Raphaël Pineau, Maylis Delugin, Marion Bouchecareilh, Noël Magnin, Alexandre Favereaux, Marlène Maitre, Timo Gaiser, Andreas von Deimling, Marcus Czabanka, Peter Vajkoczy, Eric Chevet, Andreas Bikfalvi, Michel Moenner, Inositol-requiring enzyme 1α is a key regulator of angiogenesis and invasion in malignant glioma, Proc. Natl. Acad. Sci. U S A 107 (2010) 15553–15558, http://dx.doi.org/10.1073/pnas.0914072107.
[147] D. Fukumura, R.K. Jain, Tumor microvasculature and microenvironment: Targets for anti-angiogenesis and normalization, Microvasc. Res. 74 (2007) 72–84, http://dx.doi.org/10.1016/j.mvr.2007.05.003.
[148] S.F. Lai, B.H. Ko, C.C. Chien, C.R. Chang, S.M. Yang, H.H. Chen, C. Petibois, D.Y. Hueng, S.M. Ka, A. Chen, G. Margaritondo, Y. Hwu, Gold nanoparticles as multimodality imaging agents for brain gliomas, J. Nanobiotechnol. 13 (2015) 85, http://dx.doi.org/10.1186/s12951-015-0140-2.
[149] S.F. Lai, C.C. Chien, W.C. Chen, H.H. Chen, Y.Y. Chen, C.L. Wang, Y. Hwu, C.S. Yang, C.Y. Chen, K.S. Liang, C. Petibois, H.R. Tan, E.S. Tok, G. Margaritondo, Very small photoluminescent gold nanoparticles for multimodality biomedical imaging, Biotechnol. Adv. 31 (2013) 362–368, http://dx.doi.org/10.1016/j.biotechadv.2012.05.005.
[150] A. Guevara-Torres, A. Joseph, J.B. Schallek, Label free measurement of retinal blood cell flux, velocity, hematocrit and capillary width in the living mouse eyes, Biomed. Opt. Express 7 (2016) 4228–4249, http://dx.doi.org/10.1364/BOE.7.004228.
[151] A. Li, H. Gong, B. Zhang, Q. Wang, C. Yan, J. Wu, Q. Liu, S. Zeng, Q. Luo, Micro-optical sectioning tomography to obtain a high-resolution Atlas of the mouse brain, Science 330 (2011) 1404–1408, http://dx.doi.org/10.1126/science.1191776.
[152] H. Jung, H.J. Kim, E.K. Kim, J.O. Hong, J.H. Je, Y. Hwu, W.L. Tsai, G. Magaritondo, H.S. Yoo, Comparison of unmonochromatized synchrotron radiation and conventional X-rays in the imaging of mammographic phantom and human breast specimens: A preliminary result, Yonsei Med. J. 46 (2005) 95–103, http://dx.doi.org/10.3349/ymj.2005.46.1.95.
[153] Y. Tong, G. Zhang, Y. Li, Y. Hwu, W. Tsai, J.H. Je, G. Margaritondo, D. Yuan, Synchrotron refractive-index microradiography of human liver cancer tissue, Chin. Sci. Bull. 50 (2005) 2657–2661, http://dx.doi.org/10.1007/BF03183666.
[154] C.Y. Yoon, D.J. Sung, J.H. Lee, A.R. Kim, C.W. Oh, J.H. Je, B.M. Weon, S.K. Seol, A. Pyun, Y. Hwu, G. Margaritondo, K.J. Joo, D.K. Yoon, Imaging of renal and prostate carcinoma with refractive index radiology, Int. J. Urol. 14 (2007) 96–103, http://dx.doi.org/10.1111/j.1442-2042.2007.01614.x.
[155] C.C. Chien, G. Zhang, Y. Hwu, P. Liu, W. Yue, J. Sun, Y. Li, H.J. Xue, X. Xu, C.H. Wang, N.Y. Chen, C.H. Lu, T.K. Lee, Y.C. Yang, Y.T. Lu, Y.T. Ching, P.C. Yang, J.H. Je, G. Margaritondo, Detecting small lung tumors in mouse models by refractive-index microradiology, Anal. Bioanal. Chem. 401 (2011) 827–835, http://dx.doi.org/10.1007/s00216-011-5117-x.
[156] H.J. Lee, J.H. Je, Y. Hwu, W.L. Tsai, Synchrotron X-ray induced solution precipitation of nanoparticles, Nucl. Instrum. Meth. B 199 (2003) 342–347, http://dx.doi.org/10.1016/S0168-583X(02)01561-6.
[157] Y.C. Yang, C.H. Wang, Y.K. Hwu, J.H. Je, Synchrotron X-ray synthesis of colloidal gold particles for drug delivery, Mater. Chem. Phys. 100 (2006) 72–76, http://dx.doi.org/10.1016/j.matchemphys.2005.12.007.
[158] N. Baig, I. Kammakakam, W. Falath, Nanomaterials: A review of synthesis methods, properties, recent progress, and challenges, Mater. Adv. 2 (2021) 1821, http://dx.doi.org/10.1039/d0ma00807a.
[159] S. Anu Mary Ealia, M.P. Saravanakumar, A review on the classification, characterisation, synthesis of nanoparticles and their application, IOP Conf. Ser. Mater. Sci. Eng. 263 (2017) 032019, http://dx.doi.org/10.1088/1757-899X/263/3/032019.
[160] J.H. Huang, H.J. Parab, R.S. Liu, T.C. Lai, M. Hsiao, C.H. Chen, H.S. Sheu, J.M. Chen, D.P. Tsai, Y.K. Hwu, Investigation of the growth mechanism of iron oxide nanoparticles via a seed-mediated method and its cytotoxicity studies, J. Phys. Chem. C 112 (2008) 15684–15690, http://dx.doi.org/10.1021/jp803452j.
[161] C.H. Wang, T.E. Hua, C.C. Chien, Y.L. Yu, T.Y. Yang, C.J. Liu, W.H. Leng, Y. Hwu, Y.C. Yang, C.C. Kim, J.H. Je, C.H. Chen, H.M. Lin, G. Margaritondo, Aqueous gold nanosols stabilized by electrostatic protection generated by X-ray irradiation assisted radical reduction, Mater. Chem. Phys. 106 (2007) 323–329, http://dx.doi.org/10.1016/j.matchemphys.2007.06.024.
[162] C.H. Wang, C.J. Liu, C.L. Wang, T.E. Hua, J.M. Obliosca, K.H. Lee, Y. Hwu, C.S. Yang, R.S. Liu, H.M. Lin, J.H. Je, G. Margaritondo, Optimizing the size and surface properties of polyethylene glycol (PEG)–gold nanoparticles by intense X-ray irradiation, J. Phys. D: Appl. Phys. 41 (2008) 195301, http://dx.doi.org/10.1088/0022-3727/41/19/195301.
[163] S.F. Lai, C.C. Chien, W.C. Chen, Y.Y. Chen, C. Wang, Y. Hwu, C.S. Yang, G. Margaritondo, Size control of gold nanoparticles by intense X-ray irradiation: The relevant parameters and imaging applications, RSC Adv. 2 (2012) 6185–6191, http://dx.doi.org/10.1039/C2RA20260C.
[164] S.F. Lai, W.C. Chen, C.L. Wang, H.H. Chen, S.T. Chen, C.C. Chien, Y.Y. Chen, W.T. Hung, X. Cai, E. Li, I.M. Kempson, Y. Hwu, C.S. Yang, E.S. Tok, H.R. Tan, M. Lin, G. Margaritondo, One-pot tuning of Au nucleation and growth: From nanoclusters to nanoparticles, Langmuir 27 (2011) 8424–8429, http://dx.doi.org/10.1021/la200861e.
[165] M.T. Li, S.F. Lai, S.M. Yang, Y.S. Chen, Y.J. Chen, E.S. Tok, G. Margaritondo, Y. Hwu, Gold nano-mesh synthesis by continuous-flow X-ray irradiation, J. Synchrotron Radiat. 26 (2019) 1929–1935, http://dx.doi.org/10.1107/S1600577519011834.
[166] C.C. Chien, H.H. Chen, S.F. Lai, Y. Hwu, C. Petibois, Y.S. Yang, Y. Chu, G. Margaritondo, X-ray imaging of tumor growth in live mice by detecting gold-nanoparticle-loaded cells, Sci. Rep. 2 (2012) 610, http://dx.doi.org/10.1038/srep00610.
[167] I.M. Kempson, C.C. Chien, C.Y. Chung, Y. Hwu, D. Paterson, M.D. de Jonge, D.L. Howard, Fate of intravenously administered gold nanoparticles in hair follicles: Follicular delivery, pharmacokinetic interpretation, and excretion, Adv. Healthc. Mater. 1 (2012) 736–741, http://dx.doi.org/10.1002/adhm.2012001011.
[168] C.L. Chen, L.R. Kuo, S.Y. Lee, Y.K. Hwu, S.W. Chou, C.C. Chen, F.H. Chang, K.H. Lin, D.H. Tsai, Y.Y. Chen, Photothermal cancer therapy via femtosecond-laser-excited FePt nanoparticles, Biomaterials 34 (2013) 1128–1134.
[169] C.P. Liu, F.S. Lin, C.T. Chien, S.Y. Tseng, C.W. Luo, C.H. Chen, J.K. Chen, F.G. Tseng, Y. Hwu, L.W. Lo, C.S. Yang, S.Y. Lin, In-situ formation and assembly of gold nanoparticles by gum Arabic as efficient photothermal agent for killing cancer cells, Macromol. Biosci. 13 (2013) 1314–1320, http://dx.doi.org/10.1002/mabi.201300162.
[170] Y.C. Huang, Y.C. Yang, K.C. Yang, H.R. Shieh, T.Y. Wang, Y. Hwu, Y.J. Chen, Pegylated gold nanoparticles induce apoptosis in human chronic myeloid leukemia cells, BioMed. Res. Int. 2014 (2014) 182353, http://dx.doi.org/10.1155/2014/182353.
[171] F.S. Lin, C.H. Chen, F.G. Tseng, Y. Hwu, J.K. Chen, S.Y. Lin, Y.S. Yang, Radiotherapy of the excretable radioactive gold nanocomposite with intratumoral injection, Int. J. Mater. Mech. Manuf. 1 (2013) 265–268, http://dx.doi.org/10.7763/IJMMM.2013.V1.56.
[172] F.K. Huang, W.C. Chen, S.F. Lai, C.J. Liu, C.L. Wang, C.H. Wang, H.H. Chen, T.E. Hua, Y.Y. Chen, M.K. Wu, Y. Hwu, C.S. Yang, G. Margaritondo, Enhancement of irradiation effects on cancer cells by cross-linked dextran-coated iron oxide (CLIO) nanoparticles, Phys. Med. Biol. 55 (2010) 469–482, http://dx.doi.org/10.1088/0031-9155/55/2/009.
[173] P.K. Jain, K.S. Lee, I.H. El-Sayed, M.A. El-Sayed, Calculated absorption and scattering properties of gold nanoparticles of different size, shape, and composition: Applications in biological imaging and biomedicine, J. Phys. Chem. B 110 (2006) 7238–7248, http://dx.doi.org/10.1021/jp057170o.
[174] X. Cai, C.L. Wang, H.H. Chen, C.C. Chien, S.F. eng Lai, Y.Y. Chen, T.E. Hua, I.M. Kempson, Y. Hwu, C.S. Yang, G. Margaritondo, Tailored Au nanorods: Optimizing functionality, controlling the aspect ratio and increasing biocompatibility, Nanotechnology 21 (2010) 335604, http://dx.doi.org/10.1088/0957-4484/21/33/335604.
[175] C.C. Chien, C.C. Cheng, H.H. Chen, Y. Hwu, Y.S. Chu, C. Petibois, A. Chen, Y.T. Ching, G. Margaritondo, X-ray microscopy and tomography detect the accumulation of bare and PEG-coated gold nanoparticles in normal and tumor mouse tissues, Anal. Bioanal. Chem. 404 (2012) 1287–1296, http://dx.doi.org/10.1007/s00216-012-6217-y.

[176] C.H. Wang, C.C. Chien, Y.L. Yu, C.J. Liu, C.F. Lee, C.H. Chen, Y. Hwu, C.S. Yang, J.H. Je, G. Margaritondo, Structural properties of 'naked' gold nanoparticles formed by synchrotron X-ray irradiation, J. Synchrotron Radiat. 14 (2007) 477–482, http://dx.doi.org/10.1107/S0909049507044743.
[177] K.H. Lee, S.F. Lai, Y.C. Lin, W.C. Chou, E.B.L. Ong, H.R. Tan, E.S. Tok, C.S. Yang, G. Margaritondo, Y. Hwu, Gold nanoparticles: BSA (bovine serum albumin) coating and X-ray irradiation produce variable-spectrum photoluminescence, Mater. Chem. Phys. 149–150 (2015) 582–586, http://dx.doi.org/10.1016/j.matchemphys.2014.11.009.
[178] S.F. Lai, H.R. Tan, E.S. Tok, Y.H. Chen, E.B.L. Ong, M.T. Li, Y.Y. Chen, F.C. Chien, P. Chen, G. Margaritondo, Y. Hwu, Optimization of gold nanoparticle photoluminescence by alkanethiolation, Chem. Commun. 51 (2015) 7954–7957, http://dx.doi.org/10.1039/c5cc01229e.
[179] Y.F. Song, C.H. Chang, C.Y. Liu, S.H. Chang, U.S. Jeng, Y.H. Lai, D.G. Liu, S.C. Chung, K.L. Tsang, G.C. Yin, J.F. Lee, H.S. Sheu, M.T. Tang, C.S. Hwang, Y. Hwu, K.S. Liang, X-ray beamlines for structural studies at the NSRRC superconducting wavelength shifter, J Synchrotron Radiat. 14 (2007) 320–325, http://dx.doi.org/10.1107/S0909049507021516.
[180] M.C. Garcia Toro, J.P. Schlegel, C.H. Castano Giraldo, Direct synthesis of radioactive gold nanoparticles using a research nuclear reactor, J. Nucl. Med. Technol. 46 (2018) 280–284, http://dx.doi.org/10.2967/jnmt.117.206367.
[181] C.H. Chen, F.S. Lin, W.N. Liao, S.L. Liang, M.H. Chen, Y.W. Chen, W.Y. Lin, M.H. Hsu, M.Y. Wang, J.J. Peir, F.I. Chou, C.Y. Chen, S.Y. Chen, S.C. Huang, M.H. Yang, D.Y. Hueng, Y. Hwu, C.S. Yang, J.K. Chen, Establishment of a trimodality analytical platform for tracing, imaging and quantification of gold nanoparticles in animals by radiotracer techniques, Anal. Chem. 87 (1) (2015) 601–608, http://dx.doi.org/10.1021/ac503260f.
[182] B.M. Weon, J.H. Je, Y. Hwu, G. Margaritondo, Decreased surface tension of water by hard-X-ray irradiation, Phys. Rev. Lett. 100 (2008) 217403, http://dx.doi.org/10.1103/PhysRevLett.100.217403.
[183] J.T. Kim, S.K. Seol, J.H. Je, Y. Hwu, G. Margaritondo, The microcontainer shape in electropolymerization on bubbles, Appl. Phys. Lett. 94 (2009) 034103, http://dx.doi.org/10.1063/1.3073861.
[184] P.C. Hsu, S.K. Seol, T.N. Lo, C.J. Liu, C.L. Wang, C.S. Lin, Y. Hwu, C.H. Chen, L.W. Chang, J.H. Je, G. Margaritondo, Hydrogen bubbles and the growth morphology of ramified zinc by electrodeposition, J. Electrochemical Soc. 155 (2008) D400–D407, http://dx.doi.org/10.1149/1.2894189.
[185] W.L. Tsai, P.C. Hsu, Y. Hwu, C.H. Chen, L.W. Chang, H.M. Lin, J.H. Je, A. Groso, G. Margaritondo, Building on bubbles in metal electrodeposition, Nature 417 (2002) 139, http://dx.doi.org/10.1038/417139a.
[186] S.K. Seol, A.R. Pyun, Y.K. Hwu, G. Margaritondo, J.H. Je, Localized electrochemical deposition of copper monitored using real-time X-ray microradiography, Adv. Funct. Mater. 15 (2005) 934–937, http://dx.doi.org/10.1002/adfm.200400514.
[187] A.M. Worthington, On impact with a liquid surface, Proc. R. Soc. London 34 (1883) 217–230, http://dx.doi.org/10.1098/rspl.1882.0035.
[188] K. Fezzaa, Y. Wang, Ultrafast X-ray phase-contrast imaging of the initial coalescence phase of two water droplets, Phys. Rev. Lett. 100 (2008) 104501, http://dx.doi.org/10.1103/PhysRevLett.100.104501.
[189] J.S. Lee, B.M. Weon, J.H. Je, K. Fezzaa, How does an air film evolve into a bubble during drop impact? Phys. Rev. Lett. 109 (2012) 204501, http://dx.doi.org/10.1103/PhysRevLett.109.204501.
[190] S.T. Thoroddsen, T.G. Etoh, K. Takehara, N. Ootsuka, Y. Hatsuki, The air bubble entrapped under a drop impacting on a solid surface, J. Fluid Mech. 545 (2005) 203–212, http://dx.doi.org/10.1017/S0022112005006919.
[191] J.S. Lee, B.M. Weon, S.J. Park, J. Ta Kim, J. Pyo, K. Fezzaa, J.H. Je, Air evolution during drop impact on liquid pool, Sci. Rept. 10 (2020) 5790, http://dx.doi.org/10.1038/s41598-020-62705-5.
[192] S. Dorbolo, H. Caps, N. Vandewalle, Fluid instabilities in the birth and death of antibubbles, New J. Phys 5 (2003) 161, http://dx.doi.org/10.1088/1367-2630/5/1/161.
[193] D. Bartolo, C. Josserand, D. Bonn, Retraction dynamics of aqueous drops upon impact on non-wetting surfaces, J. Fluid Mech. 545 (2005) 329–338, http://dx.doi.org/10.1017/S0022112005007184.
[194] J. Eggers, M.S. Fontelos, C. Josserand, S. Zaleski, Drop dynamics after impact on a solid wall: Theory and simulations, Phys. Fluids 22 (2010) 062101, http://dx.doi.org/10.1063/1.3432498.
[195] S. Kooij, A.M. Moqaddam, T.C. de Goede, D. Derome, J. Carmeliet, N. Shahidzadeh, D. Bonn, Sprays from droplets impacting a mesh, J. Fluid Mech. 871 (2019) 489–509, http://dx.doi.org/10.1017/jfm.2019.289.
[196] T. Paunesku, S. Vogt, J. Maser, B. Lai, G. Woloschak, X-ray fluorescence microprobe imaging in biology and medicine, J. Cell. Biochem. 99 (2006) 1489–1502, http://dx.doi.org/10.1002/jcb.21047.
[197] J.A. Howe, R.H. Loeppert, V.J. DeRose, D.B. Hunter, P.M. Bertsch, Localization and speciation of chromium in subterranean clover using XRF, XANES, and EPR spectroscopy, Environ. Sci. Techno. 37 (2003) 4091–4097, http://dx.doi.org/10.1021/es034156l.
[198] N.K. Blute, D.J. Brabander, H.F. Hemond, S.R. Sutton, M.G. Newville, Rivers. M.L., Arsenic sequestration by ferric iron plaque on cattail roots, Environ. Sci. Technol. 38 (2004) 6074–6077, http://dx.doi.org/10.1021/es049448g.
[199] B. Qian, H. Shen, W. Liang, X. Guo, C. Zhang, Y. Wang, G. Li, A. Wu, K. Cao, D. Zhang, Immunogenicity of recombinant hepatitis B virus surface antigen fused with preS1 epitopes expressed in rice seeds, Transgenic Res. 17 (2008) 621–631, http://dx.doi.org/10.1007/s11248-007-9135-6.
[200] Z. Liu, B. Liu, J. Hu, H. An, B. Gong, M. Li, Y. He, X. Gao, L. Bi, H. Li, Y. Pang, P. Zhao, (unpublished data).
[201] A.P. Bonto, R.N. Tiozon Jr., C. Rojviriya, N. Sreenivasulu, D.H. Camacho, Sonication increases the porosity of uncooked rice kernels affording softer textural properties, loss of intrinsic nutrients and increased uptake capacity during fortification, Ultrason. Sonochem. 68 (2020) 105234, http://dx.doi.org/10.1016/j.ultsonch.2020.105234.
[202] J.P. Lin, A.C. Scott, C.W. Li, H.J. Wu, W.I. Ausich, Y.L. Zhao, Y.K. Hwu, Silicified egg clusters from a middle Cambrian Burgess Shale–type deposit, Guizhou, South China, Geology 34 (2006) 1037–1040, http://dx.doi.org/10.1130/B23006A.1.
[203] J.Y. Chen, D.J. Bottjer, E.H. Davidson, S.Q. Dornbos, X. Gao, Y.H. Yang, C.W. Li, G. Li, X.Q. Wang, D.C. Xian, H.J. Wu, Y.K. Hwu, P. Tafforeau, Phosphatized polar-lobe-forming embryos from the Precambrian of Southwest China, Science 312 (2006) 1644–1646, http://dx.doi.org/10.1126/science.1125964.
[204] J.Y. Chen, D.J. Bottjer, P. Oliveri, S.Q. Dornbos, F. Gao, S. Ruffins, H. Chi, C.W. Li, E.H. Davidson, Small bilaterian fossils from 40 to 55 million years before the Cambrian, Science 305 (2004) 218–222, http://dx.doi.org/10.1126/science.1099213.
[205] J.-Y. Chen, The Dawn of Animal World, Publishing House of Jiangsu Science & Technology, Nanjing, 2004.
[206] Z.X. Luo, Doushantuo fossils: Life on the eve of animal radiation, J. Paleontol. 79 (2005) 1040–1042, http://dx.doi.org/10.1666/0022-3360(2005)079[1040:R]2.0.CO;2.
[207] D. Condon, M. Zhu, S. Bowring, W. Wang, A. Yang, Y. Jin, U-Pb ages from the neoproterozoic Doushantuo formation, China, Science 308 (2005) 95–98, http://dx.doi.org/10.1126/science.1107765.
[208] G.H. Barfod, F. Albarède, A.H. Knoll, S. Xiao, Philippe Télouk, R. Frei, J. Baker, New Lu–Hf and Pb–Pb age constraints on the earliest animal fossils, Earth Planet. Sci. Lett. 201 (2002) 203–212, http://dx.doi.org/10.1016/S0012-821X(02)00687-8.
[209] D.B. Conn, Atlas of Invertebrate Reproduction and Development, second ed., Wiley, Hoboken, NJ, 2000.
[210] S.F. Gilbert, A.M. Raunio (Eds.), Embryology: Constructing the Organism, Sinauer, Sunderland, MA, 1997.
[211] F. Albertin, A. Astolfo, M. Stampanoni, E. Peccenini, Y. Hwu, F. Kaplan, G. Margaritondo, X-ray spectrometry and imaging for ancient administrative handwritten documents, X-Ray Spectrom. 44 (2015) 93–98, http://dx.doi.org/10.1002/xrs.2581.
[212] F. Albertin, A. Astolfo, M. Stampanoni, E. Peccenini, Y. Hwu, F. Kaplan, G. Margaritondo, Ancient administrative handwritten documents: X-ray analysis and imaging, J. Synchrotron Radiat. 22 (2015) 446–451, http://dx.doi.org/10.1107/S1600577515000314.

[213] F. Albertin, A. Patera, I. Jerjen, S. Hartmann, E. Peccenini, F. Kaplan, M. Stampanoni, R. Kaufmann, G. Margaritondo, Virtual reading of a large ancient handwritten science book, Microchem. J. 125 (2016) 185–189, http://dx.doi.org/10.1016/j.microc.2015.11.024.
[214] F. Albertin, E. Peccenini, Y. Hwu, T.T. Lee, E.B.L. Ong, J.H. Je, F. Kaplan, G. Margaritondo, The Venice Archivio Di Stato: Innovating digitization with X-ray tomography, 2015 Digital Heritage (2015) 5–10, http://dx.doi.org/10.1109/DigitalHeritage.2015.7413825.
[215] O. Sporns, G. Tononi, R. Kötter, The human connectome: A structural description of the human brain, PLOS Comput. Biol. 1 (2005) e42, http://dx.doi.org/10.1371/journal.pcbi.0010042.
[216] S. Jbabdi, H. Johansen-Berg, Tractography: Where do we go from here? Brain Connect 1 (2011) 169–183, http://dx.doi.org/10.1089/brain.2011.0033.
[217] E. Macé, G. Montaldo, I. Cohen, M. Baulac, M. Fink, M. Tanter, Functional ultrasound imaging of the brain, Nature Methods 8 (2011) 662–664, http://dx.doi.org/10.1038/nmeth.1641.
[218] K. Amunts, C. Lepage, L. Borgeat, H. Mohlberg, T. Dickscheid, M.-É. Rousseau, S. Bludau, P.L. Bazin, L.B. Lewis, A.-M. Oros-Peusquens, N.J. Shah, T. Lippert, K. Zilles, A.C. Evans, BigBrain: An ultrahigh-resolution 3D human brain model, Science 340 (2013) 1472–1475, http://dx.doi.org/10.1126/science.1235381.
[219] S.W. Oh, J.A. Harris, L. Ng, B. Winslow, N. Cain, S. Mihalas, Q. Wang, C. Lau, L. Kuan, A.M. Henry, M.T. Mortrud, B. Ouellette, T.N. Nguyen, S.A. Sorensen, C.R. Slaughterbeck, W. Wakeman, Y. Li, D. Feng, A. Ho, E. Nicholas, K.E. Hirokawa, P. Bohn, K.M. Joines, H. Peng, M.J. Hawrylycz, J.W. Phillips, J.G. Hohmann, C.R. Gerfen, P. Wohnoutka, C. Koch, A. Bernard, C. Dang, A.R. Jones, H. Zeng, A mesoscale connectome of the mouse brain, Nature 508 (2014) 207–214, http://dx.doi.org/10.1038/nature13186.
[220] N. Kasthuri, K.J. Hayworth, D.R. Berger, R.L. Schalek, J.A. Conchello, S. Knowles-Barley, D. Lee, A. Vázquez-Reina, V. Kaynig, T.R. Jones, M. Roberts, J.L. Morgan, J.C. Tapia, H.S. Seung, W.G. Roncal, J.T. Vogelstein, R. Burns, D.L. Sussman, C.E. Priebe, H. Pfister, J.W. Lichtman, Saturated reconstruction of a volume of neocortex, Cell 162 (2015) 648–661, http://dx.doi.org/10.1016/j.cell.2015.06.054.
[221] M.F. Glasser, T.S. Coalson, E.C. Robinson, C.D. Hacker, J. Harwell, E. Yacoub, K. Ugurbil, J. Andersson, C.F. Beckmann, M. Jenkinson, S.M. Smith, D.C. Van Essen, A multi-modal parcellation of human cerebral cortex, Nature 536 (2016) 171–178, http://dx.doi.org/10.1038/nature18933.
[222] C.C. Lo, A.S. Chiang, Toward whole-body connectomics, J. Neurosci. 36 (2016) 11375–11383, http://dx.doi.org/10.1523/JNEUROSCI.2930-16.2016.
[223] L.A. Chu, C.H. Lu, Y.S. Yang, Y.T. Liu, K.L. Feng, Y.C. Tsai, W.K. Chang, W.C. Wang, S.W. Chang, P. Chen, T.K. Lee, Y.K. Hwu, A.S. Chiang, B.C. Chen, Rapid single-wavelength lightsheet localization microscopy for clarified tissue, Nature Commun. 10 (2019) 4762, http://dx.doi.org/10.1038/s41467-019-12715-3.
[224] C.H. Lu, W.C. Tang, Y.T. Liu, S.W. Chang, F.C.M. Wu, C.Y. Chen, Y.C. Tsai, S.M. Yang, C.W. Kuo, Y. Okada, Y.K. Hwu, P. Chen, B.C. Chen, Lightsheet localization microscopy enables fast, large-scale, and three-dimensional super-resolution imaging, Commun. Biol. 2 (2019) 177, http://dx.doi.org/10.1038/s42003-019-0403-9.
[225] R. Gao, S.M. Asano, S. Upadhyayula, I. Pisarev, D.E. Milkie, T.L. Liu, V. Singh, A. Graves, G.H. Huynh, Y. Zhao, J. Bogovic, J. Colonell, C.M. Ott, C. Zugates, S. Tappan, A. Rodriguez, K.R. Mosaliganti, S.H. Sheu, H.A. Pasolli, S. Pang, C.S. Xu, S.G. Megason, H. Hess, J. Lippincott-Schwartz, A. Hantman, G.M. Rubin, T. Kirchhausen, S. Saalfeld, Y. Aso, E.S. Boyden, E. Betzig, Cortical column and whole-brain imaging with molecular contrast and nanoscale resolution, Science 363 (2019) eaau8302, http://dx.doi.org/10.1126/science.aau8302.
[226] S.Y. Takemura, Y. Aso, T. Hige, A. Wong, Z. Lu, C.S. Xu, P.K. Rivlin, H. Hess, T. Zhao, T. Parag, S. Berg, G. Huang, W. Katz, D.J. Olbris, S. Plaza, L. Umayam, R. Aniceto, L.A. Chang, S. Lauchie, O. Ogundeyi, C. Ordish, A. Shinomiya, C. Sigmund, S. Takemura, J. Tran, G.C. Turner, G.M. Rubin, L.K. Scheffer, A connectome of a learning and memory center in the adult drosophila brain, Elife 6 (2017) e26975, http://dx.doi.org/10.7554/eLife.26975.
[227] T.M. Buzug, Computed Tomography: From Photon Statistics To Modern Conebeam CT, Springer-Verlag, Berlin, Heidelberg, 2008.
[228] J.L. Morgan, J.W. Lichtman, Why not connectomics? Nat. Methods 10 (2013) 494–500, http://dx.doi.org/10.1038/nmeth.2480.
[229] Human Brain Project. https://www.humanbrainproject.eu/.
[230] Y. Kohmura, S.M. Yang, H.H. Chen, H. Takano, C.J. Chang, Y.S. Wang, T.T. Lee, C.Y. Chiu, K.E. Yang, Y.T. Chien, H.M. Hu, T.L. Su, C. Petibois, Y.Y. Chen, C.H. Hsu, P. Chen, D.Y. Hueng, S.J. Chen, C.L. Yang, A.L. Chin, C.M. Low, F.C.K. Tan, A. Teo, E.S. Tok, X.X. Cai, H.M. Lin, J. Boeckl, A.P. Stampfl, J. Yamada, S. Matsuyama, T. Ishikawa, G. Margaritondo, A.S. Chiang, Y. Hwu, The new X-ray/visible microscopy MAXWELL technique for fast three-dimensional nanoimaging with isotropic resolution, Sci. Rep. 12 (2022) 9668, http://dx.doi.org/10.1038/s41598-022-13377-w.
[231] SYNAPSE inauguration, 2020, https://synapse-sg.org/, (Accessed 23 June 2022).
[232] SYNAPSE external experts: Adriano Aguzzi, Moo-Ming Poo, Ann-Shyn Chiang, Hollis Cline.
[233] Y. Hwu, G. Margaritondo, A.S. Chiang, Q & A: Why use synchrotron X-ray tomography for multi-scale connectome mapping? BMC Biol. 15 (2017) 122, http://dx.doi.org/10.1186/s12915-017-0461-8.
[234] H.H. Chen, S.M. Yang, K.E. Yang, C.Y. Chiu, C.J. Chang, Y.S. Wang, T.T. Lee, Y.F. Huang, Y.Y. Chen, C. Petibois, S.H. Chang, X. Cai, C.M. Low, F.C.K. Tan, A. Teo, E.S. Tok, J.H. Lim, J.H. Je, Y. Kohmura, T. Ishikawa, G. Margaritondo, Y. Hwu, High-resolution fast tomography brain imaging beamline at the Taiwan photon source, J. Synchrotron Radiat. 28 (2021) 1662–1668, http://dx.doi.org/10.1107/S1600577521007633.
[235] Y. Lau, U. Hampel, M. Schubert, Ultrafast X-ray tomographic imaging of multiphase flow in bubble columns-part 1: Image processing and reconstruction comparison, Int. J. Multiph. Flow 104 (2018) 258–271, http://dx.doi.org/10.1016/j.ijmultiphaseflow.2018.02.010.
[236] A.L. Chin, S.M. Yang, H.H. Chen, M.T. Li, T.T. Lee, Y.J. Chen, T.K. Lee, C. Petibois, X. Cai, C.M. Low, F.C.K. Tan, A. Teo, E.S. Tok, E.B.L. Ong, Y.Y. Lin, I.J. Lin, Y.C. Tseng, N.Y. Chen, C.T. Shih, J.H. Lim, J.L., J.H. Je, Y. Kohmura, T. Ishikawa, G. Margaritondo, A.S. Chiang, Y. Hwu, A synchrotron X-ray imaging strategy to map large animal brains, Chin. J. Phys. 65 (2020) 24–32, http://dx.doi.org/10.1016/j.cjph.2020.01.010.
[237] C.C. Cheng, Y.T. Ching, P.H. Ko, Y. Hwu, Correction of center of rotation and projection angle in synchrotron X-ray computed tomography, Sci. Rep. 8 (2018) 9884, http://dx.doi.org/10.1038/s41598-018-28149-8.
[238] C.C. Cheng, C.C. Chien, H.H. Chen, Y. Hwu, Y.T. Ching, Image alignment for tomography reconstruction from synchrotron X-ray microscopic images, PLoS One 9 (2014) e84675, http://dx.doi.org/10.1371/journal.pone.0084675.
[239] C. Golgi, Sulla struttura della sostanza grigia del cervelo, Gazz. Med. Ital. (Lombardia) 33 (1873) 244–246.
[240] C. Nicholson, E. Syková, Extracellular space structure revealed by diffusion analysis, Trends Neurosci. 21 (1998) 207–215, http://dx.doi.org/10.1016/s0166-2236(98)01261-2.
[241] S. Ramon, y. Cajal, The Croonian lecture.—La fine structure des centres nerveux, Proc. R. Soc. Lond. 55 (1894) 444–468, http://dx.doi.org/10.1098/rspl.1894.0063.
[242] E. Pannese, The Golgi stain: Invention, diffusion and impact on neurosciences, J. Hist. Neurosci. 8 (1999) 132–140, http://dx.doi.org/10.1076/jhin.8.2.132.1847.
[243] J. Špaček, Dynamics of Golgi method: A time-lapse study of the early stages of impregnation in single sections, J. Neurocytol. 18 (1989) 27–38, http://dx.doi.org/10.1007/BF01188421.
[244] N.J. Strausfeld, The Golgi method: Its application to the insect nervous system and the phenomenon of stochastic impregnation, in: N.J. Strausfeld, T.A. Miller (Eds.), Neuroanatomical Techniques, in: Springer Series in Experimental Entomology, Springer, New York, 1980, pp. 131–203, http://dx.doi.org/10.1007/978-1-4612-6018-9_91980.
[245] J.A. Angulo, B.S. McEwen, Molecular aspects of neuropeptide regulation and function in the corpus striatum and nucleus accumbens, Brain Res. Rev. 19 (1994) 1–28, http://dx.doi.org/10.1016/0165-0173(94)90002-7.

[246] S. Chen, A.E. Goode, J.N. Skepper, A.J. Thorley, J.M. Seiffert, K.F. Chung, T.D. Tetley, M.S.P. Shaffer, M.P. Ryan, A.E. Porter, Avoiding artefacts during electron microscopy of silver nanomaterials exposed to biological environments, J. Microsc. 261 (2016) 157–166, http://dx.doi.org/10.1111/jmi.12215.
[247] E.G. Bertram, H.K. Ihrig, Improvement of the Golgi method by pH control, Stain Technol. 32 (1957) 87–94, http://dx.doi.org/10.3109/10520295709111408.
[248] G. Rosoklija, B. Mancevski, B. Ilievski, T. Perera, S.H. Lisanby, J.D. Coplan, A. Duma, T. Serafimova, A.J. Dwork, Optimization of Golgi methods for impregnation of brain tissue from humans and monkeys, J. Neurosci. Methods 131 (2003) 1–7, http://dx.doi.org/10.1016/j.jneumeth.2003.06.001.
[249] H.W. Kang, H.K. Kim, B.H. Moon, S.J. Lee, S.J. Lee, I.J. Rhyu, Comprehensive review of Golgi staining methods for nervous tissue, Appl. Microsc. 47 (2017) 63–69, http://dx.doi.org/10.9729/AM.2017.47.2.63.
[250] A.S. Chiang, C.Y. Lin, C.C. Chuang, H.M. Chang, C.H. Hsieh, C.W. Yeh, C.T. Shih, J.J. Wu, G.T. Wang, Y.C. Chen, C.C. Wu, G.Y. Chen, Y.T. Ching, P.C. Lee, C.Y. Lin, H.H. Lin, C.C. Wu, H.W. Hsu, Y.A. Huang, J.Y. Chen, H.J. Chiang, C.F. Lu, R.F. Ni, C.Y. Yeh, J.K. Hwang, Three dimensional reconstruction of brain-wide wiring networks in drosophila at single-cell resolution, Curr. Biol. 21 (2011) 1–11, http://dx.doi.org/10.1016/j.cub.2010.11.056.
[251] R. Gao, S.M. Asano, E.S. Boyden, Q & A: Expansion microscopy, BMC Biol. 15 (2017) 50, http://dx.doi.org/10.1186/s12915-017-0393-3.
[252] A.S. Chiang, Y.-C. Liu, S.-L. Chiu, S.-H. Hu, C.-Y. Huang, C.-H. Hsieh, Three-dimensional mapping of brain neuropils in the cockroach, *Diploptera Punctata*, J. Comp. Neurol. 440 (2001) 1–11, http://dx.doi.org/10.1002/cne.1365.
[253] Q. Tang, X. Cai, J. Li, Y. Zhu, L. Wang, C. Fan, J. Hu, Optimization of Golgi-staining methods for X-ray imaging based connectomics. (Unpublished data).
[254] Y. Koyama, M. Tohyama, A modified and highly sensitive Golgi–Cox method to enable complete and stable impregnation of embryonic neurons, J. Neurosci. Methods 209 (2012) 58–61, http://dx.doi.org/10.1016/j.jneumeth.2012.06.007.
[255] E. Ramón-Moliner, The Golgi-Cox technique, in: W.J.H. Nauta, S.O.E. Ebbesson (Eds.), Contemporary Research Methods in Neuroanatomy, Springer, Berlin, Heidelberg, 1970, pp. 32–55, http://dx.doi.org/10.1007/978-3-642-85986-1_3.
[256] J.F. Pasternak, T.A. Woolsey, On the selectivity of the Golgi-Cox method, J. Comp. Neur. 160 (1975) 307–312.
[257] J.F. Hainfeld, R.N. Eisen, R.R. Tubbs, R.D. Powell, Enzymatic metallography: A simple new staining method, in: E. Voekl, D. Piston, R. Gauvin, A.J. Lockley, G.W. Bailey, S. McKernan (Eds.), Microsc. Microanal. 8, (Suppl. 2: Proceedings) (Proceedings of Microscopy and Microanalysis 2002), Cambridge University Press, New York, NY, 2002, p. 916CD.
[258] H. Kong, J. Zhang, J. Li, J. Wang, H.-J. Shin, R. Tai, Q. Yan, K. Xia, J. Hu, L. Wang, Y. Zhu, C. Fan, Genetically encoded X-ray cellular imaging for nanoscale protein localization, Natl. Sci. Rev. 7 (2020) 1218–1227, http://dx.doi.org/10.1093/nsr/nwaa055.
[259] F. Nissl, Ueber eine neue untersuchungsmethode des centralorgans zur feststellung der localisation der nervenzellen, Neurologisches Centralblatt 13 (1894) 507–508.
[260] N. Pilati, M. Barker, S. Panteleimonitis, R. Donga, M. Hamann, A rapid method combining Golgi and Nissl staining to study neuronal morphology and cytoarchitecture, J. Histochem. Cytochem. 56 (2008) 539–550, http://dx.doi.org/10.1369/jhc.2008.950246.
[261] D.A. Sholl, Dendritic organization in the neurons of the visual and motor cortices of the cat, J. Anat. 87 (1953) 387–406.
[262] Unpublished data from C.M. Low, F.C.K. Tan, A. Teo, E.S. Tok, C. Libedinsky, with no participation of other authors of the present article. Their research was exclusively supported by the National University of Singapore (NUS). Two male adult macaques (Macaca fascicularis) brains were obtained through tissue sharing program approved by NUS Institutional Animal Care and Use Committee (SingHealth IACUC#2015/SHS/1055). Procedures also conformed to the recommendations described in Guidelines for the Care and Use of Mammals in Neuroscience and Behavioral Research (National Academies Press 2003);
A. Parthasarathy, R. Herikstad, J.H. Bong, F.S. Medina, C. Libedinsky, S.C. Yen, Mixed selectivity morphs population codes in prefrontal cortex, Nat. Neurosci. 20 (2017) 1770-1779, http://dx.doi.org/10.1038/s41593-017-0003-2.
[263] A. Ogunleke, B. Recur, H. Balacey, H.H. Chen, M. Delugin, Y. Hwu, S. Javerzat, C. Petibois, 3D chemical imaging of the brain using quantitative IR spectro-microscopy, Chem. Sci. 9 (2018) 189–198, http://dx.doi.org/10.1039/C7SC03306K.
[264] M. Rust, M. Bates, X. Zhuang, Sub-diffraction-limit imaging by stochastic optical reconstruction microscopy (STORM), Nature Methods 3 (2006) 793–796, http://dx.doi.org/10.1038/nmeth929.
[265] P.S. Calhoun, B.S. Kuszyk, D.G. Heath, J.C. Carley, E.K. Fishman, Three-dimensional volume rendering of spiral CT data: Theory and method, RadioGraphics 19 (1999) 4–745, http://dx.doi.org/10.1148/radiographics.19.3.g99ma14745.
[266] W.A. Kalender, Computed Tomography: Fundamentals, System Technology, Image Quality, Applications, third ed., Publicis, Erlangen, 2011.
[267] C. Mei, G. Sibley, M. Cummins, P. Newman, I. Reid, REAL: A system for largescale mapping in constant-time using stereo, Int. J. Comput. Vision 94 (2011) 198–214, http://dx.doi.org/10.1007/s11263-010-0361-7.
[268] H. Markram, E. Muller, S. Ramaswamy, M.W. Reimann, M. Abdellah, C.A. Sanchez, A. Ailamaki, L. Alonso-Nanclares, N. Antille, S. Arsever, G.A.A. Kahou, T.K. Berger, A. Bilgili, N. Buncic, A. Chalimourda, G. Chindemi, J.-D. Courcol, F. Delalondre, V. Delattre, S. Druckmann, R. Dumusc, J. Dynes, S. Eilemann, E. Gal, M.E. Gevaert, J.P. Ghobril, A. Gidon, J.W. Graham, A. Gupta, V. Haenel, E. Hay, T. Heinis, J.B. Hernando, M. Hines, L. Kanari, D. Keller, J. Kenyon, G. Khazen, Y. Kim, J.G. King, Z. Kisvarday, P. Kumbhar, S. Lasserre, J.V. Le Bé, B.R.C. Magalhães, A. Merchán-Pérez, J. Meystre, B.R. Morrice, J. Muller, A. Muñoz-Céspedes, S. Muralidhar, K. Muthurasa, D. Nachbaur, T.H. Newton, M. Nolte, A. Ovcharenko, J. Palacios, L. Pastor, R. Perin, R. Ranjan, I. Riachi, J.R. Rodríguez, J.L. Riquelme, C. Rössert, K. Sfyrakis, Y. Shi, J.C. Shillcock, G. Silberberg, R. Silva, F. Tauheed, M. Telefont, M. Toledo-Rodriguez, T. Tränkler, W. Van Geit, J.V. Díaz, R. Walker, Y. Wang, S.M. Zaninetta, J. DeFelipe, S.L. Hill, I. Segev, F. Schürmann, Reconstruction and simulation of neocortical microcircuitry, Cell 163 (2015) 456–492, http://dx.doi.org/10.1016/j.cell.2015.09.029.
[269] P. Guimarães, J. Wigdahl, A. Ruggeri, A fast and efficient technique for the automatic tracing of corneal nerves in confocal microscopy, Trans. Vis. Sci. Tech. 5 (2016) 7, http://dx.doi.org/10.1167/tvst.5.5.7.
[270] G.W. He, T.Y. Wang, A.S. Chiang, Y.T. Ching, Soma detection in 3D images of neurons using machine learning technique, Neuroinformatics 16 (2018) 31–41, http://dx.doi.org/10.1007/s12021-017-9342-0.
[271] C.T. Shih, N.Y. Chen, T.Y. Wang, G.W. He, G.T. Wang, Y.J. Lin, T.K. Lee, A.S. Chiang, NeuroRetriever: Automatic neuron segmentation for connectome assembly, Front. Syst. Neurosci. 15 (2021) 687182, http://dx.doi.org/10.3389/fnsys.2021.687182.
[272] C.T. Shih, O. Sporns, S.L. Yuan, T.S. Su, Y.J. Lin, C.C. Chuang, T.Y. Wang, C.C. Lo, R.J. Greenspan, A.S. Chiang, Connectomics-based analysis of information flow in the Drosophila brain, Curr. Biol. 25 (2015) 1249–1258, http://dx.doi.org/10.1016/j.cub.2015.03.021.
[273] D.G.C. Hildebrand, M. Cicconet, R.M. Torres, W. Choi, T.M. Quan, J. Moon, A.W. Wetzel, A.S. Champion, B.J. Graham, O. Randlett, G.S. Plummer, R. Portugues, I.H. Bianco, S. Saalfeld, A.D. Baden, K. Lillaney, R. Burns, J.T. Vogelstein, A.F. Schier, W.C.A. Lee, W.K. Jeong, J.W. Lichtman, F. Engert, Whole-brain serial-section electron microscopy in larval zebrafish, Nature 545 (2017) 345–349, http://dx.doi.org/10.1038/nature22356.
[274] D.G. Lowe, Distinctive image features from scale-invariant keypoints, Int. J. Comput. Vis. 60 (2004) 91–110, http://dx.doi.org/10.1023/B:VISI.0000029664.99615.94.
[275] P.J. Burt, E. Adelson, The Laplacian pyramid as a compact image code, IEEE Trans. Commun. 31 (4) (1983) 532540, http://dx.doi.org/10.1109/TCOM.1983.1095851.
[276] P. Viola, W.M. Wells, Alignment by maximization of mutual information, in: Proceedings of IEEE International Conference on Computer Vision, 1995, pp. 16–23, http://dx.doi.org/10.1109/ICCV.1995.466930.

[277] P.E. Black, Greedy Algorithm. Dictionary of Algorithms and Data Structures, U.S. National Institute of Standards and Technology (NIST), 2005.
[278] M.A. Fischler, R.C. Bolles, Random sample consensus: A paradigm for model fitting with applications to image analysis and automated cartography, Commun. ACM 24 (1981) 381–395, http://dx.doi.org/10.1145/358669.358692.
[279] F. Tang, H. Tao, Probabilistic object tracking with dynamic attributed relational feature graph, IEEE Trans. Circuits Syst. Video Technol. 18 (2008) 1064–1074, http://dx.doi.org/10.1109/TCSVT.2008.927106.
[280] L. Shepp, The tuning fork artifact in computerized tomography, Comput. Graph. Image Process 10 (1979) 246–255.
[281] W. Lu, T.R. Mackie, Tomographic motion detection and correction directly in sinogram space, Phys. Med. Biol. 47 (2002) 1267–1284, http://dx.doi.org/10.1088/0031-9155/47/8/304.
[282] T. Donath, F. Beckmann, A. Schreyer, Automated determination of the center of rotation in tomography data, J. Opt. Soc. Amer. A 23 (2006) 1048–1057, http://dx.doi.org/10.1364/josaa.23.001048.
[283] N.T. Vo, M. Drakopoulos, R.C. Atwood, C. Reinhard, Reliable method for calculating the center of rotation in parallel-beam tomography, Opt. Express 22 (2014) 19078–19086, http://dx.doi.org/10.1364/OE.22.019078.
[284] H. Yu, Y. Wei, J. Hsieh, G. Wang, Data consistency based translational motion artifact reduction in fan-beam CT, IEEE Trans. Med. Imaging 25 (2006) 792–803, http://dx.doi.org/10.1109/TMI.2006.875424.
[285] H. Kudo, T. Suzuki, E.A. Rashed, Image reconstruction for sparse-view CT and interior CT-introduction to compressed sensing and differentiated backprojection, Quant. Imaging Med. Surg. 3 (2013) 147–161, http://dx.doi.org/10.3978/j.issn.2223-4292.2013.06.01.
[286] D.L. Donoho, Compressed sensing, IEEE Trans. Inf. Theory 52 (4) (2006) 1289–1306, http://dx.doi.org/10.1109/TIT.2006.871582.
[287] Z. Zhu, K. Wahid, P. Babyn, D. Cooper, I. Pratt, Y. Carter, Improved compressed sensing-based algorithm for sparse-view CT image reconstruction, Comput. Math. Methods Med. 2013 (2013) 185750, http://dx.doi.org/10.1155/2013/185750.
[288] Q. Ding, Y. Nan, H. Gao, H. Ji, Deep learning with adaptive hyper-parameters for low-dose CT image reconstruction, IEEE Trans. Comput. Imaging 7 (2021) 648–660, http://dx.doi.org/10.1109/TCI.2021.3093003.
[289] Y. Mao, B.P. Fahimian, S.J. Osher, J. Miao, Development and optimization of regularized tomographic reconstruction algorithms utilizing equally-sloped tomography, IEEE Trans. Image Process 19 (5) (2010) 1259–1268, http://dx.doi.org/10.1109/TIP.2009.2039660.
[290] D. Hu, Y. Zhang, J. Liu, C. Du, J. Zhang, S. Luo, G. Quan, Q. Liu, Y. Chen, L. Luo, SPECIAL: Single-shot projection error correction integrated adversarial learning for limited-angle CT, IEEE Trans. Comput. Imaging 7 (2021) 734–746, http://dx.doi.org/10.1109/TCI.2021.3098922.
[291] Y. Zhang, T. Lv, R. Ge, Q. Zhao, D. Hu, L. Zhang, J. Liu, Y. Zhang, Q. Liu, W. Zhao, Y. Chen, CD-net: Comprehensive domain network with spectral complementary for DECT sparse-view reconstruction, in: IEEE Trans. Comput. Imaging, 7 (2021) 436–447, http://dx.doi.org/10.1109/TCI.2021.3070184.
[292] I. Goodfellow, J. Pouget-Abadie, M. Mirza, B. Xu, D. Warde-Farley, S. Ozair, A. Courville, Y. Bengio, Generative adversarial nets, in: Z. Ghahramani, M. Welling, C. Cortes, N. Lawrence, K.Q. Weinberger (Eds.), in: Adv. Neural Inf. Process. Syst., vol. 27, 2014, pp. 2672–2680.
[293] M. Arjovsky, S. Chintala, L. Bottou, Wasserstein GAN, 2017, http://dx.doi.org/10.48550/arXiv.1701.07875, arXiv preprint arXiv:1701.07875.
[294] R. Anirudh, H. Kim, J.J. Thiagarajan, K.A. Mohan, K. Champley, T. Bremer, Lose the views: Limited angle CT reconstruction via implicit sinogram completion, in: 2018 IEEE/CVF Conference on Computer Vision and Pattern Recognition, 2018, pp. 6343–6352, http://dx.doi.org/10.1109/CVPR.2018.00664.
[295] J. Gu, J.C. Ye, AdaIN-based tunable CycleGAN for efficient unsupervised low-dose CT denoising, IEEE Trans. Comput. Imaging 7 (2021) 73–85, http://dx.doi.org/10.1109/TCI.2021.3050266.
[296] P.J. Burt, E.H. Adelson, A multiresolution spline with application to image mosaics, ACM Trans. Graph. 2 (1983) 217–236, http://dx.doi.org/10.1145/245.247.
[297] Y.C. Lin, Y. Hwu, G.S. Huang, M. Hsiao, T.T. Lee, S.M. Yang, T.K. Lee, N.Y. Chen, S.S. Yang, A. Chen, S.M. Ka, Differential synchrotron X-ray imaging markers based on the renal microvasculature for tubulointerstitial lesions and glomerulopathy, Sci. Rep. 7 (2017) 3488.1, http://dx.doi.org/10.1038/s41598-017-03677-x.
[298] FlyCircuit 1.2, A database of drosophila brain neurons, 2022, http://www.flycircuit.tw/, (Accessed 23 June 2022).
[299] J. Wang, L. Song, Z. Li, H. Sun, J. Sun, N. Zheng, End-to-end object detection with fully convolutional network, in: Proceedings of the IEEE/CVF Conference on Computer Vision and Pattern Recognition, CVPR, 2021, pp. 15849–15858.
[300] G. Cheng, P. Zhou, J. Han, RIFD-CNN: Rotation-invariant and Fisher discriminative convolutional neural networks for object detection, in: Proceedings of the IEEE Conference on Computer Vision and Pattern Recognition, CVPR, 2016, pp. 2884–2893.
[301] Q. Chen, Z. Liu, Y. Zhang, K. Fu, Q. Zhao, H. Du, RGB-D salient object detection via 3D convolutional neural networks, in: Proceedings of the AAAI Conference on Artificial Intelligence, vol. 35, 2021, pp. 1063–1071, https://ojs.aaai.org/index.php/AAAI/article/view/16191.
[302] R. Girshick, Fast R-CNN, in: 2015 IEEE International Conference on Computer Vision, ICCV, 2015, pp. 1440–1448, http://dx.doi.org/10.1109/ICCV.2015.169.
[303] S. Ren, K. He, R. Girshick, J. Sun, Faster R-CNN: Towards real-time object detection with region proposal networks, in: C. Cortes, N.D. Lawrence, D.D. Lee, M. Sugiyama, R. Garnett (Eds.), NIPS, 2015, pp. 91–99.
[304] K. He, G. Gkioxari, P. Dollar, R. Girshick, Mask R-CNN, in: 2017 IEEE International Conference on Computer Vision, ICCV, 2017, pp. 2980–2988, http://dx.doi.org/10.1109/ICCV.2017.322.
[305] J. Redmon, S. Divvala, R. Girshick, A. Farhadi, You only look once: Unified, real-time object detection, in: 2016 IEEE Conference on Computer Vision and Pattern Recognition, CVPR, 2016, pp. 779–788, http://dx.doi.org/10.1109/CVPR.2016.91.
[306] J. Redmon, A. Farhadi, YOLO9000: Better, faster, stronger, in: 2017 IEEE Conference on Computer Vision and Pattern Recognition, CVPR, 2017, pp. 6517–6525, http://dx.doi.org/10.1109/CVPR.2017.690.
[307] J. Redmon, A. Farhadi, YOLOv3: An incremental improvement, 2018, http://dx.doi.org/10.48550/arXiv.1804.02767, arXiv:1804.02767.
[308] A. Bochkovskiy, C.Y. Wang, H.Y.M. Liao, YOLOv4: Optimal speed and accuracy of object detection, 2020, http://dx.doi.org/10.48550/arXiv.2004.10934, arXiv:2004.10934.
[309] T. Rohlfing, C.R. Maurer, Nonrigid image registration in shared-memory multiprocessor environments with application to brains, breasts, and bees, IEEE Trans. Inf. Technol. Biomed. 7 (2003) 16–25, http://dx.doi.org/10.1109/titb.2003.808506.
[310] M. Costa, J.D. Manton, A.D. Ostrovsky, S. Prohaska, G.S.X.E. Jefferis, NBLAST: Rapid, sensitive comparison of neuronal structure and construction of neuron family databases, Neuron 91 (2016) 293–311, http://dx.doi.org/10.1016/j.neuron.2016.06.012.
[311] R. Roy, K. Sato, S. Bhattachrya, X. Fang, Y. Joti, T. Hatsui, T. Hiraki, J. Guo, W. Yu, Compression of time evolutionary image data through predictive deep neural networks, in: 2021 IEEE/ACM 21st International Symposium on Cluster, Cloud and Internet Computing, CCGrid 2021, 2021, pp. 41–50, http://dx.doi.org/10.1109/CCGrid51090.2021.00014.
[312] X. Huang, G. Mei, J. Zhang, R. Abbas, A comprehensive survey on point cloud registration, 2021, http://dx.doi.org/10.48550/arXiv.2103.02690, arXiv preprint arXiv:2103.02690.
[313] T. Ngoc Linh, H. Hiroshi, Global iterative closet point using nested annealing for initialization, Procedia Comput. Sci. 60 (2015) 381–390, http://dx.doi.org/10.1016/j.procs.2015.08.147.
[314] B. Eckart, K. Kim, J. Kautz, HGMR: Hierarchical Gaussian mixtures for adaptive 3D registration, in: European Conference on Computer Vision, ECCV 2018, 2018, https://research.nvidia.com/publication/2018-09_HGMM-Registration.

[315] B. Denis de Senneville, C. Zachiu, M. Ries, C. Moonen, Evolution: An edge-based variational method for non-rigid multi-modal image registration, Phys. Med. Biol. 61 (2016) 7377–7396, http://dx.doi.org/10.1088/0031-9155/61/20/7377.
[316] E. Ferrante, N. Paragios, Non-rigid 2D-3D medical image registration using Markov random fields, in: K. Mori, I. Sakuma, Y. Sato, C. Barillot, N. Navab (Eds.), Medical Image Computing and Computer-Assisted Intervention – MICCAI 2013, MICCAI 2013, in: Lecture Notes in Computer Science, vol. 8151, Springer, Berlin, Heidelberg, 2013, pp. 163–170, http://dx.doi.org/10.1007/978-3-642-40760-4_21.
[317] F. Khalifa, G.M. Beache, G. Gimel'farb, J.S. Suri, A.S. El-Baz, State-of-the-art medical image registration methodologies: A survey, in: A. El-Baz, U.R. Acharya, M. Mirmehdi, J. Suri (Eds.), Multi Modality State-of-the-Art Medical Image Segmentation and Registration Methodologies, Springer, Boston, MA, 2011, pp. 235–280, http://dx.doi.org/10.1007/978-1-4419-8195-0_9.
[318] H. Bay, T. Tuytelaars, L. Van Gool, SURF: Speeded up robust features, in: A. Leonardis, H. Bischof, A. Pinz (Eds.), Computer Vision – ECCV 2006, ECCV 2006, in: Lecture Notes in Computer Science, vol. 3951, Springer, Berlin, Heidelberg, 2006, pp. 404–417, http://dx.doi.org/10.1007/11744023_32.
[319] D. Fleet, Y. Weiss, Optical flow estimation, in: N. Paragios, Y. Chen, O. Faugeras (Eds.), Handbook of Mathematical Models in Computer Vision, Springer, Boston, 2006, pp. 237–257, http://dx.doi.org/10.1007/0-387-28831-7_15.
[320] D. Stalling, M. Westerhoff, H.C. Hege, Amira: A highly interactive system for visual data analysis, in: C.D. Hansen, C.R. Johnson (Eds.), The Visualization Handbook, Elsevier, 2005, pp. 749–767, http://dx.doi.org/10.1016/B978-012387582-2/50040-X.
[321] CloudCompare, 2022, https://www.cloudcompare.org. (Accessed 23 June 2023).
[322] P. Cignoni, M. Callieri, M. Corsini, M. Dellepiane, F. Ganovelli, G. Ranzuglia, MeshLab: An open-source mesh processing tool, Sixth Eurographics Italian Chapter Conference (2008) 129–136, http://dx.doi.org/10.2312/LocalChapterEvents/ItalChap/ItalianChapConf2008/129-136.
[323] Noctylio, 2022, http://www.noctylio.com/index.html. (Accessed 23 June 2023).
[324] S. Tsugawa, K. Teratsuji, F. Okura, K. Noshita, M. Tateno, J. Zhang, T. Demura, Exploring the mechanical and morphological rationality of tree branch structure based on 3D point cloud analysis and the finite element method, Sci. Rep. 12 (2022) 4054, http://dx.doi.org/10.1038/s41598-022-08030-5.
[325] Z. Sun, C. Wang, X. Hao, W. Li, X. Zhang, Quantitative evaluation for shape characteristics of aggregate particles based on 3D point cloud data, Constr. Build. Mater. 263 (2020) 120156, http://dx.doi.org/10.1016/j.conbuildmat.2020.120156.
[326] B. Elnashef, S. Filin, R.N. Lati, Tensor-based classification and segmentation of three-dimensional point clouds for organ-level plant phenotyping and growth analysis, Comput. Electron. Agric. 156 (2019) 51–61, http://dx.doi.org/10.1016/j.compag.2018.10.036.
[327] F. Milletari, N. Navab, S. Ahmadi, V-Net: Fully convolutional neural networks for volumetric medical image segmentation, 2016, http://dx.doi.org/10.48550/arXiv.1606.04797, arXiv:1606.04797.
[328] V. Badrinarayanan, A. Kendall, R. Cipolla, SegNet: A deep convolutional encoder-decoder architecture for image segmentation, IEEE Trans. Pattern Anal. Mach. Intell. 39 (12) (2017) 2481–2495, http://dx.doi.org/10.1109/TPAMI.2016.2644615.
[329] O. Ronneberger, P. Fischer, T. Brox, U-net: Convolutional networks for biomedical image segmentation, 2015, http://dx.doi.org/10.48550/arXiv.1505.04597, arXiv:1505.04597.
[330] X. Liu, L. Song, S. Liu, Y. Zhang, A review of deep-learning-based medical image segmentation methods, Sustainability 13 (1224) (2021) http://dx.doi.org/10.3390/su13031224.
[331] G. Lepetit-Aimon, R. Duval, F. Cheriet, Large receptive field fully convolutional network for semantic segmentation of retinal vasculature in Fundus images, in: Computational Pathology and Ophthalmic Medical Image Analysis, OMIA COMPAY 2018 2018, in: Lecture Notes in Computer Science, vol. 11039, Springer, Cham, 2018, pp. 201–209, http://dx.doi.org/10.1007/978-3-030-00949-6_24.
[332] GenomeAsia 100K, 2022, https://www.genomeasia100k.com. (Accessed 23 June 2022).
[333] Personal communication, Stephan C. Schuster, Singapore Centre for Environmental Life Sciences Engineering, Nanyang Technological University, Singapore.
[334] GenomeAsia100K Consortium, The GenomeAsia 100K project enables genetic discoveries across Asia. GenomeAsia consortium, Nature 576 (2019) 106–111, http://dx.doi.org/10.1038/s41586-019-1793-z.
[335] Tin Wee Tan, Marek Michalewicz, Personal communication.
[336] G. Noaje, A. Davis, J. Low, S. Lim, G.L. Tan, L. Orłowski, D. Chien, S.W. Liou, T.W. Tan, Y. Poppe, K. Ban Hon Kim, A. Howard, D. Southwell, J. Gunthorpe, M. Michalewicz, InfiniCortex - From proof-of-concept to production, Supercomput. Front. Innov. 4 (2017) 87–102, http://dx.doi.org/10.14529/jsfi170207.
[337] Data mover challenge, NSCC, Singarpore, 2022, https://www.nscc.sg/data-mover-challenge-2021/. (Accessed 23 June 2022).
[338] Tin Wee Tan, Personal communication.
[339] M. Barisits, T. Beermann, F. Berghaus, B. Bockelman, J. Bogado, D. Cameron, D. Christidis, D. Ciangottini, G. Dimitrov, M. Elsing, V. Garonne, A. di Girolamo, L. Goossens, W. Guan, J. Guenther, T. Javurek, D. Kuhn, M. Lassnig, F. Lopez, N. Magini, A. Molfetas, A. Nairz, F. Ould-Saada, S. Prenner, C. Serfon, G. Stewart, E. Vaandering, P. Vasileva, R. Vigne, T. Wegner, Rucio: Scientific data management, Comput. Softw. Big Sci. 3 (2019) 11, http://dx.doi.org/10.1007/s41781-019-0026-3.
[340] G.M. Kurtzer, V. Sochat, M.V. Bauer, Singularity: Scientific containers for mobility of compute, PLoS One 12 (2017) e0177459, http://dx.doi.org/10.1371/journal.pone.0177459.
[341] In addition to the standard algorithm/software project development tools such as Jira or GitLab.
[342] The global research platform, 2022, https://www.theglobalresearchplatform.net/. (Accessed 23 June 2022).
[343] Pytorch, 2022, https://pytorch.org/. (Accessed 23 June 2022).
[344] J. Wang, L. Song, Z. Li, H. Sun, J. Sun, N. Zheng, End-to-end object detection with fully convolutional network, in: Proceedings of the IEEE/CVF Conference on Computer Vision and Pattern Recognition, CVPR, 2021, pp. 15849–15858, http://dx.doi.org/10.48550/arXiv.2012.03544.
[345] G. Cheng, P. Zhou, J. Han, RIFD-CNN: Rotation-Invariant and Fisher Discriminative Convolutional Neural Networks for Object Detection, CVPR, 2016, pp. 2884–2893.
[346] Q. Chen, Z. Liu, Y. Zhang, K. Fu, Q. Zhao, H. Du, RGB-D salient object detection via 3D convolutional neural networks, in: Proceedings of the AAAI Conference on Artificial Intelligence, vol. 35, AAAI, 2021, pp. 1063–1071, https://ojs.aaai.org/index.php/AAAI/article/view/16191, 2021.
[347] R. Girshick, Fast R-CNN, in: 2015 IEEE International Conference on Computer Vision, ICCV, 2015, pp. 1440–1448, http://dx.doi.org/10.1109/ICCV.2015.169.
[348] S. Ren, K. He, R. Girshick, J. Sun, Faster R-CNN: Towards real-time object detection with region proposal networks, in: Advances in Neural Information Processing Systems 28, NIPS 2015, 2015, pp. 91–99.
[349] K. He, G. Gkioxari, P. Dollar, R. Girshick, Mask R-CNN, in: 2017 IEEE International Conference on Computer Vision, ICCV, 2017, pp. 2980–2988, http://dx.doi.org/10.1109/ICCV.2017.322.
[350] J. Redmon, S. Divvala, R. Girshick, A. Farhadi, You only look once: Unified, real-time object detection, in: 2016 IEEE Conference on Computer Vision and Pattern Recognition, CVPR, 2016, pp. 779–788, http://dx.doi.org/10.1109/CVPR.2016.91.
[351] J. Redmon, A. Farhadi, YOLO9000: Better, faster, stronger, in: 2017 IEEE Conference on Computer Vision and Pattern Recognition, CVPR, 2017, pp. 6517–6525, http://dx.doi.org/10.1109/CVPR.2017.690.
[352] J. Redmon, A. Farhadi, YOLOv3: An incremental improvement, 2018, http://dx.doi.org/10.48550/arXiv.1804.02767, arXiv:1804.02767.

[353] A. Bochkovskiy, C.Y. Wang, H.Y.M. Liao, YOLOv4: Optimal speed and accuracy of object detection, 2020, http://dx.doi.org/10.48550/arXiv.2004.10934, arXiv:2004.10934.
[354] S. Navlakha, P. Ahammad, E.W. Myers, Unsupervised segmentation of noisy electron microscopy images using salient watersheds and region merging, BMC Bioinform. 14 (2013) 294, http://dx.doi.org/10.1186/1471-2105-14-294.
[355] M.K. Bashar, K. Komatsu, T. Fujimori, T.J. Kobayashi, Automatic extraction of nuclei centroids of mouse embryonic cells from fluorescence microscopy images, PLoS One 7 (2012) e35550, http://dx.doi.org/10.1371/journal.pone.0035550.
[356] S. Wienert, D. Heim, K. Saeger, A. Stenzinger, M. Beil, P. Hufnagl, M. Dietel, C. Denkert, F. Klauschen, Detection and segmentation of cell nuclei in virtual microscopy images: A minimum-model approach, Sci. Rep. 2 (2012) 503, http://dx.doi.org/10.1038/srep00503.
[357] T. Quan, T. Zheng, Z. Yang, W. Ding, S. Li, J. Li, H. Zhou, Q. Luo, H. Gong, S. Zeng, Neurogps: Automated localization of neurons for brain circuits using l1 minimization model, Sci. Rep. 3 (2013) 1414, http://dx.doi.org/10.1038/srep01414.
[358] S. Cheng, T. Quan, X. Liu, S. Zeng, Large-scale localization of touching somas from 3D images using density-peak clustering, BMC Bioinform. 17 (2016) 375, http://dx.doi.org/10.1186/s12859-016-1252-x.
[359] K.-M. Kim, K. Son, G.T.R. Palmore, Neuron image analyzer: Automated and accurate extraction of neuronal data from low quality images, Sci. Rep. 5 (2015) 17062, http://dx.doi.org/10.1038/srep17062.
[360] K. El-Laithy, M. Knorr, J. Käs, M. Bogdan, Digital detection and analysis of branching and cell contacts in neural cell cultures, J. Neurosci. Methods 210 (2012) 206–219, http://dx.doi.org/10.1016/j.jneumeth.2012.07.007.
[361] S. Liu, D. Zhang, S. Liu, D. Feng, H. Peng, W. Cai, Rivulet: 3dneuron morphology tracing with iterative back-tracking, Neuroinform. 14 (2016) 387–401, http://dx.doi.org/10.1007/s12021-016-9302-0.
[362] H. Xiao, H. Peng, App2: Automatic tracing of 3D neuronmorphology based on hierarchical pruning of a gray-weighted image distance-tree, Bioinformatics 29 (2013) 1448–1454, http://dx.doi.org/10.1093/bioinformatics/btt170.
[363] Z. Zhou, S. Sorensen, H. Zeng, M. Hawrylycz, H. Peng, Adaptive image enhancement for tracing 3d morphologies of neurons and brain vasculatures, Neuroinform. 13 (2015) 153–166, http://dx.doi.org/10.1007/s12021-014-9249-y.
[364] B. Ozcan, P. Negi, F. Laezza, M. Papadakis, D. Labate, Automated detection of soma location and morphology in neuronal network cultures, PLoS One 10 (2015) e0121886, http://dx.doi.org/10.1371/journal.pone.0121886.
[365] C.B. Kayasandik, D. Labate, Improved detection of soma location and morphology in fluorescence microscopy images of neurons, J. Neurosci. Methods 274 (2016) 61–70, http://dx.doi.org/10.1016/j.jneumeth.2016.09.007.
[366] G.-W. He, T.-Y. Wang, A.-S. Chiang, Y.-T. Ching, Soma detection in 3d images of neurons using machine learning technique, Neuroinform. 16 (2018) 31–41, http://dx.doi.org/10.1007/s12021-017-9342-0.
[367] J. Chen, H. Huang, J. Peng, J. Zhu, L. Chen, W. Li, B. Sun, H. Li, Convolution neural network architecture learning for remote sensing scene classification, 2020, http://dx.doi.org/10.48550/arXiv.2001.09614, arXiv:2001.09614.
[368] M.A. Kadhim, M.H. Abed, Convolutional neural network for satellite image classification, in: M. Huk, M. Maleszka, E. Szczerbicki (Eds.), Intelligent Information and Database Systems: Recent Developments, ACIIDS 2019, in: Studies in Computational Intelligence, vol. 830, Springer, Cham, 2020, pp. 165–178, http://dx.doi.org/10.1007/978-3-030-14132-5_1310.
[369] M. Uma, G. Padmavathi, An efficient network traffic monitoring for wireless networks, Int. J. Comput. Appl. 53 (2012) 51–59, http://dx.doi.org/10.5120/8453-2255.
[370] J. Lee, J. Bang, S. Yang, Object detection with sliding window in images including multiple similar objects, in: 2017 International Conference on Information and Communication Technology Convergence, ICTC, 2017, pp. 80–806, http://dx.doi.org/10.1109/ICTC.2017.8190786.
[371] M. Najibi, B. Singh, L. Davis, AutoFocus: Efficient multi-scale inference, in: 2019 IEEE/CVF International Conference on Computer Vision, ICCV, 2019, pp. 9744–9754, http://dx.doi.org/10.1109/ICCV.2019.00984.
[372] B. Uzkent, C. Yeh, S. Ermon, Efficient object detection in large images using deep reinforcement learning, in: 2020 IEEE Winter Conference on Applications of Computer Vision, WACV, 2020, pp. 1813–1822, http://dx.doi.org/10.1109/WACV45572.2020.9093447.
[373] Z. Tian, C. Shen, H. Chen, T. He, FCOS: Fully convolutional one-stage object detection, in: 2019 IEEE/CVF International Conference on Computer Vision, ICCV, 2019, pp. 9626–9635, http://dx.doi.org/10.1109/ICCV.2019.00972.
[374] Z. Yang, S. Liu, H. Hu, L. Wang, S. Lin, RepPoints: Point set representation for object detection, in: 2019 IEEE/CVF International Conference on Computer Vision, ICCV, 2019, pp. 9656–9665, http://dx.doi.org/10.1109/ICCV.2019.00975.
[375] Y. Chen, Z. Zhang, Y. Cao, L. Wang, S. Lin, H. Hu, RepPoints v2: Verification meets regression for object detection, in: H. Larochelle, M. Ranzato, R. Hadsell, M.F. Balcan, H. Lin (Eds.), NIPS'20: Proceedings of the 34th International Conference on Neural Information Processing Systems 2020, (NeurIPS 2020), Vancouver, Canada, pp. 5621–5631.
[376] K. Duan, S. Bai, L. Xie, H. Qi, Q. Huang, Q. Tian, CenterNet: Keypoint triplets for object detection, in: 2019 IEEE/CVF International Conference on Computer Vision, ICCV, 2019, pp. 6568–6577, http://dx.doi.org/10.1109/ICCV.2019.00667.
[377] S. Zhang, C. Chi, Y. Yao, Z. Lei, S.Z. Li, Bridging the gap between anchor-based and anchor-free detection via adaptive training sample selection, in: 2020 IEEE/CVF Conference on Computer Vision and Pattern Recognition, CVPR, 2020, pp. 9756–9765, http://dx.doi.org/10.1109/CVPR42600.2020.00978.
[378] N. Otsu, A threshold selection method from gray-level histograms, IEEE Trans. Syst. Man. Cyber. 9 (1979) 62–66, http://dx.doi.org/10.1109/TSMC.1979.4310076.
[379] S. Cheng, T. Quan, X. Liu, S. Zeng, Large-scale localization of touching somas from 3D images using density-peak clustering, BMC Bioinform. 17 (2016) 375, http://dx.doi.org/10.1186/s12859-016-1252-x.
[380] H.J. Vala, A. Baxi, A review on otsu image segmentation algorithm, Int. J. Adv. Res. Comput. Eng. Technol. (IJARCET) 2 (2013) 387–389.
[381] F. Pedregosa, G. Varoquaux, A. Gramfort, V. Michel, B. Thirion, O. Grisel, M. Blondel, P. Prettenhofer, R. Weiss, V. Dubourg, J. Vanderplas, A. Passos, D. Cournapeau, M. Brucher, M. Perrot, E. Duchesnay, Scikit-learn: Machine learning in Python, J. Mach. Learn. Res. 12 (2011) 2825–2830, http://jmlr.org/papers/v12/pedregosa11a.html & http://scikit-learn.sourceforge.net.